Thesis presented to the Technological Institute of Aeronautics, in partial fulfillment of the requirements for the degree of Doctor of Science in the Program of Physics, Area of Plasma Physics.

David Arruda Toneli

A VOLUME AVERAGED GLOBAL MODEL STUDY OF OXYGEN DISCHARGES – FORMATION AND ANNIHILATION OF THE SINGLET MOLECULAR METASTABLES AND EFFECTS OF THE ELECTRON ENERGY DISTRIBUTION FUNCTION

Thesis approved in its final version by signatories below:

Prof. Dr. Marisa Roberto

Advisor

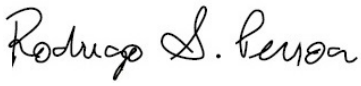

Prof. Dr. Rodrigo Sávio Pessoa

Co-advisor

Prof. Dr. Luiz Carlos Sandoval Góes

Prorector of Graduate Studies and Research

Campo Montenegro
São José dos Campos, SP - Brazil
2016

Cataloging-in Publication Data
Documentation and Information Division

Toneli, David Arruda
A volume averaged global model study of oxygen discharges – formation and annihilation of the singlet molecular metastables and effects of the electron energy distribution function / David Arruda Toneli.
São José dos Campos, 2016.
93f.

Thesis of Doctor of Science – Course of Physics. Area of Plasma Physics – Technological Institute of Aeronautics, 2016. Advisor: Prof. Dr. Marisa Roberto. Co-advisor: Prof. Dr. Rodrigo Sávio Pessoa.

1. Physics. 2. Plasma. 3. Oxygen. 4. Metastable. 5. Modelling. I. Technological Institute of Aeronautics. II. Title.

BIBLIOGRAPHIC REFERENCE

TONELI, David Arruda. **A volume averaged global model study of oxygen discharges – formation and annihilation of the singlet molecular metastables and effects of the electron energy distribution function**. 2016. 93f. Thesis of Doctor of Science – Technological Institute of Aeronautics, São José dos Campos.

CESSION OF RIGHTS

David Arruda Toneli
Rua Itambé, 154
12.230-660 – São José dos Campos–SP

A VOLUME AVERAGED GLOBAL MODEL STUDY OF OXYGEN DISCHARGES – FORMATION AND ANNIHILATION OF THE SINGLET MOLECULAR METASTABLES AND EFFECTS OF THE ELECTRON ENERGY DISTRIBUTION FUNCTION

David Arruda Toneli

Thesis Committee Composition:

Prof. Dr.	Gilberto Petraconi Filho	Chair	-	ITA
Prof. Dr.	Marisa Roberto	Advisor	-	ITA
Prof. Dr.	Rodrigo Sávio Pessoa	Co-advisor	-	UNIVAP
Prof. Dr.	Gerson Otto Ludwig	Internal examiner	-	INPE
Prof. Dr.	Rogério Pinto Mota	External examiner	-	UNESP
Prof. Dr.	Zwinglio O. Guimarães Filho	External examiner	-	USP

ITA

To the ones who supported me

Acknowledgments

First, I have to thank God for giving me the capacity to complete this work. Then, I thank my advisor Marisa Roberto and my co-advisor Rodrigo Sávio Pessoa for the knowledge shared during this time. I really appreciate the cooperation of the professor Jon Tomas Gudmundsson. I thank to the graduate coordinator Manuel M. B. Malheiro Oliveira for motivation and support. I thank to the professors of the Technological Institute of Aeronautics that contributed to my development. I thank to all the staff of the Technological Institute of Aeronautics. I would also acknowledge the financial support of the Sectoral Fund for Technology Information (CT-INFO) represented by Brazilian National Council of Research and Development (CNPq), the Coordination for the Improvement of Higher Education Personnel (CAPES), and the São Paulo Research Foundation (FAPESP).

"The more critically one exercises one's capacity for learning, the greater is one's capacity for constructing and developing what I call "epistemological curiosity", without which it is not possible to obtain a complete grasp of the object of our knowledge"

— Paulo Freire.

Resumo

Este trabalho descreve um modelo computacional chamado de *"volume averaged global model"* para um plasma de oxigênio produzido em um reator do tipo indutivo associado à uma fonte de tensão alternada que opera em uma frequência de 13,56 MHz. Este modelo considera um extenso conjunto de reações que inclui as espécies: $O_2(X^3\Sigma_g^-)$, $O_2(a^1\Delta_g)$, $O_2(b^1\Sigma_g^+)$, $O_2(A^3\Sigma_u^+$, $A'^3\Delta_u$, $c^1\Sigma_u^-)$, O_2^+, O_2^-, $O(^3P)$, $O(^1D)$, O^+, O^-, O_3, O_3^+, O_3^- e elétrons. Os valores dos coeficientes de reação de algumas reações são avaliados e novos valores são propostos. Calculou-se as densidades das várias espécies em função da pressão na faixa de 1 à 100 mTorr. Neste trabalho também avaliou-se a influência da função de distribuição de energia dos elétrons (FDEE) e do material das paredes do reator. Diferenças nos resultados para funções de distribuição Maxwelliana e não Maxwellianas mostram a importância de usar FDEEs adequadas no estudo computacional de descargas elétricas em oxigênio. Também foi estudado as diferenças devido a reatores de diferentes materiais comparando resultados para um reator de alumínio anodizado com um reator de aço inoxidável. Devido ao baixo coeficiente de recombinação de átomos de oxigênio em paredes de alumínio anodizado a produção de átomos de oxigênio em reatores de alumínio anodizado aumenta quando comparado com um reator de aço inoxidável. Entretanto, essa diferença diminui quando a pressão aumenta. Assim, reatores de alumínio anodizado são mais apropriados em aplicações onde se deseja uma maior concentração de átomos de oxigênio. A formação e a aniquilação dos estados singletos metaestáveis da molécula de oxigênio foram avaliadas. Encontrou-se que a densidade de $O_2(a^1\Delta_g)$ pode ser menor do que a densidade de $O_2(b^1\Sigma_g^+)$ contradizendo resultados anteriores. As taxas de reação para formação e aniquilação de $O_2(a^1\Delta_g)$ e $O_2(b^1\Sigma_g^+)$ foram avaliadas e as mais importantes reações foram indicadas. O processo de perda de O^- foi também estudado. Recentemente, resultados experimentais têm mostrado que a velocidade com que cada íon entra na bainha pode se aproximar de um valor comum. Este valor seria aquele obtido da solução do critério de Bohm generalizado assumindo que todos os íons alcançam a bainha com a mesma velocidade. Assim, neste trabalho também estudou-se essa velocidade comum dos íons através de uma expressão obtida da relação de dispersão para um plasma com várias espécies de íons positivos e negativos. Quando a eletronegatividade aumenta na região da bainha, a velocidade comum dos íons diminui como ocorre para a velocidade de Bohm.

Abstract

This work describes a computational model called volume averaged global model for an oxygen plasma produced in an inductive reactor coupled to an AC power source which operates at a frequency of 13.56 MHz. This model considers an extensive reaction set that includes the species: $O_2(X^3\Sigma_g^-)$, $O_2(a^1\Delta_g)$, $O_2(b^1\Sigma_g^+)$, $O_2(A^3\Sigma_u^+$, $A'^3\Delta_u$, $c^1\Sigma_u^-)$, O_2^+, O_2^-, $O(^3P)$, $O(^1D)$, O^+, O^-, O_3, O_3^+, O_3^-, and electrons. Rate coefficients for some reactions are evaluated and new values are proposed. It was calculated the densities of various species as a function of discharge pressure in the pressure range 1 – 100 mTorr. In this work, the influence of the electron energy distribution function (EEDF) and the wall material were also evaluated. Differences in the results for Maxwellian and non-Maxwellian distributions show the importance of using a proper EEDF in discharge modelling. It was also explored the differences due to different reactor wall materials comparing the results for an anodized aluminium reactor with a stainless steel reactor. Due to the low recombination coefficient for oxygen atoms on the anodized aluminium walls, the yield of atomic oxygen in anodized aluminium reactors increases significantly as compared to stainless steel reactors. However, the difference of the yield of atomic oxygen in these reactors decreases as pressure increases. Thus, anodized aluminium reactors can be desired for applications where a high concentration of atomic oxygen is required. Formation and annihilation of the singlet molecular metastables were evaluated. It was found that the $O_2(a^1\Delta_g)$ density can be lower than the $O_2(b^1\Sigma_g^+)$ density contradicting previous results. The relative reaction rates for formation and annihilation of $O_2(a^1\Delta_g)$ and $O_2(b^1\Sigma_g^+)$ are evaluated and the most important reactions are indicated. Recently, experimental results have shown that the velocity of each ion at the sheath edge can approximate to a common value. One of these values would be the solution of the generalized Bohm criterion assuming that all ions reach the sheath edge at the same velocity. Thus, in this work, it was also studied this common velocity of the ions through an expression obtained from the dispersion relation for a plasma with many species of positive and negative ions. As the electronegativity at the sheath increases, the common velocity of the ions decreases as the Bohm velocity.

Contents

1 Introduction

In physical science, the term plasma was firstly used by Irving Langmuir to describe the region of an electrical discharge with the same number of ions and electrons [1]. The reason for Langmuir choose the word plasma was the resemblance between that region of the discharge and the blood plasma – electrons, ions and molecules were compared to red and white corpuscles and germs [2, 3]. Plasma is the fourth state of matter, i.e., matter can be found in the solid, liquid, gas or plasma states. It should be mentioned here that the Bose-Einstein condensate is also considered as a state of matter. The concept of a fourth state of matter was proposed by Michael Faraday and reasserted by Willian Crookes [4]. Providing energy to the matter in the gaseous state, neutral atoms and molecules fragment into ions and electrons and the matter changes to the plasma state. Thus, say that a plasma is an ionized gas is correct, although it would be weird if plasma is accepted as a state of matter as it is weird to say that a liquid is a melted solid. The status of plasma as a state of matter has been questioned [5] which would make plasma an ionized gas, but not all ionized gas is a plasma. Every gas has even a small degree of ionization; therefore, according to Chen [6], an ionized gas is in the plasma state if it satisfies three conditions:

1. Quasineutrality: plasma dimensions have to be much larger than the Debye length so that local concentrations of charge or external potentials can be shielded out in a short distance compared to the plasma dimensions.

2. Collective behavior: the particles in the plasma exhibit a collective behaviour due to inner interactions in response to the local conditions.

3. The third condition is a mathematical relationship between the plasma frequency and the rate of collisions between charged and neutral particles which determines if the motion of the charged particles is controlled by electromagnetic forces or hydrodynamic forces.

Flames, lightning, and the Aurora Borealis (the Nothern Lights) are some examples of natural plasma phenomena that we are used to. Regarding flames, if the three conditions stated above were satisfied, they are plasmas [7]. As claimed by von Engel and Cozens [8],

"the part of a flame that possesses the well-known properties of an electric plasma is called "flame plasma", and thus not every type of flame deserves this distinction". However, it is possible to find in the literature statements asserting that flames are plasmas [9, 10].

Most of the observable matter in the universe is in the plasma state. Thus, plasma physics is of great importance to space physics and astrophysics. Space plasma physics is limited to the study of plasmas occuring naturally in the Solar System while plasma astrophysics is concerned with birth, evolution and death of visible structures in the universe like stars and galaxies. In plasma conferences, these two research areas are frequently presented in one area – space and astrophysical plasmas. The European Physical Society Conference on Plasma Physics divides the plasma science into four topical areas: magnetic confinement fusion, beam plasma and inertial fusion, low temperature plasmas, and basic and astrophysical plasmas [11]. The subject of this work is in the low temperature plasma area which adresses weakly ionized plasmas. These plasmas are also named collisional plasmas because coupling, i.e., the transfer of energy, occurs first from the power source to electrons and ions then to neutral atoms and molecules through collisions producing chemically active species.

Low temperature plasmas can be arranged into thermal plasmas and non-thermal plasmas [12, 13]. Here, thermal plasma means a thermal quasi-equilibrium state where electrons, ions and neutral atoms and molecules have approximately the same temperature. A complete equilibrium state is found in high temperature plasmas. The term "cold plasmas" is assigned to non-thermal low temperature plasmas [13–15] where there is a non-equilibrium state due to a low rate of collisions resulting in high electron temperature and heavy particle temperatures in the range of the room temperature. Thus, cold plasmas are weakly ionized plasmas while hot plasmas are fully ionized plasmas as fusion plasmas, solar wind, and stellar interiors.

This work presents a study of an oxygen cold plasma produced in a reactor for inductively coupled plasmas (ICPs). In the past decades, there has been an increasing interest in oxygen discharges due to their applications in different areas such as plasma materials processing, plasma sterilization [16], plasma medicine [17], and oxygen-iodine lasers [18] to name a few. Plasma materials processing in microelectronics fabrication uses oxygen plasma for ashing of photoresist [19–22], removal and/or treatment of polymer films [23, 24], oxidation of silicon [25], and deposition of oxide-based materials which is performed in oxygen diluted discharges [26]. In the chapter 2, an ICP is presented along with a glow discharge and a capacitively coupled plasma (CCP) in order to obtain a thorough understanding of the kind of plasma that was studied here. Regarding the importance of the metastable states for studies of oxygen plasmas, a short explanation of spectroscopic notation for atoms and diatomic molecules is presented in the chapter 3. It serves as a guide for students that are not familiar with this subject. For a full

understanding, the references that are found in the text are recommended. Chapter 4 presents a reviewed reaction set for modelling of oxygen discharges. The mathematical background of the volume averaged global model is presented in the chapter 5.

One of the computational approaches to study the plasma chemistry is the volume averaged global model that is characterized by its simplicity. The spatial variations of the plasma parameters are neglected in the model, thus it only calculates the average parameters. This allows including a large number of reactions with relatively low computer time. Initially, the volume averaged global model was developed to describe the characteristics of argon plasmas created in different kinds of high density low pressure plasma sources [27]. Subsequently, it was used to study the chemistry of atomic and molecular gas discharges and gas mixtures [28–30]. In fact, the volume averaged global model is particularly useful when exploring complex and convoluted chemistries. There have been various modifications of the volume averaged global model over the years in order to improve the understanding of the plasma chemistry and obtain modelling results closer to the experimental data.

Utilizing good databases of reactions and rate constants [31–35], a volume averaged global model similar to that proposed by Kim *et al* [36, 37] was developed further to include a larger number of reactions in order to evaluate oxygen discharges. There are a great number of studies of oxygen discharges, both experimental [38–42] and modelling efforts [28,29,36,37,40,43–45], of which some are compared with the results obtained in this work presented in the chapter 6. In this chapter, it was evaluated changes in the electron energy distribution function (EEDF). Most efforts to model the plasma chemistry of the oxygen discharge have assumed Maxwellian EEDF [28, 37, 40, 44, 46]. Modelling studies where the effects of non-Maxwellian EEDFs on the plasma parameters are evaluated have been reported for Ar discharge [47], N_2 discharge [48], Cl_2 discharge [49,50], Ar/O_2 mixture discharge [45], and CF_4 discharge [51]. It is not known so far similar studies for oxygen discharges other than the scientific papers [52,53] that are results of this work. This study also compares plasma produced in a stainless steel reactor with a plasma produced in an anodized aluminium reactor.

Recently, experimental results have shown that the velocity of the ions at the sheath edge can approximate to a common value [54–56]. One of these values would be the solution of the generalized Bohm criterion assuming that all ions reach the sheath edge at the same with the same velocity – the ions sound speed of the system. An expression for the ion sound speed of the system for a plasma with multiple positive and negative ions obtained from the dispersion relation at the sheath edge is presented in the chapter 7. Changes in the energy distribution functions of electrons and negative ions can also be evaluated through this expression. As the electronegativity at the sheath edge is high, the ion sound speed of the system decreases. Moreover, changes in the distribution functions

of electrons and negative ions are also significant. Finally, the concluding remarks are presented in the chapter 8. The annex A provides the cross sections for the electron-impact reactions used in the model.

2 Plasma sources – glow discharge, CCP, and ICP

Chapman wrote in his book [57]: *"Amongst sputtering and plasma etching folks, the words 'plasma' and 'glow discharge' tend to be used synonymously – to the horror of plasma physicists, I'm sure!"*. A glow discharge is one of the three regimes of an electrical discharge – the others are dark discharge and arc discharge. The characteristics of an electrical discharge as luminescence, current density, voltage-current graph, and breakdown voltage depend on how it was produced; i.e., depend on gas, geometry and material of the electrodes, and vessel. As a glow discharge is an electrical discharge, 'electrical discharge' usually is also used as synonymous of 'plasma'. However, one should keep in mind that plasma refers to a region of an electrical discharge.

A direct current (DC) glow discharge is produced when a DC voltage is applied between two electrodes in a gas and it is high enough to overcome the breakdown point. Then, a sequence of bright and dark layers can be seen along the discharge tube. Therefore, the glow discharge is divided in different regions: the Aston Dark Space, the Cathode Glow, the Cathode Dark Space also called Crooks Dark Space or Hittorf Dark Space, the Negative Glow, the Faraday Dark Space, the Positive Column, the Anode Glow, and the Anode Dark Space (see figure 2.1).

In the Aston Dark Space, electrons that were emitted from cathode have insufficient energy to excite atoms or molecules, thus this region is dark. Across this layer, electrons receive energy from the electric field. At the beginning of the Cathode Glow, electron energies are sufficient to excite atoms or molecules which return to the ground state emitting a photon ($h\nu$). The frequency ν depends on the gas in the discharge tube. Photons are also emitted when ions that are in excited states due to electron-ion recombination return to the ground state. In the spectrum of a DC glow discharge, there are line spectra of excited neutrals and broadband spectra of excited ions [58]. At the end of the Cathode Glow, there are the low energy electron group that lost energy in inelastic collisions and the high energy electron group that kept accumulating energy through this layer. Electrons from the first group do not have energy enough to excite atoms or molecules

while electrons from the second group ionize atoms or molecules instead of excite them. Therefore, the next region is dark.

In the Cathode Dark Space, the number of electrons has a significant increase due to ionization processes. Electrons receive energy through the Cathode Dark Space. When they are able to excite atoms or molecules again, the brightest region of the DC glow discharge begins – the Negative Glow. Electrons lose energy through inelastic collisions in the Negative Glow becoming unable to excite neutrals. Due to the wide range of electron energies at the beginning of the Negative Glow, the end of the Negative Glow is not well defined fading into the Faraday Dark Space.

As electrons go further from the cathode, the electric field becomes weaker because the voltage difference applied between the electrodes have a significant fall in the regions close to the cathode due to the build up of positive ions. Thus, in the Faraday Dark Space, electrons receive less energy from the electric field as compared to the previous layers that explains why it is the longest dark layer. At the beginning of the Positive Column, electron have sufficient energy to excite atoms or molecules again. While in the Cathode Glow there is an excess of positive ions and in the Negative Glow there is an excess of negative ions, in the Positive Column there is a balance of positive ions and negative ions and electrons. It is the first bright layer where the charge neutrality condition is valid. It is in the Positive Column where the ionized gas satisfies the plasma requirements. At the end of the Positive Column, ionization is possible again due to the increase of the electric field which also repel positive ions to the Positive Column resulting in the Anode Glow which is a layer even brighter than the Positive Column. Electrons that lost energy through inelastic collisions in the Anode Glow go into the anode with low energy crossing a dark region where they receive energy but it is not enough to excite neutrals again. The Anode Dark Space is featured by an excess of low energy electrons.

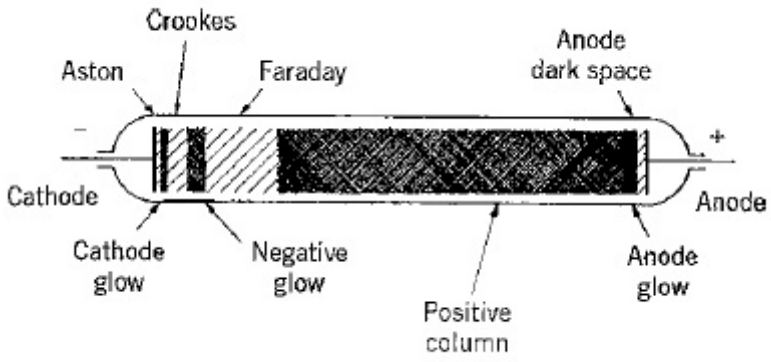

FIGURE 2.1 – A sketch of the bright and dark layers of a DC glow discharge [59].

A DC discharge requires conducting electrodes; however, in some applications as sputter deposition and plasma etching, the electrodes are covered with non-conducting ma-

terials. In this case a DC voltage does not sustain the discharge because the electrode covered with a non-conducting material will charge up to a floating potential resulting in the same fluxes of ions and electrons. There will be only one short-lived discharge. The discharge can be sustained if an AC voltage is applied between the electrodes instead of a DC voltage. However, the time required by the non-conducting electrode charges up has to be less than half of the period of the AC supply otherwise there will be a series of short-lived discharges. Thus, the frequencies used in these discharges are usually in the radio-frequency range (1 KHz – 10^3 MHz). The frequency of 13.54 MHz is the most used because it is the frequency alloted by the international communications authorities to avoid interferences with communications. This kind of discharge is called capacitively coupled (CC) radio-frequency (RF) discharge – radio-frequency because it works in the radio-frequency range and capacitively coupled because the input power is coupled through two electrodes like a capacitor. Figure 2.2 shows a schematic of a reactor for CCPs.

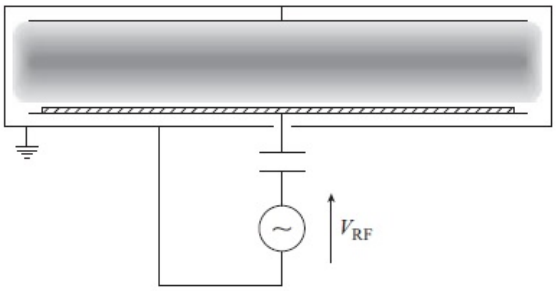

FIGURE 2.2 – Schematic of a reactor for a CCP [60].

The input power can also be coupled by electromagnetic induction. The development of ICPs is due to the requirements of microelectronic industry that searched for plasma sources that could offer a high flux of low energy electrons [59, 60]. In CC RF discharges, voltage and current are not independent; therefore, the increase of ion flux is obtained along with the increase of sheath voltages resulting in high energy ions that damage wafers in plasma processings. The magnetic improvements of cc rf discharges – like RF magnetron also called MEIRE – results in an improvement of power transfer and plasma confinement changing it from the low density plasma source group to the high density plasma source group; however, their applications find limits due to uniformity problems.

In ICPs, RF power is applied to the inductive element which can be a helical conductor in cylindrical geometries or a flat spiral conductor in planar geometries. The RF currents in the inductive element result in a RF magnetic flux that penetrates in the plasma region inducing a RF electric field that provides energy to electrons which ionize gas atom and/or molecules sustaining the plasma. Figure 2.3 shows the RF magnetic and the RF electric fields produced by a planar spiral coupler in an ICP.

It is required a non-conducting wall – called window – to separate the inductive element from the plasma otherwise the RF magnetic field would not penetrate in the plasma region due to electromagnetic shielding. However, degradation and deposition on the windown during the process represent a problem that interferes in the efficiency of power transfer. Low power transfer results in low electron density and excessive heating of the inductive element. The coupling efficiency in planar RF ICPs is analysed in [61].

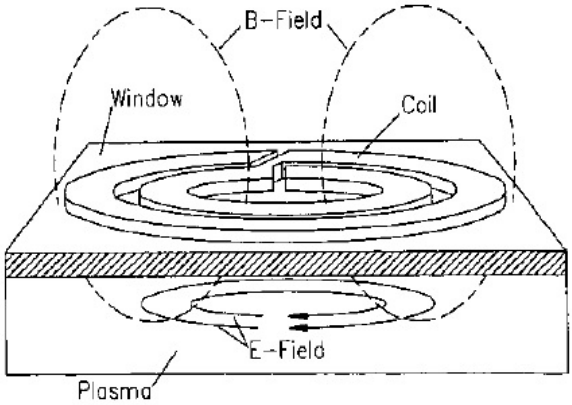

FIGURE 2.3 – The RF magnetic and RF electric fields produced by a planar spiral coupler [62].

Hopwood *et al* [63] studied the electromagnetic fields produced by a planar square coil in a planar RF ICP. The RF magnetic field was measured, the RF electric field was calculated from the measured RF magnetic field, and a finite element analysis program was used to model the electromagnetic fields within a cold collisionless plasma. It was found that the radial component of the RF magnetic field B_{r} – the RF magnetic field is represented in cylindrical coordinates – presents a exponentially decrease as the distance from the window increases. As function of the radius of the chamber, B_{r} has low values in the centre of the chamber, increases up to a maximum value at a distance from the centre around half of the radius of the chamber, then it decreases having low values at the edge of the chamber (see figure 2.4). The axial component of the RF magnetic field B_{z} has a maximum value in the centre of the chamber while the azimuthal component B_{ϕ} is null. The RF electric field, given by the equation [63]

$$\vec{E} \simeq \frac{B_{\mathrm{r}} \exp(-z/\delta)}{i\omega\varepsilon\mu_0\delta}\widehat{\phi}, \tag{2.1}$$

has only the azimuthal component and presents the same radial variation as B_{r}. In Eq. 2.1, ε is the complex plasma permitivity, μ_0 is the permitivity of the free space, ω is the RF frequency, and δ is the skin depth which represents the distance from the window at which the magnetic field is attenuated by a factor of $1/e$. Figure 2.4 shows the RF electric field obtained through finite element analysis. The size of each arrow in this figure is proportional to the magnitude of the RF electric field. Despite of the

assumptions in the model that make the calculations feasible, the modelling results agree with the experimental results.

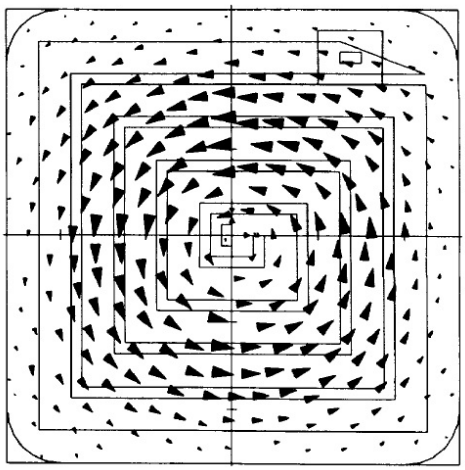

FIGURE 2.4 – The RF electric field within a cold collisionless plasma produced by a planar square coil. It was calculated through a finite element analysis program [63].

The inductive coupling enables high density of ions and low voltages across the plasma sheaths which make it appropriate for many applications [59]. However, ICPs operate at low pressures requiring expensive pumping systems that is an issue in the plasma processing area motivating researches in atmospheric plasma processes [64].

3 Spectroscopic notation

3.1 Spectroscopic notation for atoms

The exact solution of the Schrödinger equation for monoelectronic atoms provides the framework to the study of complex atoms. Obtain the solution of the Schrödinger equation for monoelectronic atoms is facilitated by the spherical symmetry of Coulomb potential that allows to use the variable separation method which give solutions only for discrete values of energy. These energy values are the eigenvalues and the solutions, i.e., the wave functions that satisfy the Schrödinger equation for these energy values, are the eigenfunctions of the Schrödinger equation. The probability density of these eigenfunctions does not depend on time, thus they are steady-states of the system. These steady-states are labelled by three quantum numbers: n, l, and m. The magnetic quantum number m and the orbital quantum number l stem from the angular part of the Schrödinger equation. The solutions of the angular part of the Schrödinger equation are spherical harmonics that depend on l and m. The principal quantum number n stems from the radial part of the Schrödinger equation. The solutions of the radial part of the Schrödinger equation that depend on n and l are expressed through Laguerre polynomials. The discrete values of the energy are determined by the principal quantum number n through the expression [65]:

$$E_{\mathrm{n}} = -\frac{\mu Z^2 e^4}{2\hbar^2 n^2}, \tag{3.1}$$

where Z is the number of protons in the nucleus, e is the elementary charge, $\hbar = h/2\pi$, and $\mu = m_{\mathrm{N}} + m_{\mathrm{e}}/(m_{\mathrm{N}} + m_{\mathrm{e}})$ is the effective mass of the reduced system, i.e., the reduced mass calculated through the mucleus mass m_{N} and the electron mass m_{e}.

They correspond to the energy of the shell that the electron can occupy, therefore n specifies the shell. It has integer values from 1 up to the number of the outermost occupied electron shell ($n = 1, 2, 3, ...$). The orbital quantum number l, which is also called azimuthal quantum number or angular quantum number, corresponds to the subshell occupied by the electron. It also gives the magnitude of the orbital angular momentum $\vec{L}$ which is $L^2 = \hbar^2 l(l+1)$. It has integer values from 0 up to $n-1$ ($l = 0, 1, ..., n-1$). The

magnetic quantum number m corresponds to the orbital within the subshell. It gives the projection of the orbital angular momentum on the z axis $L_{\mathrm{z}} = m\hbar$. It has integer values from $-l$ up to l ($m = -l, ..., 0, ..., l$).

Through measurements of the orbital magnetic dipole moment of the electron, it was identified that the electron has an intrinsic angular momentum which was called spin and represented by $\vec{S}$. The magnitude of the electron spin is given by $S = \sqrt{s(s+1)}\hbar$, where s is the spin quantum number that takes the value $1/2$. The magnitude of the projection of the electron spin on the z axis is given by $S_{\mathrm{z}} = m_{\mathrm{s}}\hbar$, where m_{s} is the spin projection quantum number that has integer values from $-s$ to s ($m_{\mathrm{s}} = -s, ..., s$). Therefore, it can take the values $1/2$ and $-1/2$. The steady-states are now labelled by four quantum numbers: n, l, m_{l}, and m_{s}. The magnetic quantum number that was represented by m changed to m_{l}.

The total angular momentum $\vec{J}$ is given by $\vec{J} = \vec{L} + \vec{S}$. The magnitude of the total angular momentum is calculated by $J = \sqrt{j(j+1)}\hbar$ where j is the main total angular momentum quantum number. The values that j can take are $1/2$ for $l = 0$ and $l + 1/2$ and $l - 1/2$ for $l \neq 0$. The magnitude of the projection of the total angular momentum on the z axis is given by $J_{\mathrm{z}} = m_{\mathrm{j}}\hbar$ where m_{j} is the secondary total angular momentum quantum number that has integer values from $-j$ to j ($m_{\mathrm{j}} = -j, ..., j$). The quantum number m_{l} and m_{s} can be placed by j and m_{j} in the quantum number set that specifies the steady-states of the system. In fact, there are problems where the steady-states have to be specified by n, l, j, and m_{j} as in the calculation of the spin-orbit potential.

The Coulomb potential of complex atoms, i.e., atoms with more than one electron, has terms due to electron-nucleus interactions and terms due to electron-electron interactions. These latter are the non-central part of the potential which forbid to use the variable separation method. Thus, approximate methods try to regain the monoeletronic atom problem. In the Hartree-Fock approximation, there is a Schrödinger equation for each eletron with a Coulomb potential that represents the interaction between the electron and an effective nuclear charge which is the nuclear charge shielded by the other electrons. The steady-state of the system is given by the product of the steady-states of each electron and the energy is given by the sum of the energies of the steady-states of each electron.

Until now, the standard notation of many quantum mechanic books was followed, i.e., the upper case letters L, S, and J are used to represent the module of the orbital angular momentum $\vec{L}$, spin $\vec{S}$, and total angular momentum $\vec{J}$, respectively, while the lower case letters l, s, and j are used to represent quantum numbers associated with these angular momenta. However, it is usual change this notation when dealing with complex atoms due to the need of coupling many angular momenta from many electrons in the atom. Single electron angular momenta are represented by lower case letters while upper case letters are used to represent the angular momenta that result from angular momentum coupling.

For the ith electron in an atom, $\vec{l_i}$ is the orbital angular momentum, l_i is the orbital angular momentum quantum number, $\vec{s_i}$ is the spin, s_i is the spin quantum number, $\vec{j_i}$ is the total angular momentum, and j_i is the main total angular momentum quantum number. As the main two coupling schemes are L-S or Russell-Saunders coupling and j-j coupling which use this notation even in their names, from now on, it will be used this notation.

In the Russell-Saunders coupling, the orbital angular momenta of the electrons are added resulting in the total orbital angular momentum, $\vec{L} = \sum_i \vec{l_i}$, and the spin of the electrons are added resulting in the total spin, $\vec{S} = \sum_i \vec{s_i}$. Then, they are added resulting in the total angular momentum, $\vec{J} = \vec{L} + \vec{S}$. In the j-j coupling, first the total angular momentum is obtained by adding the orbital angular momentum and the spin for each electron, $\vec{j_i} = \vec{l_i} + \vec{s_i}$, then the total angular momentum of the electrons are added resulting in the total angular momentum, $\vec{J} = \sum_i \vec{j_i}$. In light atoms, $\vec{L}$ and $\vec{S}$ are conserved quantities due to weak relativistic effects, but $\vec{L}$ and $\vec{S}$ are no longer conserved quantities in heavy atoms and j-j coupling have to be used. Spin is a quantum phenomenon without a similar classic one. It is obtained through relativistic quantum mechanic, therefore spin-orbit coupling is a relativistic effect. In light atoms, coupling between orbital angular momentum and spin of individual electrons is weak compared to coupling between orbital angular momenta of electrons [66–68].

The configuration of a state shows how the electrons are distributed through the shells and sub-shells in the atom. The oxygen configuration in the ground states is $1s^2 2s^2 2p^4$. In spectrocopical notation, an atom configuration is splited in terms, a term is splited in levels, a level is splited in sub-levels which are the true states of the atom. A term is represented by ${}^{2S+1}L^{(o)}$, where the superscript $2S+1$ is the spin multiplicity, L is the total orbital angular momentum, and the superscript o appears for odd parity terms. The values of L 0, 1, 2, 3, 4, 5... are designated by the upper case letters $S, P, D, F, G, H...$, respectively. A term with $S = 0$ represents a singlet state, with $S = 1/2$ a doublet state, with $S = 1$ a triplet state, and so forth. A level is represented by ${}^{2S+1}L_J^{(o)}$, where the subscript J is the total angular momentum. A level splits into $2J + 1$ sub-levels that are determined by the total magnetic quantum number M_J. To determine the energy ordering of levels and sub-levels, it is used the Hund's rules [69]:

1. For a given configuration, the term with maximum spin multiplicity lies lowest in energy.

2. For a given configuration and spin multiplicity, the term with the largest value of L lies lowest in energy.

3. For atoms with less than half-filled shells, the level with the lowest value of J lies lowest in energy.

4. For atoms with more than half-filled shells, the level with the highest value of J lies lowest in energy.

Oxygen atoms in the ground state have more than half filled subshell. In this case, it is usual to determine the terms by considering vacancies or holes instead of electrons. Thus, the terms for oxygen in the ground states are the same as for carbon in the ground state which are ^{1}S, ^{1}D, and ^{3}P. The latter term is the lowest energy term according to the second Hund's rule. As $L = 1$ and $S = 1$ in the term ^{3}P, J can take the values of 0, 1, and 2, therefore the levels $^3P_0$, $^3P_1$, and $^3P_2$ are possible. According to the fourth Hund's rule, the level $^3P_2$ is the ground state of atomic oxygen.

3.2 Spectroscopic notation for diatomic molecules

Electrons move much faster than nuclei due to their small mass, therefore it is possible to say that they rearrange instantaneously when the nuclei change their positions in a molecule. Thus, the motions of electrons and nuclei can be treated separately as an approximation which is used in the Born-Oppenheimer approximation. Schrödinger equations for electrons are solved for nuclei in fixed positions. From the solutions for different positions of the nuclei, the potential energy curve is obtained for diatomic molecules while the potential energy surface is obtained for polyatomic molecules. Figure 3.1 shows the potential energy curves for the ground state $X^3\Sigma_g^-$ and some of the excited states including the singlet states $a^1\Delta_g$ and $b^1\Sigma_g^+$ of the oxygen molecule.

One can solve exactly the Schrödinger equation for hydrogen atom working in spherical coordinates. Using the Born-Oppenheimer approximation, one can solve exactly only the hydrogen molecule-ion H_2^+ working in ellipsoidal coordinates. As the solutions for hydrogen atom are called atomic orbitals, the solutions for hydrogen molecule-ion H_2^+ are called molecular orbitals. Molecular orbitals can be approximated by linear combinations of atomic orbitals (LCAO). A molecule configuration represents how the electrons are distributed into the molecular orbitals that came from LCAO. The ground state of the oxygen molecule which is $(\sigma_g 1s)^2(\sigma_u^* 1s)^2(\sigma_g 2s)^2(\sigma_u^* 2s)^2(\sigma_g 2p)^2(\pi_u 2p)^4(\pi_g^* 2p)^2$ gives rise to three states: the ground state $^3\Sigma_g^-$ and the two low-lying excited states $^1\Delta_g$ and $^1\Sigma_g^+$.

A molecular term symbol is represented by $^{2S+1}\Lambda$ and a state by $^{2S+1}\Lambda_\Omega$, where Λ is the quantum number of the component of the total orbital angular momentum $\vec{L}$ along the internuclear axis, S is the total spin quantum number that determines the magnitude of the total spin $\vec{S}$, and Ω is the quantum number of the component of $\vec{L} + \vec{S}$ along the internuclear axis. As the component of the total spin $\vec{S}$ along the internuclear axis is Σ, Ω is given by $\Omega =\mid \Lambda + \Sigma \mid$.

The coupling scheme for molecular term symbol of diatomic molecules is the Hund's

case (a) [70, 71]. The orbital angular momenta of electrons are coupled resulting in the total angular momentum $\vec{L}$. The spin of electrons are coupled resulting in the total spin $\vec{S}$. $\vec{L}$ and $\vec{S}$ precess rapidly about the molecular axis with fixed projections $\Lambda\hbar$ and $\Sigma\hbar$, respectively. The quantum number Λ can take the values of 0,1,2,3,... which corresponds to the letters Σ, Π, Δ, Φ, Γ,... , respectively. The quantum number Σ can take the values of $-S, -S+1, ..., S-1, S$. The total angular momentum $\vec{J}$ is given by the sum of the rotational angular momentum $\vec{N}$ and the projection of $\vec{L}+\vec{S}$ on the molecular axis, therefore, in the Hund's case (a), the projection of $\vec{J}$ along the molecular axis is $\Omega\hbar$.

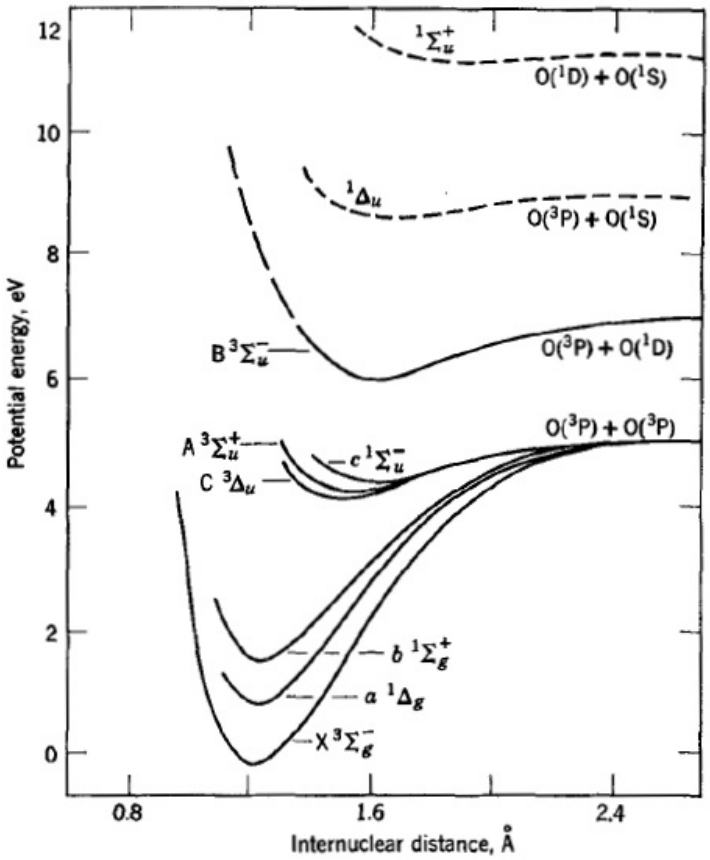

FIGURE 3.1 – Potential energy curves for oxygen molecule [72].

As there are many states with the same term symbol, a letter is added to distinguish them. The letter X is reserved to the ground state, the uppercase letters A, B, C,... are used for excited states with the same multiplicity in order of increasing energy, and the lowercase letters a, b, c,... are used for states that have multiplicity different from the ground state in order of increasing energy. The subscripts g and u came from the german words gerade and ungerade which means even and odd.This symetry property is used to classify homonuclear molecules only. If the wavefunction obtained from LCAO does not change its sign when nuclei are interchanged, then it is even or symmetric to inversion through the center of the molecule and the letter g is added to its molecular term otherwise it is odd or antisymmetric and the letter u is added to its molecular term.

The superscripts + or - that are attached in the Σ states mean that the wavefunction is symmetric or antisymmetric to reflection through a plane that contains the internuclear axis. For $\Lambda > 0$ states, symmetric and antisymmetric componets are present due to degeneracy, therefore no superscript is added to the term.

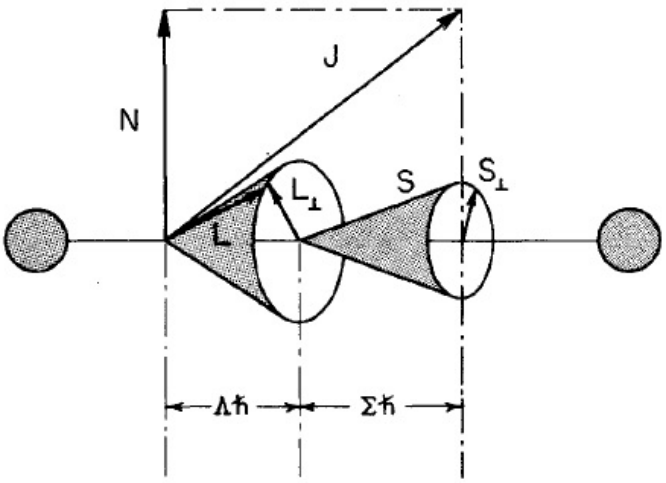

FIGURE 3.2 – The Hund's case (a). [71].

4 Reaction set for oxygen discharge modelling

The oxygen chemistry is complicated due to the presence of metastable atomic and molecular species and their interactions, in particular dissociative attachment and detachment processes, that dictate the negative ion density. It is in particular the two low lying metastable states designated by $a^1\Delta_g$ and $b^1\Sigma_g^+$, which are located 0.98 and 1.627 eV above the ground state, respectively, that can play a significant role in the overall chemistry. The $a^1\Delta_g$ state can be produced in significant amount due to its stability against deactivation by collisions with other molecules and chamber walls. Both these metastable states have approximately the same nuclear separation and similarly shaped potential curves as the ground state $X^3\Sigma_g^-$ [72]. It is well established that collisions with these metastable states have in many cases larger cross sections and thus higher reaction rates than corresponding collisions with the ground state molecule. Thus, these long lived metastable species may be of particular interest as reactive species in the field of plasma medicine [73, 74]. Often the higher $b^1\Sigma_g^+$ state is neglected in modelling studies. In fact, the $b^1\Sigma_g^+$ state is often reported as being present in small concentrations. One reason would be the wall deactivation which is recognized as the major loss channel for both metastable species and ions. Among the few works that address the $b^1\Sigma_g^+$ state wall deactivation, it is reported as being much higher than the $a^1\Delta_g$ state wall deactivation [75–79]. However, recent global model studies have suggested that the $b^1\Sigma_g^+$ state is present in sizeable amounts and plays a significant role in dissociation, ionization and, in particular, it is a significant contributor to the loss of O^- through detachment [43, 44].

The reaction set of the model developed in this work works with the oxygen molecule in the ground state $O_2(X^3\Sigma_g^-)$, the metastable singlet states of the oxygen molecule $O_2(a^1\Delta_g)$ and $O_2(b^1\Sigma_g^+)$, the metastable Herzberg states $O_2(A^3\Sigma_u^+, A'^3\Delta_u, c^1\Sigma_u^-)$, the molecular ions O_2^+ and O_2^-, the oxygen atom in the ground state $O(^3P)$, in the non-Rydberg states, $O(^1D)$, $O(^1S)$, and $O(^3P^o)$, and in the Rydberg states, $O(^5S^o)$ and $O(^3S^o)$, the ions of the atom O^+ and O^-, ozone O_3 and its ions O_3^+ and O_3^-, and electrons. Table 4.1 lists the electron impact reactions, table 4.2 lists the reactions between heavy neutral particles, table 4.3 lists reactions between heavy charged particles, table 4.4 lists the rate of decay of the

metastable species, and table 4.5 lists the wall surface reactions and wall recombination and quenching coefficients. In the tables, the Herzberg states $O_2(A^3\Sigma_u^+$, $A'^3\Delta_u$, $c^1\Sigma_u^-)$ are represented as O_2^H.

The cross sections for reactions 1–22, 27, 28, 39, 42–52, and 54 are available in the literature. For some reactions, it is possible to find different references with different cross sections, therefore each reaction in table 4.1 is followed by the reference that has the cross sections selected for this model. These cross sections were also included in annex A. Given the cross sections, the rate coefficients are calculated by equation 5.2, here assuming a Maxwellian EEDF.

TABLE 4.1 – Electron-impact reactions.

No.	Reaction	Ref.	No.	Reaction	Ref.
1	$e + O_3 \longrightarrow 2e + O_3^+$	[80]	29	$e + O_2(a^1\Delta_g) \longrightarrow e + O_2(b^1\Sigma_g^+)$	[81]
2	$e + O_3 \longrightarrow 2e + O(^3P) + O_2^+$	[80]	30	$e + O_2(a^1\Delta_g) \longrightarrow e + O_2^H$	[81]
3	$e + O_3 \longrightarrow e + O(^3P) + O^+ + O^-$	[80]	31	$e + O_2(a^1\Delta_g) \longrightarrow e + O(^3P) + O(^1D)$	[81]
4	$e + O_3 \longrightarrow O_2(X^3\Sigma_g^-) + O^-$	[82]	32	$e + O_2(b^1\Sigma_g^+) \longrightarrow e + O_2^H$	[81]
5	$e + O_3 \longrightarrow O(^3P) + O_2^-$	[82]	33	$e + O_2(b^1\Sigma_g^+) \longrightarrow 2e + O_2^+$	[81]
6	$e + O_2(X^3\Sigma_g^-) \longrightarrow e + O_2(X^3\Sigma_g^-)$	[33]	34	$e + O_2(b^1\Sigma_g^+) \longrightarrow e + O(^3P) + O(^3P)$	[81]
7	$e + O_2(X^3\Sigma_g^-) \longrightarrow 2e + O_2^+$	[83]	35	$e + O_2(b^1\Sigma_g^+) \longrightarrow 2e + O(^3P) + O^+$	[81]
8	$e + O_2(X^3\Sigma_g^-) \longrightarrow e + O(^3P) + O(^3P)$	[84]	36	$e + O_2(b^1\Sigma_g^+) \longrightarrow e + O_2(X^3\Sigma_g^-)$	[81]
9	$e + O_2(X^3\Sigma_g^-) \longrightarrow 2e + O(^3P) + O^+$	[83]	37	$e + O_2(b^1\Sigma_g^+) \longrightarrow O(^3P) + O^-$	[81]
10	$e + O_2(X^3\Sigma_g^-) \longrightarrow O(^3P) + O^-$	[33]	38	$e + O_2(b^1\Sigma_g^+) \longrightarrow e + O(^3P) + O(^1D)$	[81]
11	$e + O_2(X^3\Sigma_g^-) \longrightarrow e + O^+ + O^-$	[85]	39	$e + O_2^H \longrightarrow O(^3P) + O^-$	[86]
12	$e + O_2(X^3\Sigma_g^-) \longrightarrow e + O_2(rot)$	[84]	40	$e + O_2^H \longrightarrow e + O(^3P) + O(^3P)$	[81]
13	$e + O_2(X^3\Sigma_g^-) \longrightarrow e + O_2(v1)$	[84]	41	$e + O_2^H \longrightarrow e + O(^3P) + O(^1D)$	[81]
14	$e + O_2(X^3\Sigma_g^-) \longrightarrow e + O_2(v2)$	[84]	42	$e + O_2^+ \longrightarrow e + O(^3P) + O^+$	[87]
15	$e + O_2(X^3\Sigma_g^-) \longrightarrow e + O_2(v3)$	[84]	43	$e + O_2^+ \longrightarrow 2e + O^+ + O^+$	[87]
16	$e + O_2(X^3\Sigma_g^-) \longrightarrow e + O_2(v4)$	[84]	44	$e + O_2^+ \longrightarrow O(^3P) + O(^3P)$	[88]
17	$e + O_2(X^3\Sigma_g^-) \longrightarrow e + O_2(a^1\Delta_g)$	[89]	45	$e + O_2^+ \longrightarrow O(^3P) + O(^1D)$	[88]
18	$e + O_2(X^3\Sigma_g^-) \longrightarrow e + O_2(b^1\Sigma_g)$	[89]	46	$e + O(^3P) \longrightarrow e + O(^3P)$	[34]
19	$e + O_2(X^3\Sigma_g^-) \longrightarrow e + O_2^H$	[33]	47	$e + O(^3P) \longrightarrow 2e + O^+$	[90]
20	$e + O_2(X^3\Sigma_g^-) \longrightarrow e + O(^3P) + O(^1D)$	[84]	48	$e + O(^3P) \longrightarrow e + O(^1D)$	[91]
21	$e + O_2(X^3\Sigma_g^-) \longrightarrow e + O(^1D) + O(^1D)$	[84]	49	$e + O(^3P) \longrightarrow e + O(^1S)$	[91]
22	$e + O_2(X^3\Sigma_g^-) \longrightarrow e + O_2(14.7eV)$	[84]	50	$e + O(^3P) \longrightarrow e + O(^3P^o)$	[91]
23	$e + O_2(a^1\Delta_g) \longrightarrow 2e + O_2^+$	[81]	51	$e + O(^3P) \longrightarrow e + O(^5S^o)$	[91]
24	$e + O_2(a^1\Delta_g) \longrightarrow e + O(^3P) + O(^3P)$	[81]	52	$e + O(^3P) \longrightarrow e + O(^3S^o)$	[91]
25	$e + O_2(a^1\Delta_g) \longrightarrow 2e + O(^3P) + O^+$	[81]	53	$e + O(^3P) \longrightarrow e + O^{h*}$	[91]
26	$e + O_2(a^1\Delta_g) \longrightarrow e + O_2(X^3\Sigma_g^-)$	[81]	54	$e + O^- \longrightarrow 2e + O(^3P)$	[92]
27	$e + O_2(a^1\Delta_g) \longrightarrow O(^3P) + O^-$	[93]	55	$e + O(^1D) \longrightarrow 2e + O^+$	[28]
28	$e + O_2(a^1\Delta_g) \longrightarrow O(^1D) + O^-$	[93]	56	$e + O(^1D) \longrightarrow e + O(^3P)$	[81]

The rate coefficients for electron impact ionization (reaction 23), electron impact dissociation (reaction 24), and electron impact dissociative ionization (reaction 25) from the metastable $O_2(a^1\Delta_g)$ are calculated by applying threshold reduction to the rate coefficients for reactions 7, 8, and 9, respectively [81]. It means that the rate coefficients for reactions 7, 8, and 9 are multiplied by $\exp(0.98/T_e)$ in order to reduce the threshold energy since the excitation energy of $O_2(a^1\Delta_g)$ is 0.98 eV. Reaction 26 represents the de-excitation of the metastable $O_2(a^1\Delta_g)$ through electron impact collision and its rate coefficient is calculated by applying the principle of detailed balancing [81]. In this method, the rate coefficient calculated for reaction 17 is multiplied by $(3/2)\exp(0.98/T_e)$ where the exponential factor considers the lowering of the threshold energy for the reverse process and the fraction (3/2) due to the three degenerate states of the ground state of

the oxygen molecule and the two degenerate states of the $O_2(a^1\Delta_g)$. The rate coefficients for reactions 29, 30, and 31 are calculated by applying threshold reduction to the rate coefficients for reactions 18, 19, and 20, respectively [81].

TABLE 4.2 – Collisions among the heavy neutral particles in the oxygen discharge and the rate coefficients.

No.	Reaction	Rate coefficient [m^3/s]	Ref.
57	$O_3 + O_3 \longrightarrow O(^3P) + O_2(X^3\Sigma_g^-) + O_3$	$1.65\times10^{-15}\exp(-11433/T_g)$	[94]
58	$O_3 + O(^1D) \longrightarrow O_2(X^3\Sigma_g^-) + O_2(X^3\Sigma_g^-)$	1.2×10^{-16}	[31]
59	$O_3 + O(^1D) \longrightarrow O_2(X^3\Sigma_g^-) + O(^3P) + O(^3P)$	1.2×10^{-16}	[31]
60	$O_3 + O(^1D) \longrightarrow O_2(X^3\Sigma_g^-) + O_2(a^1\Delta_g)$	2.7×10^{-16}	[31]
61	$O_3 + O(^1D) \longrightarrow O(^3P) + O_3$	2.4×10^{-16}	[31,35]
62	$O_2(X^3\Sigma_g^-) + O_3 \longrightarrow O(^3P) + O_2(X^3\Sigma_g^-) + O_2(X^3\Sigma_g^-)$	$7.26\times10^{-16}\exp(-11400/T_g)$	[31]
63	$O_2(X^3\Sigma_g^-) + O_2(X^3\Sigma_g^-) \longrightarrow O(^3P) + O_3$	$7.972\times10^{-18}\exp(-49824/T_g)$	[95]
64	$O_2(X^3\Sigma_g^-) + O_2(a^1\Delta_g) \longrightarrow O_2(X^3\Sigma_g^-) + O_2(X^3\Sigma_g^-)$	$2.2\times10^{-24}(T_g/300)^{0.8}$	[32]
65	$O_2(X^3\Sigma_g^-) + O_2(a^1\Delta_g) \longrightarrow O(^3P) + O_3$	$2.95\times10^{-27}(T_g/300)^{0.5}$	[96]
66	$O_2(X^3\Sigma_g^-) + O_2(b^1\Sigma_g^+) \longrightarrow O_2(X^3\Sigma_g^-) + O_2(a^1\Delta_g)$	$3.8\times10^{-28}T_g^{2.405}\exp(-200/T_g)$	[97]
67	$O_2(X^3\Sigma_g^-) + O_2(b^1\Sigma_g^+) \longrightarrow O_2(X^3\Sigma_g^-) + O_2(X^3\Sigma_g^-)$	4×10^{-23}	[31,35]
68	$O_2(X^3\Sigma_g^-) + O_2(b^1\Sigma_g^+) \longrightarrow O_2(a^1\Delta_g) + O_2(a^1\Delta_g)$	$2.4\times10^{-24}(T_g/300)^{3.8}\exp(-3080/T_g)$	[31]
69	$O_2(X^3\Sigma_g^-) + O_2^H \longrightarrow O_2(b^1\Sigma_g^+) + O_2(b^1\Sigma_g^+)$	2.9×10^{-19}	[98]
70	$O_2(X^3\Sigma_g^-) + O(^1D) \longrightarrow O(^3P) + O_2(X^3\Sigma_g^-)$	$7\times10^{-18}\exp(67/T_g)$	[98]
71	$O_2(X^3\Sigma_g^-) + O(^1D) \longrightarrow O(^3P) + O_2(a^1\Delta_g)$	1×10^{-18}	[31]
72	$O_2(X^3\Sigma_g^-) + O(^1D) \longrightarrow O(^3P) + O_2(b^1\Sigma_g^+)$	$2.56\times10^{-17}\exp(67/T_g)$	[31,35]
73	$O_2(a^1\Delta_g) + O_3 \longrightarrow O(^3P) + O_2(X^3\Sigma_g^-) + O_2(X^3\Sigma_g^-)$	$6.01\times10^{-17}\exp(-2853/T_g)$	[99]
74	$O_2(a^1\Delta_g) + O_3 \longrightarrow O(^1D) + O_2(X^3\Sigma_g^-) + O_2(X^3\Sigma_g^-)$	1×10^{-17}	[31]
75	$O_2(a^1\Delta_g) + O_3 \longrightarrow O_2(X^3\Sigma_g^-) + O_3$	3×10^{-21}	[100]
76	$O_2(a^1\Delta_g) + O_2(a^1\Delta_g) \longrightarrow O_2(X^3\Sigma_g^-) + O_2(b^1\Sigma_g^+)$	$1.8\times10^{-24}(T_g/300)^{3.8}\exp(700/T_g)$	[101]
77	$O_2(a^1\Delta_g) + O_2(a^1\Delta_g) \longrightarrow O_2(X^3\Sigma_g^-) + O_2(X^3\Sigma_g^-)$	$5.5\times10^{-29}(T_g/300)^{0.5}$	[102]
78	$O_2(b^1\Sigma_g^+) + O_3 \longrightarrow O(^3P) + O_2(X^3\Sigma_g^-) + O_2(X^3\Sigma_g^-)$	1.5×10^{-17}	[35,99]
79	$O_2(b^1\Sigma_g^+) + O_3 \longrightarrow O_2(X^3\Sigma_g^-) + O_3$	3.3×10^{-18}	[35]
80	$O_2(b^1\Sigma_g^+) + O_3 \longrightarrow O_2(a^1\Delta_g) + O_3$	3.3×10^{-18}	[35]
81	$O_2(b^1\Sigma_g^+) + O_2(b^1\Sigma_g^+) \longrightarrow O_2(X^3\Sigma_g^-) + O_2(a^1\Delta_g)$	$3.6\times10^{-23}(T_g/300)^{0.5}$	[96]
82	$O(^3P) + O_3 \longrightarrow O_2(X^3\Sigma_g^-) + O_2(X^3\Sigma_g^-)$	$1.8\times10^{-17}\exp(-2300/T_g)$	[31]
83	$O(^3P) + O_3 \longrightarrow O(^3P) + O(^3P) + O_2(X^3\Sigma_g^-)$	$2.9\times10^{-16}\exp(-11400/T_g)$	[103]
84	$O(^3P) + O_3 \longrightarrow O_2(X^3\Sigma_g^-) + O_2(a^1\Delta_g)$	$1\times10^{-17}\exp(-2300/T_g)$	[31]
85	$O(^3P) + O_3 \longrightarrow O_2(X^3\Sigma_g^-) + O_2(b^1\Sigma_g^+)$	$2.8\times10^{-21}\exp(-2300/T_g)$	[31]
86	$O(^3P) + O_2(a^1\Delta_g) \longrightarrow O(^3P) + O_2(X^3\Sigma_g^-)$	1.3×10^{-22}	[104]
87	$O(^3P) + O_2(b^1\Sigma_g^+) \longrightarrow O(^3P) + O_2(a^1\Delta_g)$	4×10^{-20}	[105]
88	$O(^3P) + O_2(b^1\Sigma_g^+) \longrightarrow O(^3P) + O_2(X^3\Sigma_g^-)$	4×10^{-20}	[105]
89	$O(^3P) + O_2^H \longrightarrow O(^3P) + O_2(X^3\Sigma_g^-)$	4.95×10^{-18}	[106]
90	$O(^3P) + O_2^H \longrightarrow O(^1D) + O_2(a^1\Delta_g)$	2.7×10^{-18}	[106]
91	$O(^3P) + O_2^H \longrightarrow O(^1D) + O_2(b^1\Sigma_g^+)$	1.35×10^{-18}	[106]
92	$O(^3P) + O(^1D) \longrightarrow O(^3P) + O(^3P)$	8×10^{-18}	[107]

There are no cross sections available in the literature for electron impact on $O_2(b^1\Sigma_g^+)$ (reactions 32–38). The rate coefficients for all of these reactions are calculated by threshold reduction from the ground state except the rate coefficient for de-excitation of the $O_2(b^1\Sigma_g^+)$ (reaction 36) which is calculated by the principle of detailed balancing [81]. Thus, the rate coefficient for reaction 36 is calculated through the rate coefficient for reaction 18 which is multiplied by $3\exp(1.627/T_e)$, where the factor 3 is due to the three degenerate states of the $O_2(b^1\Sigma_g^+)$ and 1.627 inside the exponential is due to the threshold energy for the reverse process. The rate coefficients for dissociation of the Herzberg states $O_2(A^3\Sigma_u^+, A'^3\Delta_u, c^1\Sigma_u^-)$ (reactions 40 and 41) are calculated by applying threshold reduction to reactions 8 and 20, respectively, where the exponential factor is $\exp(4.34/T_e)$ [81].

In reaction 53, O^{h*} represents all the excited states of the atomic oxygen excluding

the non-Rydberg states, $O(^1D)$, $O(^1S)$, and $O(^3P^o)$, and the Rydberg states, $O(^5S^o)$ and $O(^3S^o)$. The cross sections utilized to calculate the rate coefficient for this reaction is given by subtracting the cross sections for the excited states $O(^1D)$, $O(^1S)$, $O(^3P^o)$, $O(^5S^o)$, and $O(^3S^o)$ from the total $e + O(^3P) \longrightarrow e + O^*$ excitation cross section without autoionization [91]. The rate coefficient for electron impact ionization of the metastable oxygen atom $O(^1D)$ (reaction 55) is calculated by threshold reduction of the rate coefficient for reaction 47 with $\exp(1.96/T_e)$ as the exponential factor. The rate coefficient for reaction 56 (de-excitation of the $O(^1D)$ by electron impact) is calculated by detailed balancing [81]. For this reaction, the rate coefficient for reaction 48 is multiplied by $(9/5)\exp(1.96/T_e)$, where the exponential factor considers the lowering of the threshold energy for the reverse process and the fraction (9/5) due to the nine degenerate states of the ground states of the oxygen atom and the five degenerate states of the metastable oxygen atom $O(^1D)$.

TABLE 4.3 – Collisions involving the heavy charged particles in the oxygen discharge and the rate coefficients.

No.	Reaction	Rate coefficient [m^3/s]	Ref.
93	$O_3^- + O_2(X^3\Sigma_g^-) \longrightarrow e + O_2(X^3\Sigma_g^-) + O_3$	2.3×10^{-17}	[31]
94	$O_3^- + O(^3P) \longrightarrow O_2(X^3\Sigma_g^-) + O_2^-$	1×10^{-16}	[31]
95	$O_3^- + O(^3P) \longrightarrow e + O_2(X^3\Sigma_g^-) + O_2(X^3\Sigma_g^-)$	3×10^{-16}	[31]
96	$O_3^- + O_2^+ \longrightarrow O_2(X^3\Sigma_g^-) + O_3$	$2\times10^{-14}(T_g/300)^{0.5}$	[52]
97	$O_3^- + O_2^+ \longrightarrow O(^3P) + O(^3P) + O_3$	$2\times10^{-14}(T_g/300)^{0.5}$	[52]
98	$O_3^- + O^+ \longrightarrow O(^3P) + O_3$	$2\times10^{-14}(T_g/300)^{0.5}$	[52]
99	$O_2^- + O_3 \longrightarrow O_2(X^3\Sigma_g^-) + O_3^-$	1.3×10^{-15}	[108]
100	$O_2^- + O_2(X^3\Sigma_g^-) \longrightarrow e + O_2(X^3\Sigma_g^-) + O_2(X^3\Sigma_g^-)$	$2.7\times10^{-16}(T_g/300)^{0.5}\exp(-5590/T_g)$	[32]
101	$O_2^- + O_2(a^1\Delta_g) \longrightarrow e + O_2(X^3\Sigma_g^-) + O_2(X^3\Sigma_g^-)$	2×10^{-16}	[109]
102	$O_2^- + O_2(b^1\Sigma_g^+) \longrightarrow e + O_2(X^3\Sigma_g^-) + O_2(X^3\Sigma_g^-)$	3.6×10^{-16}	[31]
103	$O_2^- + O(^3P) \longrightarrow O_2(X^3\Sigma_g^-) + O^-$	1.755×10^{-16}	[110]
104	$O_2^- + O(^3P) \longrightarrow e + O_3$	2.145×10^{-16}	[110]
105	$O_2^- + O_2^+ \longrightarrow O_2(X^3\Sigma_g^-) + O_2(X^3\Sigma_g^-)$	$2\times10^{-14}(T_g/300)^{0.5}$	[52]
106	$O_2^- + O_2^+ \longrightarrow O(^3P) + O(^3P) + O_2(X^3\Sigma_g^-)$	$2\times10^{-14}(T_g/300)^{0.5}$	[52]
107	$O_2^- + O^+ \longrightarrow O(^3P) + O_2(X^3\Sigma_g^-)$	$2\times10^{-14}(T_g/300)^{0.5}$	[52]
108	$O^- + O_3 \longrightarrow O(^3P) + O_3^-$	1.4×10^{-15}	[108]
109	$O^- + O_3 \longrightarrow e + O_2(X^3\Sigma_g^-) + O_2(X^3\Sigma_g^-)$	$3.01\times10^{-16}(T_g/300)^{0.5}$	[96]
110	$O^- + O_3 \longrightarrow O_2(X^3\Sigma_g^-) + O_2^-$	0.3×10^{-15}	[108]
111	$O^- + O_2(X^3\Sigma_g^-) \longrightarrow e + O_3$	5×10^{-21}	[32]
112	$O^- + O_2(X^3\Sigma_g^-) \longrightarrow e + O(^3P) + O_2(X^3\Sigma_g^-)$	2.4×10^{-18}	[31, 95]
113	$O^- + O_2(X^3\Sigma_g^-) \longrightarrow O(^3P) + O_2^-$	6.9×10^{-17}	[111]
114	$O^- + O_2(a^1\Delta_g) \longrightarrow O(^3P) + O_2^-$	4.75×10^{-17}	[112]
115	$O^- + O_2(a^1\Delta_g) \longrightarrow e + O_3$	1.42×10^{-16}	[112]
116	$O^- + O_2(b^1\Sigma_g^+) \longrightarrow e + O(^3P) + O_2(X^3\Sigma_g^-)$	6.9×10^{-16}	[113]
117	$O^- + O(^3P) \longrightarrow e + O_2(X^3\Sigma_g^-)$	2.3×10^{-16}	[112]
118	$O^- + O_2^+ \longrightarrow O(^3P) + O_2(X^3\Sigma_g^-)$	$2.6\times10^{-14}(300/T_g)^{0.44}$	[114]
119	$O^- + O_2^+ \longrightarrow O(^3P) + O(^3P) + O(^3P)$	$2.6\times10^{-14}(300/T_g)^{0.44}$	[114]
120	$O^- + O^+ \longrightarrow O(^3P) + O(^3P)$	$4\times10^{-14}(300/T_g)^{0.43}$	[114]
121	$O_2(X^3\Sigma_g^-) + O^+ \longrightarrow O(^3P) + O_2^+$	$2\times10^{-17}(300/T_g)^{0.5}$	[31]
122	$O_3 + O^+ \longrightarrow O_2(X^3\Sigma_g^-) + O_2^+$	1×10^{-16}	[32]
123	$O_2(a^1\Delta_g) + O^+ \longrightarrow O(^3P) + O_2^+$	2×10^{-17}	[100]

Table 4.2 presents collisions involving the heavy neutral particles. The rate coefficients are for the most part taken directly from the literature, mainly from the collections of Eliasson and Kogelshatz [31] and Baulch *et al.* [35]. For reaction 66, we made a new fit to the data of Borrell *et al.* [97] as there was an inconsistency in the literature [32, 115]. For reaction 67, we use the rate coefficient of 4×10^{-23} m^3/s for quenching of the metastable

$O_2(b^1\Sigma_g^+)$ by the molecular oxygen in the ground state as recommended by Baulch *et al.* [35] which are based on the measurements realized by Martin *et al.* [116] and Lawton *et al.* [117].

The rate coefficient for the quenching of $O_2(b^1\Sigma_g^+)$ by $O(^3P)$,

$$O(^3P) + O_2(b^1\Sigma_g^+) \longrightarrow \text{products},$$

has been measured by Slanger and Black [105] to be 8×10^{-20} m^3/s. We assume half leads to creation of the oxygen molecule in the ground state $O_2(X^3\Sigma_g^-)$ and the other half leads to the metastable oxygen molecule $O_2(a^1\Delta_g)$, thus reactions 87 and 88, respectively.

Table 4.3 presents the reactions among the heavy charged particles. The rate coefficients for mutual neutralization among O_3^- and O_2^+ (reactions 96 and 97), O_3^- and O^+ (reaction 98), O_2^- and O_2^+ (reactions 105 and 106), and O_2^- and O^+ (reaction 107) are assumed to be $2\times10^{-14}(T_g/300)^{0.5}$ in agreement with the mutual neutralization among O^- and O_2^+ (reactions 118 and 119) and O^- and O^+ (reaction 120) as discussed elsewhere [114]. Also, this is consistent with recent experimental measurements of rate coefficients for ion-ion mutual neutralization involving the halide anions Cl^-, Br^-, and I^- [118].

TABLE 4.4 – Decay of metastable species.

No.	Reaction	Decay rate [s^{-1}]	Ref.
124	$O_2^H \longrightarrow O_2(X^3\Sigma_g^-) + h\nu$	6.25	[119]
125	$O_2(b^1\Sigma_g^+) \longrightarrow O_2(X^3\Sigma_g^-) + h\nu$	0.14	[31]
126	$O_2(a^1\Delta_g) \longrightarrow O_2(X^3\Sigma_g^-) + h\nu$	2.256×10^{-4}	[120]
127	$O(^1D) \longrightarrow O(^3P) + h\nu$	6.8×10^{-3}	[31]

The rate of decay of the metastable species are listed in table 4.4. The $O_2(a^1\Delta_g)$ has the lowest rate decay, therefore its long radiative lifetime enables potential applications [121], since as this excited state is more reactive than the ground state. Table 4.5 lists the surface reactions and the wall quenching and recombination coefficients. We assume here that the wall recombination coefficient for oxygen atoms on stainless steel surfaces depends on pressure through $\gamma_O = 0.1438\exp(2.5069/p)$ for pressures above 2 mTorr and $\gamma_O = -0.25p + 1$ for pressures under 2 mTorr [122]. The pressure dependence on the wall recombination coefficient was achieved by fitting all the available data for stainless steel surfaces. The same wall recombination coefficient was used for $O(^1D)$ as no data is available. The wall quenching coefficient for $O_2(a^1\Delta_g)$ on stainless steel surfaces was assumed to be 0.007 [123] and the wall quenching coefficients for $O(^1D)$, $O_2(b^1\Sigma_g^+)$, and $O_2(A^3\Sigma_u^+, A'^3\Delta_u, c^1\Sigma_u^-)$ were assumed to be 0.1 [79]. This assumption is based on the findings that the wall quenching coefficient for $b^1\Sigma_g^+$ state is about 100 times higher than for the $^1\Delta_g$ state [76, 77] as no direct measurements exist. Interactions between O_3 and surface are neglected [122]. The negative ions do not react with the walls due to the sheath potential, therefore they are lost by recombination and detachment reactions in the bulk

of the plasma. The ion-neutral cross section σ_{ion} necessary to calculate the ion-neutral mean free path λ_{ion} was assumed to be $\sigma_{\text{ion}} = 7.5 \times 10^{-19}$ m^2 [124] for O^+, O_2^+, and O_3^+ and the same value was used for the neutral mean free path λ_{n} to calculate the h factor for neutrals.

TABLE 4.5 – Quenching coefficients and recombination coefficients for stainless steel surfaces and surface reactions.

No.	Reaction	γ–stainless steel	Ref.
128	$O_2(a^1\Delta_g) \longrightarrow O_2(X^3\Sigma_g^-)$	0.007	[123]
129	$O_2(b^1\Sigma_g^+) \longrightarrow O_2(X^3\Sigma_g^-)$	0.1	[79]
130	$O_2^H \longrightarrow O_2(X^3\Sigma_g^-)$	0.1	[79]
131	$O(^3P) \longrightarrow (1/2)O_2(X^3\Sigma_g^-)$	$0.1438\exp(2.5069/p)$	[122]
132	$O(^1D) \longrightarrow (1/2)O_2(X^3\Sigma_g^-)$	$0.1438\exp(2.5069/p)$	[122]
133	$O(^1D) \longrightarrow O(^3P)$	0.1	[79]
134	$O_3^+ \longrightarrow O_3$		
135	$O_2^+ \longrightarrow O_2(X^3\Sigma_g^-)$		
136	$O^+ \longrightarrow O(^3P)$		

For calculations supposing an anodized aluminium reactor walls, the recombination coefficient for atomic oxygen at the walls is assumed to be a constant $\gamma_{\text{O}} = 0.06$ based on the measurements of Guha *et al* [125]. The same value was assumed for the wall recombination coefficient for $O(^1D)$.

It would be possible neglect the $O_2(a^1\Delta_g)$ loss at the anodized aluminium walls since O'Brien and Myers [76] reported a null percentage of $O_2(a^1\Delta_g)$ deactivation by aluminium spiral wires and Sharpless and Slanger [123] reported that the surface loss-rate coefficient for aluminium would be less than 10^{-3}. Du *et al* [126] studied the $O_2(a^1\Delta_g)$ deactivation on copper, chromium, nickel, and silver. According this study, copper would be more effective to $O_2(a^1\Delta_g)$ deactivation than chromium, nickel, and silver; however, the $O_2(a^1\Delta_g)$ deactivation would be higher on silver surfaces than copper surfaces according to Sharpless and Slanger [123]. Moreover Du *et al* [126] reported that the quenching probability for $O_2(a^1\Delta_g)$ would be in the range $1 - 2 \times 10^{-4}$ for chromium and $0.6 - 1 \times 10^{-4}$ for nickel while Sharpless and Slanger [123] reported that the surface loss-rate coefficient would be 0.011 for nickel and 0.002 for chromium. Therefore, chromium would be almost as inert as aluminium. Due to these contradictory results for the quenching of $O_2(a^1\Delta_g)$, the quenching coefficient for stainless steel surfaces, which has been assumed as 0.007 [123], was also assumed for anodized aluminium surfaces in this work.

There are even less data for the quenching coefficients for $O_2(b^1\Sigma_g^+)$, $O_2(A^3\Sigma_u^+$, $A'^3\Delta_u$, $c^1\Sigma_u^-)$, and $O(^1D)$. According to O'Brien and Myers [76], 25 % of $O_2(b^1\Sigma_g^+)$ would be quenched on aluminium spiral wires and 30 % on iron spiral wires while aluminium spiral wires and iron spiral wires would be inert to $O_2(a^1\Delta_g)$ quenching as mentioned above. Quenching of $O_2(b^1\Sigma_g^+)$ on Pyrex walls was also reported as been higher than quenching of $O_2(a^1\Delta_g)$ [75,77,78]. Thorsteinsson and Gudmundsson [79] attributed 0.1 for the quenching coefficients of $O_2(b^1\Sigma_g^+)$ and $O_2(A^3\Sigma_u^+$, $A'^3\Delta_u$, $c^1\Sigma_u^-)$ on stainless steel walls. Here,

it was assumed that these quenching coefficients are also valid for anodized aluminium walls. This can not be a gross assumption since the difference between aluminium spiral wires and iron spiral wires is small for quenching of $O_2(b^1\Sigma_g^+)$ [76].

5 The Volume Averaged Global Model

According to the microscopic theory, a plasma is studied considering the interactions that all particles that compound it are subjected, i.e., the interactions between all particles and the interactions between charged particles and electromagnetic fields present in the plasma. The great number of particles in the plasma results in many equations to be solved making the mathematical solution extremely hard. Despite of the simplifications that are necessary to make the calculations feasible, particle-in-cell (PIC) computer modelling works in the microscopic level which explain why it is the most time-consuming model in plasma physics [127].

To avoid the heavy calculations of the microscopic theory, plasmas are studied through statistical theories as the kinetic theory and the fluid theory. In the kinetic theory, a distribution function is defined in a phase space for each kind of particle and how these distribution functions change in time and space is determined by the Boltzmann's equation. The macroscopic variables that describe the plasma are calculated through the momentums of the distribution functions. However, solve the Boltzmann's equation to obtain the distribution function is usually a hard work. One can avoid this problem resorting to the fluid theory which works with the macroscopic transport equations obtained from the momentums of the Boltzmann's equation.

From the continuity equation, which is one of the fluid equations, it is possible to derive the balance equations used in the volume averaged global model [60]. This model is based on a system of linear differential equations which includes a particle balance equation for each of the heavy particle considered in the model and an energy balance equation. In addition a charge neutrality is assumed which gives the density of electrons. These equations are solved to obtain the plasma parameters and density of species.

The particle balance equations can be written as [52]:

$$V\frac{\mathrm{d}n}{\mathrm{d}t} = Q + \sum_i k_i lmV_i - \sum_j k_j mnV_j + \sum_r \Gamma_r S - \Gamma S + k_{\mathrm{pump}} n. \tag{5.1}$$

On the left hand side (LHS), V is the reactor volume and n is the volume averaged density of a species. On the right hand side (RHS), Q is the flow rate of the input gas and the second term represents the particle gain (n increase) through collision reactions between species which have densities represented by l and m. These reactions can involve collisions between electron and molecule, atom or ion; molecule and molecule, atom or ion; atom and atom or ion; or ion and ion. The k_i are the rate coefficients for gain reactions and V_i can be the effective volume for negative ions V_-, the effective volume for recombination V_{rec}, or the reactor volume V [36, 37]. The third term on the RHS represents the particle loss (n decrease) through collision reactions between the species, which density is represented by n, and electron, molecule, atom or ion. The k_j are the rate coefficients for loss reactions and V_j depends on reaction type as explained for V_i. The Γ_r is the flux of other particle species to the walls that results in particle gain due to surface interactions, Γ is the particle flux that is lost to the wall, S is the inner area of the reactor, and k_{pump} is the pumping rate. Not all of these terms are present in the balance equations for all species. The reaction set determines which of the terms are present for a given particle.

The rate coefficients for the electron-impact reactions are calculated by [48]

$$k(T_{\mathrm{eff}}) = \left(\frac{2e}{m_{\mathrm{e}}}\right)^{1/2} \int_0^\infty \sigma(\varepsilon)\varepsilon^{1/2} f(\varepsilon)\,\mathrm{d}\varepsilon, \tag{5.2}$$

where T_{eff} is the effective electron temperature, e is the elementary charge, m_{e} is the electron mass, ε is the electron energy, $\sigma(\varepsilon)$ is the cross section, and $f(\varepsilon)$ is the EEDF. The concept of effective electron temperature have to be used for non-Maxwellian distribution functions since these distribution functions are characteristics from non-equilibrium steady states [128]. To study the effects of different electron energy distribution functions on the plasma parameters, the general distribution function [47]

$$f(\varepsilon) = c_1\varepsilon^{1/2}\exp(-c_2\varepsilon^x) \tag{5.3}$$

was used. The parameter x defines the shape of the distribution. For $x = 1$ equation 5.3 represents a Maxwellian distribution while for $x = 2$ the EEDF is the Druyvesteyn distribution. If $x = 0.5$ the EEDF is concave and could represent the EEDF in a low pressure capacitively coupled discharge. The expressions for c_1 and c_2 are [47]

$$c_1 = \frac{x}{\langle\varepsilon\rangle^{3/2}} \frac{[\Gamma(\xi_2)]^{3/2}}{[\Gamma(\xi_1)]^{5/2}} \tag{5.4}$$

and

$$c_2 = \frac{1}{\langle\varepsilon\rangle^x}\left[\frac{\Gamma(\xi_2)}{\Gamma(\xi_1)}\right]^x, \tag{5.5}$$

where $\langle\varepsilon\rangle$ is the mean electron energy, $\xi_1 = 3/2x$ and $\xi_2 = 5/2x$. The factors c_1 and c_2 are determined through the equation for normalization of the distribution function and the equation for the mean energy of electrons as discussed by Gudmundsson [47]. The mean electron energy is given by [47]

$$\langle\varepsilon\rangle = \frac{3}{2}k_{\mathrm{B}}T_{\mathrm{eff}}, \tag{5.6}$$

where k_{B} is the Boltzmann constant.

In order to apply threshold reduction the cross sections are calculated through [79]

$$\sigma_{\mathrm{tr}}(\varepsilon) = \left(1 + \frac{\varepsilon_{\mathrm{a}}}{\varepsilon}\right)\sigma(\varepsilon + \varepsilon_{\mathrm{a}}) \tag{5.7}$$

and for detailed balancing through [79]

$$\sigma_{\mathrm{db}}(\varepsilon) = \left(1 + \frac{\varepsilon_{\mathrm{a}}}{\varepsilon}\right)\frac{g_{\mathrm{x}}}{g_{\mathrm{x}^*}}\sigma(\varepsilon + \varepsilon_{\mathrm{a}}), \tag{5.8}$$

where ε_{a} is the energy threshold of the excitation reaction, g_{x} is the degeneracy of the unexcited state, and g_{x^*} is the degeneracy of the excited state.

The energy balance equation is expressed as [59]:

$$V\frac{\mathrm{d}W_{\mathrm{e}}}{\mathrm{d}t} = P_{\mathrm{abs}} - P_{\mathrm{loss}}, \tag{5.9}$$

where W_{e} denotes the electron energy density, P_{abs} is the absorbed power by plasma, and P_{loss} is the loss power. The electron energy density W_{e} is [59]

$$W_{\mathrm{e}} = \frac{3}{2}en_{\mathrm{e}}T_{\mathrm{eff}}, \tag{5.10}$$

where n_{e} is the electron density. The loss power P_{loss} is given by [59]

$$P_{\mathrm{loss}} = P_{\mathrm{ev}} + P_{\mathrm{ew}} + P_{\mathrm{iw}}, \tag{5.11}$$

where P_{ev} is the power lost due to electron-particle interactions in the reactor volume

$$P_{\mathrm{ev}} = en_{\mathrm{e}}V\sum_i k_{\mathrm{iz},i}n_i\varepsilon_{\mathrm{c},i}, \tag{5.12}$$

P_{ew} is the power lost due to electron-wall interactions

$$P_{\mathrm{ew}} = eS\varepsilon_{\mathrm{ew}} n_{\mathrm{es}} u_{\mathrm{B}}, \tag{5.13}$$

and P_{iw} is the power lost due to ion-wall interactions

$$P_{\mathrm{iw}} = eS\varepsilon_{\mathrm{iw}} \sum_j n_{+\mathrm{s},j} u_{\mathrm{B},j}. \tag{5.14}$$

In equation 5.12, $k_{\mathrm{iz},i}$ is the ionization rate coefficient, n_i represents the densities of particles which collide with electrons, and $\varepsilon_{\mathrm{c},i}$ is the collisional energy loss per electron-ion pair created. In equation 5.13, $\varepsilon_{\mathrm{ew}}$ is the mean kinetic energy lost per electron lost, n_{es} is the electron density at sheath-edge, and u_{B} is the average Bohm velocity. In equation 5.14, $\varepsilon_{\mathrm{iw}}$ is the mean kinetic energy lost per ion lost, $n_{+\mathrm{s},j}$ represents the positive ion densities at sheath-edge, and $u_{\mathrm{B},j}$ is the Bohm velocity for positive ion species j. The mean kinetic energy lost per electron lost $\varepsilon_{\mathrm{ew}}$ is given by [47]

$$\varepsilon_{\mathrm{ew}} = \frac{\Gamma(\xi_1)\Gamma(\xi_5)}{\Gamma(\xi_2)\Gamma(\xi_4)} \langle\varepsilon\rangle \tag{5.15}$$

and the mean kinetic energy lost per ions lost $\varepsilon_{\mathrm{iw}}$ is given by [47]

$$\varepsilon_{\mathrm{iw}} = \frac{[\Gamma(\xi_1)]^2}{\Gamma(\xi_2)\Gamma(\xi_3)} \langle\varepsilon\rangle + V_{\mathrm{s}}. \tag{5.16}$$

In these equations, $\xi_3 = 1/2x$, $\xi_4 = 2/x$, $\xi_5 = 3/x$, and V_{s} is the sheath potential which is calculated through the balance of electron and negative ion fluxes to the positive ion flux at the sheath edge. However, the negative ion flux is found to be always negligible as expected [59]. For a Maxwellian EEDF, Eq. 5.15 reduces to $\varepsilon_{\mathrm{ew}} = 2T_{\mathrm{e}}$ and Eq. 5.16 reduces to $\varepsilon_{\mathrm{iw}} = T_{\mathrm{e}}/2 + V_{\mathrm{s}}$.

The collisional energy loss per electron-ion pair created is given by [59]:

$$\varepsilon_{\mathrm{c}} = \varepsilon_{\mathrm{iz}} + \sum_i \left(\frac{k_{\mathrm{diss},j}}{k_{\mathrm{iz}}} \varepsilon_{\mathrm{diss},j} \right) + \sum_j \left(\frac{k_{\mathrm{ex},j}}{k_{\mathrm{iz}}} \varepsilon_{\mathrm{ex},j} \right) + \frac{k_{\mathrm{elas}}}{k_{\mathrm{iz}}} \frac{3m_{\mathrm{e}}}{m_{\mathrm{ion}}} T_{\mathrm{eff}}, \tag{5.17}$$

where $\varepsilon_{\mathrm{iz}}$ is the ionization threshold energy, $k_{\mathrm{diss},j}$ represent the dissociation rate coefficients, $\varepsilon_{\mathrm{diss},j}$ represents the dissociation threshold energy, $k_{\mathrm{ex},j}$ represents the excitation rate coefficients, $\varepsilon_{\mathrm{ex},j}$ represents the excitation threshold energy, k_{elas} is the rate coefficient for elastic collisions between electrons and neutral species, and m_{ion} is the mass of the ion.

In equation 5.14, the positive ion density at the sheath-edge $n_{+\mathrm{s}}$ is related to the positive ion density at the discharge centre through the h factor – the edge-to-centre plasma

density ratio – which applies for two electronegative discharge regimes: a two-region low pressure regime with a parabolic electronegative core surrounded by an electropositive edge h_a and a one-region flat-topped electronegative profile h_c. For a cylindrical reactor like that supposed in this model, the h_a factor at the axial walls is calculated through an expression different of that for the h_a factor at the radial wall. For axial walls, it is given by [36, 37]

$$h_{a,L} \simeq \frac{0.86}{(1+\alpha_0)\left[3+(\eta L/2\lambda_{ion})\right]^{1/2}} \tag{5.18}$$

and the h_a factor for radial wall is [36, 37]

$$h_{a,R} \simeq \frac{0.8}{(1+\alpha_0)\left[4+(\eta R/\lambda_{ion})\right]^{1/2}}. \tag{5.19}$$

In equations 5.18 and 5.19, L is the length of the reactor, R is the radius of the reactor, $\eta = 2T_+/(T_+ + T_-)$, T_+ is the positive ion temperature, T_- is the negative ion temperature, λ_{ion} is the ion-neutral mean free path, and α_0 is the central electronegativity. The ion-neutral mean free path λ_{ion} is calculated through $\lambda_{ion} = 1/n_g\sigma_{ion}$ where n_g is the gas density and σ_{ion} is the ion-neutral cross section [36, 37]. The central electronegativity α_0 relates with the average electronegativity α through $\alpha_0 V_- = \alpha V$ [36, 37]. For radial and axial walls, the h_c factor is calculated through the same expression which is given by [36, 37]

$$h_c \simeq \frac{1}{{\gamma_-}^{1/2} + (n_+/n_-)(\gamma_+ n_*/n_-)^{1/2}}, \tag{5.20}$$

where $\gamma_- = T_{eff}/T_-$, $\gamma_+ = T_{eff}/T_+$, and [36, 37]

$$n_* = \frac{15\eta^2 v_{th}}{56 k_{rec}\lambda_{ion}}. \tag{5.21}$$

In the equation above, k_{rec} is the average rate coefficient for mutual neutralizations and v_{th} is the mean thermal velocity of the ions which is calculated through [59]

$$v_{th} = \left(\frac{8k_B T_+}{\pi m_{ion}}\right)^{1/2}. \tag{5.22}$$

The positive ion temperature T_+ and the negative ion temperature T_- are assumed to be equal to the gas temperature. The h factor is calculated through $h_L = ({h_{a,L}}^2 + {h_c}^2)^{1/2}$ for axial wall and $h_R = ({h_{a,R}}^2 + {h_c}^2)^{1/2}$ for radial walls.

For the general EEDF represented by equation 5.3, the Bohm velocity for an elec-

tropositive plasma is given by [47]

$$u_{\mathrm{B}} = \langle \varepsilon \rangle^{1/2} \left(\frac{2}{m_{\mathrm{ion}}} \right)^{1/2} \frac{\Gamma(\xi_1)}{[\Gamma(\xi_2)\Gamma(\xi_3)]^{1/2}}, \tag{5.23}$$

where m_{ion} is the ion mass. For a Maxwellian EEDF, Eq. 5.23 becomes

$$u_{\mathrm{B}} = \left(\frac{eT_{\mathrm{e}}}{m_{\mathrm{ion}}} \right)^{1/2}. \tag{5.24}$$

One should keep in mind that Eq. 5.23 and 5.24 are valid for an electropositive plasma with one species of positive ion. They can be used for an electropositive plasma with more than one species of positive ion as an approximation. For an electronegative plasma, Eq. 5.24 changes to [59]

$$u_{\mathrm{B}} = \left[\frac{eT_{\mathrm{e}}(1+\alpha_{\mathrm{s}})}{m_{\mathrm{ion}}(1+\alpha_{\mathrm{s}}\gamma_{-})} \right]^{1/2}. \tag{5.25}$$

The parameter α_s is the electronegativity at sheath-edge which can be calculated through [129]

$$\alpha_{\mathrm{s}} = \alpha \exp \left[\frac{(1+\alpha_{\mathrm{s}})(1-\gamma_{-})}{2(1+\alpha_{\mathrm{s}}\gamma_{-})} \right]. \tag{5.26}$$

As an attempt to include the negative ion effects in Eq. 5.23, it was modified to

$$u_{\mathrm{B}} = \langle \varepsilon \rangle^{1/2} \left(\frac{2}{m_{\mathrm{ion}}} \right)^{1/2} \left[\frac{(1+\alpha_{\mathrm{s}})}{(1+\alpha_{\mathrm{s}}\gamma_{-})} \right]^{1/2} \frac{\Gamma(\xi_1)}{[\Gamma(\xi_2)\Gamma(\xi_3)]^{1/2}}. \tag{5.27}$$

Some of the neutral species are also lost at the reactor walls and their flux to the walls are calculated through [36, 37]

$$\Gamma = \frac{\gamma}{2(2-\gamma)} n_{\mathrm{s}} v_{\mathrm{th}} = \frac{\gamma}{2(2-\gamma)} h_{\mathrm{n}} n_0 v_{\mathrm{th}}. \tag{5.28}$$

where γ represents the wall deactivation (or quenching) coefficient or the wall recombination coefficient, n_{s} is the density of the neutral species at the sheath-edge, h_{n} is the h factor for neutrals which represents the ratio between the density of the neutral species at sheath-edge and the density at the centre of the reactor, n_0 is the density of the neutral species at the centre of the reactor, and v_{th} is the mean thermal velocity of the neutral species which is calculated as in equation 5.22 with the positive ion temperature replaced by the neutral temperature and the mass of the ion replaced by the mass of the neutral

species. The edge-to-centre density ratio for neutrals h_{n} is given by [36, 37]

$$h_{\mathrm{n}} = \left[1 + \frac{L v_{\mathrm{th}} \gamma}{8 D_{\mathrm{n}} (2 - \gamma)}\right]^{-1}, \tag{5.29}$$

where D_{n} is the neutral diffusion coefficient which is calculated through [59]

$$D_{\mathrm{n}} = \frac{e T_{\mathrm{g}} \lambda_{\mathrm{n}}}{m_{\mathrm{n}} v_{\mathrm{th}}}, \tag{5.30}$$

where λ_{n} is the neutral mean free path in the gas.

6 Modelling of an Oxygen Discharge

6.1 EEDF, collisional energy loss per electron-ion pair created, and effective electron temperature

The various applications of oxygen discharges utilize different plasma sources with different coupling resulting in different EEDFs. Electrons promote many of the reactions within the discharge, therefore a knowledge of the EEDF is essential to achieve better understanding and optimization for the plasma applications. Differences in the surface material and in the ratio between the surface and volume of the reactor also change the neutral and ionic composition of the plasma, which in turn also influence the EEDF. In fact, Singh and Graves [130] stress the importance of reporting the neutral and ionic composition of the plasma along with the EEDF.

In order to evaluate the differences between the EEDFs, it is usual to use the electron energy probability function (EEPF) that relates with the EEDF through

$$F(\varepsilon) = \varepsilon^{-1/2} f(\varepsilon), \tag{6.1}$$

where $F(\varepsilon)$ is the EEPF and $f(\varepsilon)$ is the EEDF. For a Maxwellian EEDF, the EEPF appears as a straight line as the y-axis is in the logarithmic scale; therefore, EEPFs that deviate from Maxwellian are easily identified. Figure 6.1 shows the EEPF for $T_{\text{eff}} = 2$ eV for $x = 0.5$, $x = 1.0$ (Maxwellian EEDF), and $x = 2.0$ (Druyvesteyn EEDF). For $x = 0.5$, the EEPF has a concave shape which resembles a bi-Maxwellian EEPF. Bi-Maxwellian EEPFs are commonly interpreted as the sum of two Maxwellian EEPFs where one distribution represents a cold electron group and the other distribution represents a hot electron group. This concave EEPF has a higher concentration of high-energy electrons in comparison with Maxwellian EEPF and Druyvesteyn EEPF. In fact, the appearance of such a distribution is more common for low-pressure and low-density capacitively coupled discharges which provide greater energy gain by the electrons due to sheath oscillation heating. As said before, the Druyvesteyn EEPF is characterized by a reduction in the number of high energy electrons and it is usually observed at high-pressure and in high-density

inductively coupled discharges. As the T_{eff} increases, the EEPFs tend to encompass more energetic electrons for all x values.

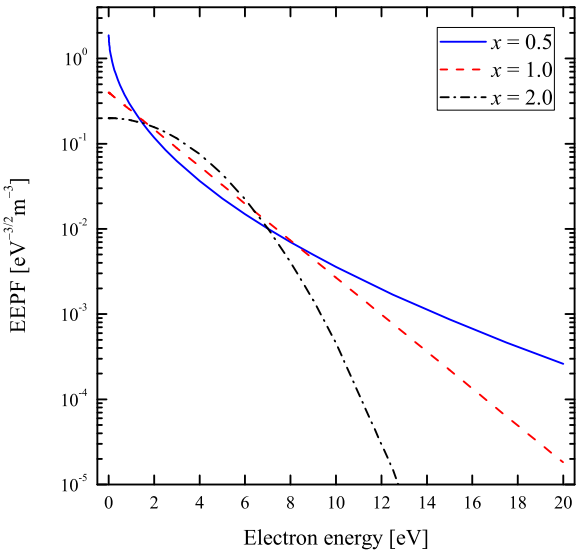

FIGURE 6.1 – The EEPF as a function of electron energy for $T_{\text{eff}} = 2$ eV, for $x = 0.5$, $x = 1.0$ (Maxwellian EEDF), and $x = 2.0$ (Druyvesteyn EEDF).

Although one can find differences in results of Langmuir probe measurements in an inductively coupled oxygen discharge, a general behaviour has been reported for the electron energy probability function (EEPF). The EEPF that can be approximated to a Maxwellian distribution at low pressures becomes depleted of high energy electrons as pressures increases taking the shape of a two temperature distribution [39, 40, 42, 46, 131–133], which approximates to a Druyvesteyn distribution. Countering these results, Fuller *et al* [41] reported a bi-Maxwellian EEPF with a low temperature electron group for electron energies below 15 eV and a high temperature electron group for electron energies above 15 eV for 10 mTorr and 980 W. In addition Singh and Graves [130] reported that the EEPF develops a three temperature structure at high pressures – apparently for pressures above 30 mTorr.

Changes in the EEDF change the rate coefficientes that are calculated by equation 5.2 affecting the collisional energy loss per electron-ion pair created. Figure 6.2 shows the collisional energy loss per electron-ion pair created for $O_2(X^3\Sigma_g^-)$ and $O(^3P)$ as a function of the electron temperature for different EEDFs. The collisional energy loss per electron-ion pair created is calculated through equation 5.17 using reactions from 6 to 22 for $O_2(X^3\Sigma_g^-)$ and reactions from 46 to 53 for $O(^3P)$. Reactions 12, 13, 14, 15, and 16 are used just to calculate the collisional energy loss per electron-ion pair created for $O_2(X^3\Sigma_g^-)$. The same applies for reactions 49, 50, 51, 52, and 53 which are only used to calculate the collisional energy loss per electron-ion pair created for $O(^3P)$. There are no particle balance equations for the rotational and vibrational excited states; O_2(rot),

O_2(v1), O_2(v2), O_2(v3), and O_2(v4); for the non-Rydberg states; O(^{1}S) and O(^{3}P^o); and for the Rydberg states; O(^{5}S^o) and O(^{3}S^o).

The collisional energy loss per electron-ion pair created is higher for $O_2(X^3\Sigma_g^-)$ as compared with O(^{3}P) because electrons lose more energy when they collide with molecules as molecules have vibrational and rotational excited states. Note that the collisional energy loss per electron-ion pair created increases significantly as the parameter x is increased for $T_{eff} < 10$ eV. EEDFs which include higher population of high energy electrons result in higher rate coefficients for electron-impact ionization which result in lower values for collisional energy loss per electron-ion pair created. Planar inductively coupled discharges typically operate at effective electron temperature in the range from 2 to 6 eV [40]; therefore, the EEDF has considerable influence on the plasma parameters since the collisional energy loss per electron-ion pair created changes significantly in this range.

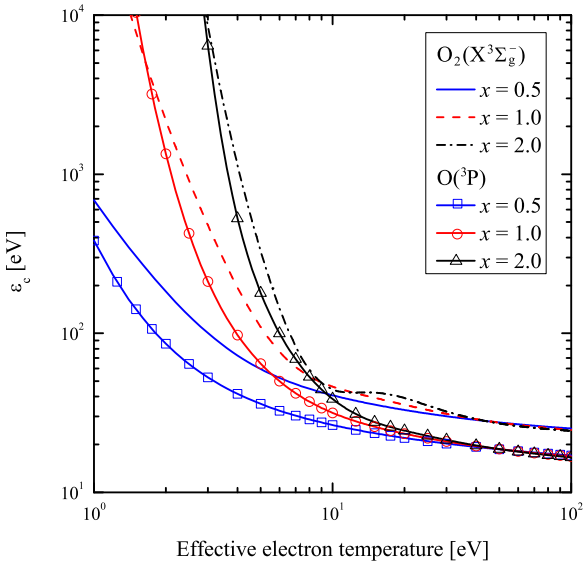

FIGURE 6.2 – Collisional energy loss per electron-ion pair created for $O_2(X^3\Sigma_g^-)$ and O(^{3}P) as a function of effective electron temperature for $x = 0.5$, $x = 1.0$ (Maxwellian EEDF), and $x = 2.0$ (Druyvesteyn EEDF).

Note that the collisional energy loss per electron-ion pair created for O(^{3}P) is higher than the collisional energy loss per electron-ion pair created for $O_2(X^3\Sigma_g^-)$ for electron temperatures below 1.6 eV for $x = 1.0$. In fact, the difference between the collisional energy loss per electron-ion pair created for O(^{3}P) and the collisional energy loss per electron-ion pair created for $O_2(X^3\Sigma_g^-)$ decreases as the electron temperature (or effective electron temperature for $x = 0.5$ and $x = 2.0$) decreases. The reason is the decrease of the rate coefficients for ionization of O(^{3}P) and $O_2(X^3\Sigma_g^-)$ as electron temperature decreases. The decrease of the rate coefficient for O(^{3}P) ionization is steeper than the decrease of the rate coefficient for $O_2(X^3\Sigma_g^-)$ ionization resulting in a collisional energy loss per electron-ion pair created that is higher for O(^{3}P) than for $O_2(X^3\Sigma_g^-)$ at low electron

temperatures.

The following results depend on input parameters, power and pressure, reactor dimensions, and reactor wall properties. We assume a cylindrical reactor chamber with radius $R = 15$ cm and length $L = 30$ cm. The flow rate of oxygen feedstock is 50 sccm, the gas temperature is assumed 600 K, and the power absorbed by the plasma is 500 W.

Figure 6.3 shows the effective electron temperature as a function of pressure for different EEDFs for stainless steel and anodized aluminium reactor walls. At low pressures, the energy supplied to the plasma is shared among a lower quantity of species, therefore the effective electron temperature is higher. At high pressures, the quantity of species in the plasma are high, therefore the electron temperature decreases. As x increases, the effective electron temperature increases which is explained by the decrease of the electron density that will be discuss in the figure 6.14. The effective electron temperature relates with the mean electron density through equation 5.10. The effective electron temperature for anodized aluminium reactor is higher than the effective electron temperature for stainless steel reactor for low pressures; however, this difference is small. This is due to the increased partial pressure of oxygen atoms which have higher ionization potential than oxygen molecules. At higher pressures, the difference in the effective electron temperature is negligible.

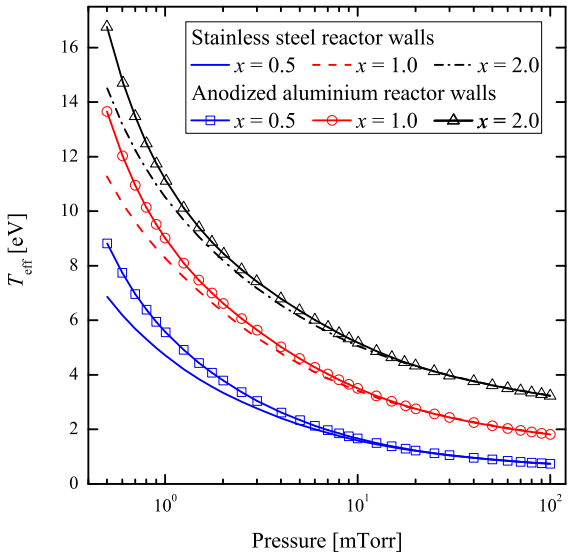

FIGURE 6.3 – The effective electron temperature as a function of pressure for $x = 0.5$, $x = 1.0$ (Maxwellian EEDF), and $x = 2.0$ (Druyvesteyn EEDF) for cylindrical stainless steel chamber and cylindrical anodized aluminium chamber of radius $R = 15$ cm and length $L = 30$ cm, and absorbed power of 500 W.

6.2 Neutral species

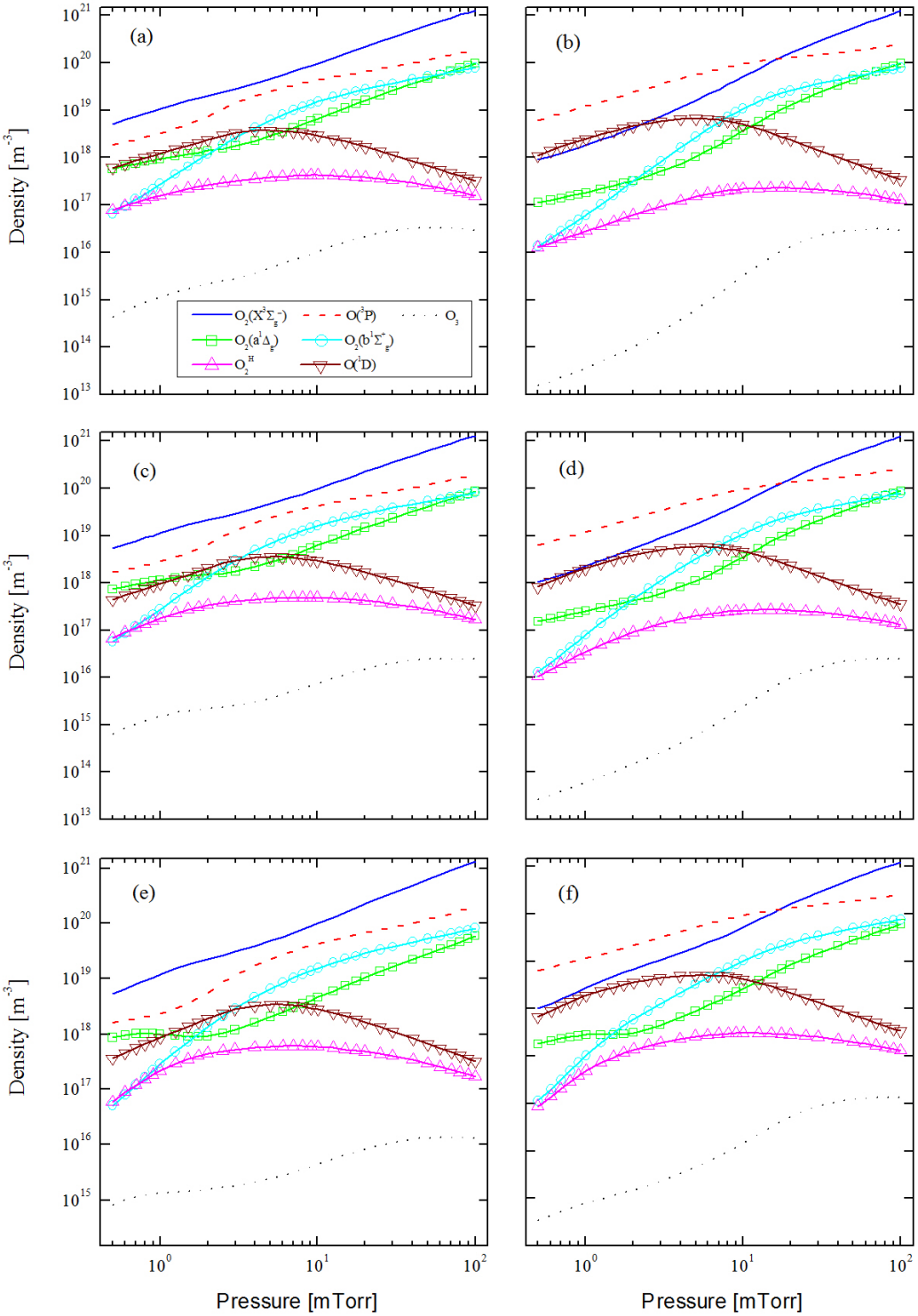

FIGURE 6.4 – Mean density of neutral species as a function of pressure for (a) stainless steel reactor walls and $x = 0.5$, (b) anodized aluminium reactor walls and $x = 0.5$, (c) stainless steel reactor walls and $x = 1.0$, (d) anodized aluminium reactor walls and $x = 1.0$, (e) stainless steel reactor walls and $x = 2.0$, (f) anodized aluminium reactor walls and $x = 2.0$.

It was mentioned that the partial pressure of $O(^3P)$ increases at low pressures, thus it is appropriate to discuss the density of neutral species. The mean density of neutral species as a function of pressure is shown in figure 6.4 (a) for a stainless steel reactor walls and $x = 0.5$, in figure 6.4 (b) for an anodized aluminium reactor walls and $x = 0.5$, in figure 6.4 (c) for a stainless steel reactor walls and $x = 1.0$, in figure 6.4 (d) for an anodized aluminium reactor walls and $x = 1.0$, in figure 6.4 (e) for a stainless steel reactor walls and $x = 2.0$, and in figure 6.4 (f) for an anodized aluminium reactor walls and $x = 2.0$.

See that changes in the EEDF results in minor changes in the mean density of neutrals thus the following discussion is valid for the three values of x. For stainless steel reactor walls, the dominant species is the oxygen molecule in the ground state $O_2(X^3\Sigma_g^-)$ followed by the oxygen atom in the ground state $O(^3P)$. The singlet metastable states of the oxygen molecule $O_2(a^1\Delta_g)$ and $O_2(b^1\Sigma_g^+)$ and the singlet metastable state of the oxygen atom $O(^1D)$ are present in the plasma in significant amounts. For anodized aluminium reactor walls, the dominant species is $O(^3P)$ for low pressures (< 17 mTorr). As pressure increases, the dominant species is $O_2(X^3\Sigma_g^-)$. The density of $O(^1D)$ is comparable to the density of $O_2(X^3\Sigma_g^-)$ for low pressure. For $x = 0.5$, the density of $O(^1D)$ overcomes the density of $O_2(X^3\Sigma_g^-)$.

For both stainless steel or anodized aluminium reactors, the density of the Herzberg states $O_2(A^3\Sigma_u^+, A'^3\Delta_u, c^1\Sigma_u^-)$ is low and the density of ozone O_3 is even lower. Thus, neglecting these species in the reaction set in more computationally intensive models such as fluid models and particle-in-cell Monte Carlo collision simulations may be justified.

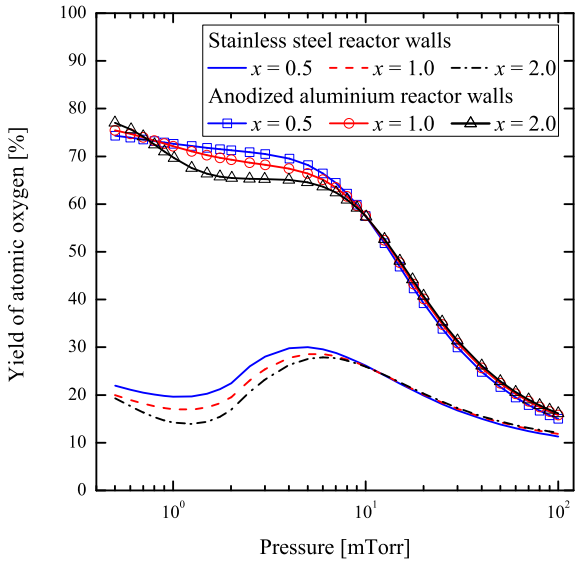

FIGURE 6.5 – The yield of atomic oxygen as a function of pressure for $x = 0.5$, $x = 1.0$ (Maxwellian EEDF), and $x = 2.0$ (Druyvesteyn EEDF) for cylindrical stainless steel chamber and anodized aluminium chamber of radius $R = 15$ cm and length $L = 30$ cm, and absorbed power of 500 W.

A further study can be done to understand better the increase of the desinty of oxygen atom showed in the figure 6.4 for anodized aluminium reactors at low pressures. Figure 6.5 shows the yield of atomic oxygen as a function of pressure for $x = 0.5$, $x = 1.0$, and $x = 2.0$ for stainless steel and anodized aluminium reactor walls. The yield of atomic oxygen is calculated by the ratio between the density of oxygen atom and the total density of the neutral species. As discussed above, changes in the EEDF results in minor changes in the density of neutral species, therefore small changes are noted for low pressures for different values of x. However, there is a huge difference in the yield of oxygen atom due to the different wall materials studied. The reason is the low recombination coefficient of oxygen atom at the walls for anodized aluminium as compared to stainless steel which results in high yield of oxygen atom.

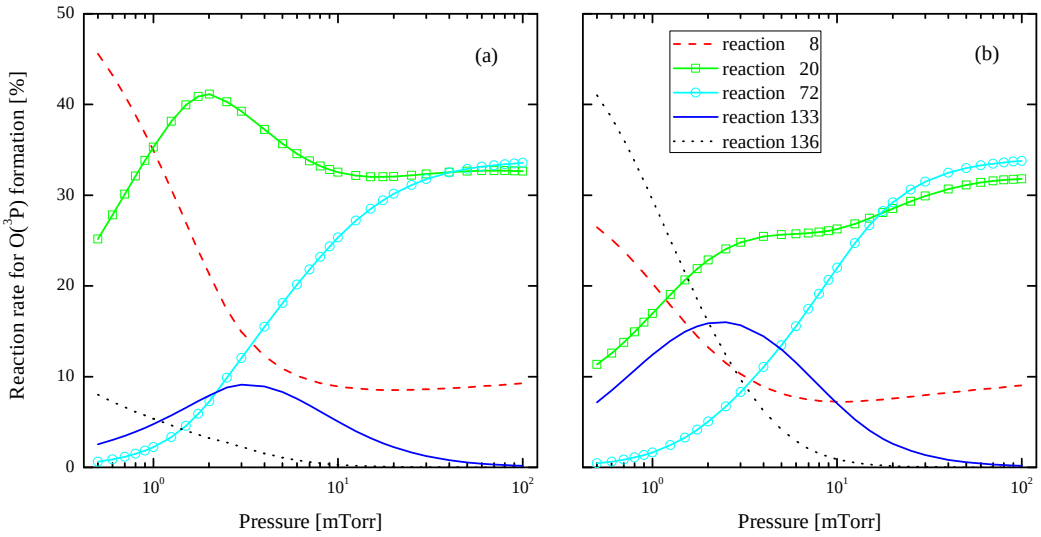

FIGURE 6.6 – Reactions rates for $O(^3P)$ formation as a function of pressure for $x = 1.0$ for (a) stainless steel reactor and (b) anodized aluminium reactor – other reactions with very small reaction rates are not shown in these figures.

Changes in the EEDF results in minor changes in the reaction rates for formation and annihilation of oxygen atom, but changes in the wall material results in significant changes. Therefore, figure 6.6 shows the reaction rates for the most important channels for formation of $O(^3P)$ as a function of pressure for a Maxwellian EEDF for (a) stainless steel reactor walls and (b) anodized aluminium reactor walls. For a stainless steel reactor, the main channels for formation of oxygen atom in the ground state $O(^3P)$ are (reaction 8)

$$e + O_2(X^3\Sigma_g^-) \longrightarrow e + O(^3P) + O(^3P)$$

and (reaction 20)

$$e + O_2(X^3\Sigma_g^-) \longrightarrow e + O(^3P) + O(^1D)$$

at low pressures. As pressure increases, the channel (reaction 72)

$$O_2(X^3\Sigma_g^-) + O(^1D) \longrightarrow O(^3P) + O_2(b^1\Sigma_g^+)$$

becomes an important contributor while the reaction rate for reaction 8 decreases. For an anodized aluminium reactor, due to the high density of O^+ for pressures below 10 mTorr (see figure 6.4), the contribution of quenching of O^+ at the walls (reaction 136) for formation of $O(^3P)$ is higher than the contributions of dissociation of $O_2(X^3\Sigma_g^-)$. Quenching of $O(^1D)$ is also a significant contributor for formation of $O(^3P)$ at low pressures.

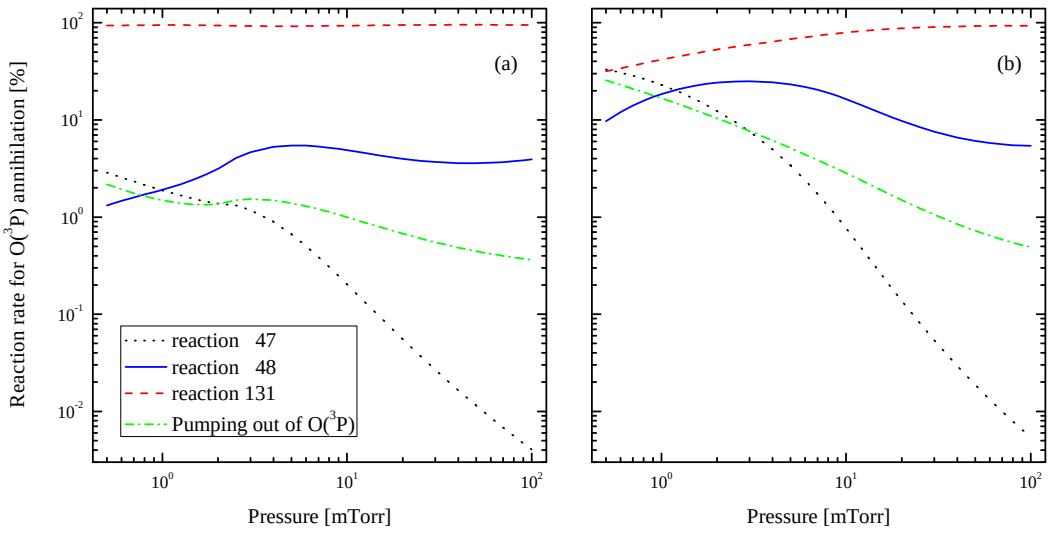

FIGURE 6.7 – Reactions rates for $O(^3P)$ annihilation as a function of pressure for $x = 1.0$ for (a) stainless steel reactor and (b) anodized aluminium reactor – other reactions with very small reaction rates are not shown in these figures.

Figure 6.7 shows the reaction rates for $O(^3P)$ annihilation as a function of pressures for $x = 1.0$ for (a) stainless steel walls and (b) anodized aluminium walls. For stainless steel walls, the dominant channel for annihilation of $O(^3P)$ is recombination at the walls producing $O_2(X^3\Sigma_g^-)$ (reaction 131) through all range of pressure studied. The low recombination coefficient assumed for anodized aluminium reactor walls results in a significant decrease of the contribution of recombination at the walls for annihilation of $O(^3P)$ at low pressures. Electron impact ionization (reaction 47),

$$e + O(^3P) \longrightarrow 2e + O^+,$$

and electron impact excitation to the metastable state $O(^1D)$ (reaction 48),

$$e + O(^3P) \longrightarrow e + O(^1D),$$

along with pumping out become important contributors for annihilation of $O(^3P)$. As

pressure increases, recombination of $O(^3P)$ at the walls becomes the main channel for $O(^3P)$ loss in anodized aluminium reactors as in stainless steel reactors. The loss of neutral species is calculated in the model through equation 5.28, therefore the flux of $O(^3P)$ to the walls increases even though the recombination coefficient is low due to the increase of the density of $O(^3P)$.

Fuller *et al.* [41] studied the densities of $O_2(X^3\Sigma_g^-)$, $O(^3P)$, $O(^1D)$, and $O(^1S)$ as a function of power in an inductive oxygen discharge emphasizing the importance of atomic oxygen density to etching of low-k organic films. Their measured dissociation fraction is roughly 1 % at 400 W and 10 mTorr somewhat lower than our calculations. Corr *et al.* [42] also studied the atomic oxygen density as a function of power and pressure in an inductive oxygen discharge. Their results show that the atomic oxygen density decreases as pressure increases in the pressure range 12.5 – 50 mTorr and the dissociation fraction is in the range 10 – 20 % at 25 mTorr and 170 – 270 W. They also see enhancement in dissociation with decreasing pressure, it is 10 % at 50 mTorr and increases up to 50 % at 12.5 mTorr.

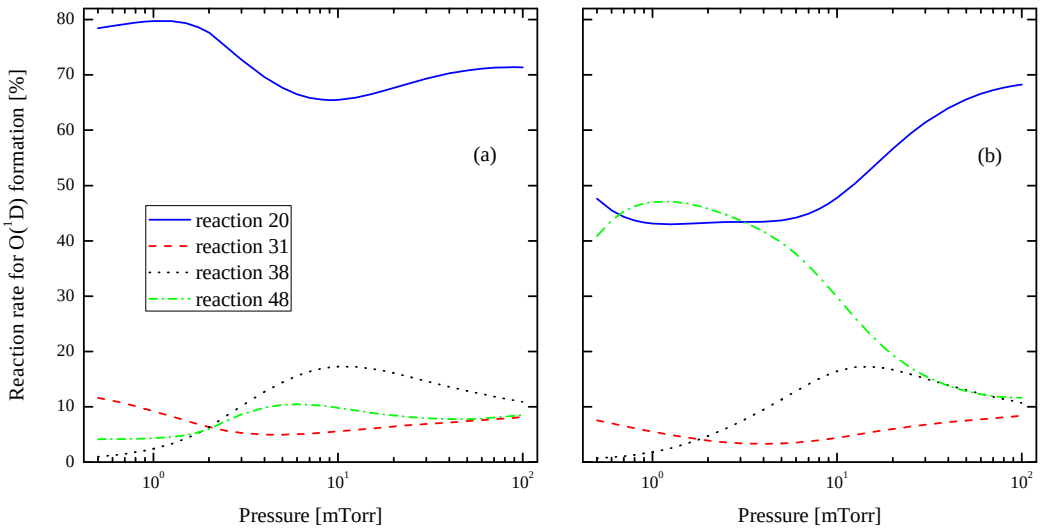

FIGURE 6.8 – Reactions rates for $O(^1D)$ formation as a function of pressure for $x = 1.0$ for (a) stainless steel reactor and (b) anodized aluminium reactor – other reactions with very small reaction rates are not shown in these figures.

Figure 6.8 shows the reaction rates for $O(^1D)$ formation as a function of pressure for $x = 1.0$ for (a) stainless steel walls and (b) anodized aluminium walls. Formation of $O(^1D)$ occurs mostly through reaction 20 for both of the wall materials studied. However, due to the increase of $O(^3P)$ at low pressures, a significant amount of $O(^1D)$ is produced through reaction 48.

Figure 6.9 shows the reaction rates for $O(^1D)$ annihilation as a function of pressure for $x = 1.0$ for (a) stainless steel walls and (b) anodized aluminium walls. For stainless steel

reactors, the main channel for $O(^1D)$ annihilation is recombination at the walls (reaction 132) at low pressures and reaction 72 at high pressures. For anodized aluminium reactors, the low recombination coefficient results in a decrease of the reaction rate of reaction 132 and an increase in the reaction rates of the reactions 55, 56, 92, and 133 and in the rate of pumping $O(^1D)$ out for low pressure. As pressure increases, the reaction rates of the reactions 55, 56, 92, and 133 and the rate of pump $O(^1D)$ out decrease and the reaction rate of the reaction 72 increases. Therefore, the reason of the increase of the density of $O(^1D)$ at low pressures in anodized aluminium reactors showed in figure 6.4 due to the increase of the density of $O(^3P)$ that contributed to formation of $O(^1D)$ through reaction 48 and the low recombination coefficient that was assumed for reaction 132 that reduces the recombination of $O(^1D)$ at the walls.

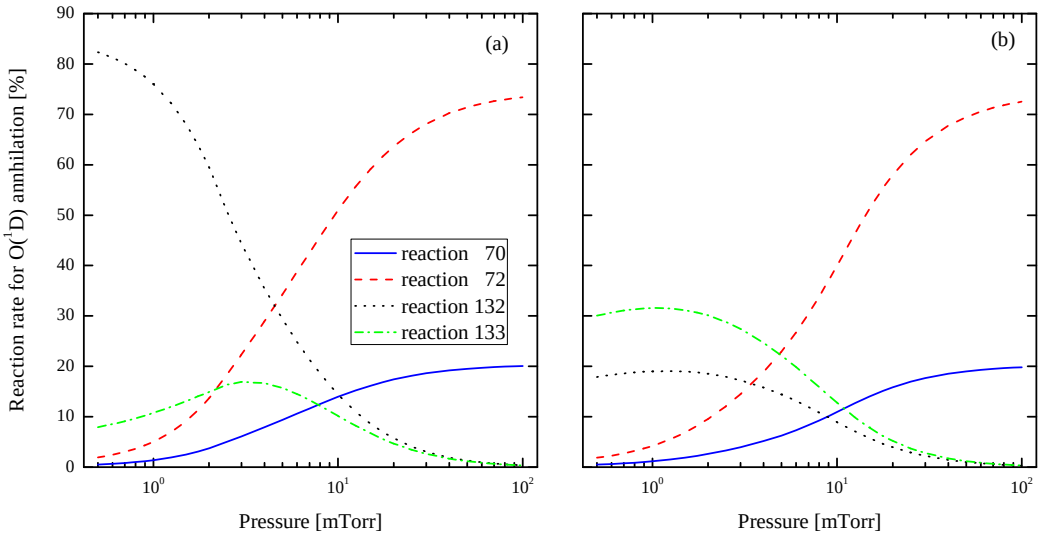

FIGURE 6.9 – Reactions rates for $O(^1D)$ annihilation as a function of pressure for $x = 1.0$ for (a) stainless steel reactor and (b) anodized aluminium reactor – other reactions with very small reaction rates are not shown in these figures.

Other point that draws attention in the figure 6.4 involve the $O_2(b^1\Sigma_g^+)$ density. In general, the $O_2(a^1\Delta_g)$ density is reported to be higher than the $O_2(b^1\Sigma_g^+)$ density [44]; however, the calculations with this more extended reaction set show that the $O_2(b^1\Sigma_g^+)$ density can overcome the $O_2(a^1\Delta_g)$ density.

The differences in the reaction rates for formation and annihilation of $O_2(a^1\Delta_g)$ and $O_2(b^1\Sigma_g^+)$ due to changes in the EEDF and in the material of the reactor walls ar smal for the EEDFs and materials analyzed in this work. Thus, the main channels for formation and annihilation of these species for $x = 1.0$ in a stainless steel reactor are also the main channels for $x = 0.5$ and $x = 2.0$ in stainless steel and for for $x = 0.5$, $x = 1.0$, and $x = 2.0$ in anodized aluminium reactor.

Figure 6.10 shows the main reaction rates for $O_2(a^1\Delta_g)$ formation for $x = 1.0$ in a

stainless steel reactor. Formation of $O_2(a^1\Delta_g)$ is dominated by electron impact excitation (reaction 17),

$$e + O_2(X^3\Sigma_g^-) \longrightarrow O_2(a^1\Delta_g) + e.$$

Energy transfer from $O(^1D)$ to $O_2(X^3\Sigma_g^-)$ creating $O_2(a^1\Delta_g)$ (reaction 71),

$$O(^1D) + O_2(X^3\Sigma_g^-) \longrightarrow O_2(a^1\Delta_g) + O(^3P),$$

and quenching of the metastable oxygen molecule $O_2(b^1\Sigma_g^+)$ (reaction 87),

$$O(^3P) + O_2(b^1\Sigma_g^+) \longrightarrow O_2(a^1\Delta_g) + O(^3P),$$

are also significant processes for $O_2(a^1\Delta_g)$ formation. Other reactions have negligible contributions for formation of $O_2(a^1\Delta_g)$ [52].

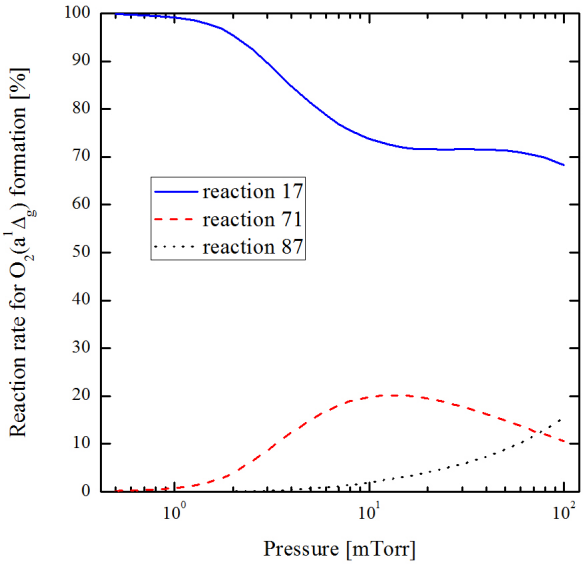

FIGURE 6.10 – Reactions rates for $O_2(a^1\Delta_g)$ formation as a function of pressure for $x = 1.0$ in a stainless steel reactor – other reactions with very small reaction rates are not shown in this figure.

Figure 6.11 shows the main reaction rates for $O_2(a^1\Delta_g)$ annihilation for $x = 1.0$ in a stainless steel reactor. Electron impact dissociations, (reaction 31)

$$e + O_2(a^1\Delta_g) \longrightarrow O(^3P) + O(^1D) + e$$

and (reaction 24)

$$e + O_2(a^1\Delta_g) \longrightarrow O(^3P) + O(^3P) + e,$$

are important contributors to the loss of $O_2(a^1\Delta_g)$. Electron impact de-excitation (reaction 26),

$$e + O_2(a^1\Delta_g) \longrightarrow O_2(X^3\Sigma_g^-) + e,$$

is also important and electron impact ionization from the metastable oxygen molecule $O_2(a^1\Delta_g)$ (reaction 23),

$$e + O_2(a^1\Delta_g) \longrightarrow O_2^+ + 2e,$$

is important at low pressures. Other reactions have negligible influence on $O_2(a^1\Delta_g)$ annihilation [52]. The wall quenching (reaction 128) is low at low pressures, but it becomes important as pressure increases. It overcomes the reaction rate of reaction 31 for $O_2(a^1\Delta_g)$ annihilation at 80 mTorr in figure 6.11. The rate for pumping of $O_2(a^1\Delta_g)$ out of the reactor is low.

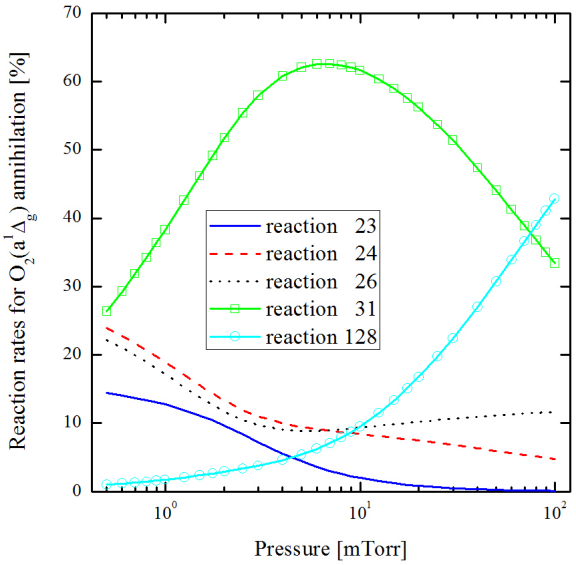

FIGURE 6.11 – Reactions rates for $O_2(a^1\Delta_g)$ annihilation as a function of pressure for $x = 1.0$ in a stainless steel reactor – other reactions with very small reaction rates are not shown in this figure.

Figure 6.12 shows the main reaction rates for $O_2(b^1\Sigma_g^+)$ formation for $x = 1.0$ in a stainless steel reactor. The most important contributor to the formation of the metastable oxygen molecule $O_2(b^1\Sigma_g^+)$ is reaction 72. Therefore, this reaction is very important for oxygen plasma modelling since it is an important contributor for formation of $O(^3P)$ and $O_2(b^1\Sigma_g^+)$ and for annihilation of $O(^1D)$. The reaction rate for this reaction is taken from the review of Baulch *et al.* [35] which is based on the measurements of Streit *et al.* [134] and Amimoto *et al.* [135]. This reaction has been suggested to be a major contributor to the formation of $b^1\Sigma_g^+$ state in the atmosphere [136]. Electron impact excitation from the ground state (reaction 18),

$$e + O_2(X^3\Sigma_g^-) \longrightarrow O_2(b^1\Sigma_g^+) + e,$$

also gives a significant contribution to formation of $O_2(b^1\Sigma_g^+)$ at low pressures. Other reactions have negligible contribution for $O_2(b^1\Sigma_g^+)$ formation [52].

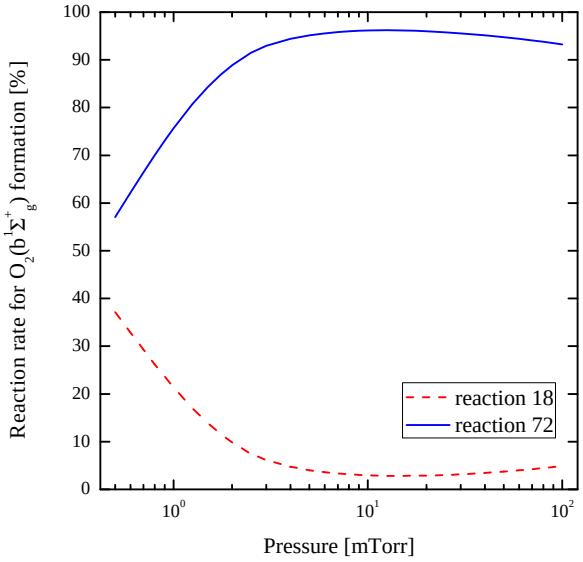

FIGURE 6.12 – Reactions rates for $O_2(b^1\Sigma_g^+)$ formation as a function of pressure for $x = 1.0$ in a stainless steel reactor – other reactions with very small reaction rates are not shown in this figure.

Figure 6.13 shows the main reaction rates for $O_2(b^1\Sigma_g^+)$ annihilation for $x = 1.0$ in a stainless steel reactor. Electron impact ionization (reaction 33),

$$e + O_2(b^1\Sigma_g^+) \longrightarrow O_2^+ + 2e,$$

electron impact dissociation from the metastable oxygen molecule $O_2(b^1\Sigma_g^+)$ with no formation of $O(^1D)$ (reaction 34),

$$e + O_2(b^1\Sigma_g^+) \longrightarrow O(^3P) + O(^3P) + e,$$

and with formation of $O(^1D)$ (reaction 38),

$$e + O_2(b^1\Sigma_g^+) \longrightarrow O(^3P) + O(^1D) + e,$$

and quenching of $O_2(b^1\Sigma_g^+)$ at the walls (reaction 129) have important contributions for $O_2(b^1\Sigma_g^+)$ loss. Other reactions have negligible contribution for $O_2(b^1\Sigma_g^+)$ annihilation [52].

6.3 Charged species

The mean density of charged species as a function of pressure is shown in figure 6.14 (a) for a stainless steel reactor walls and $x = 0.5$, in figure 6.14 (b) for an anodized aluminium reactor walls and $x = 0.5$, in figure 6.14 (c) for a stainless steel reactor walls

and $x = 1.0$, in figure 6.14 (d) for an anodized aluminium reactor walls and $x = 1.0$, in figure 6.14 (e) for a stainless steel reactor walls and $x = 2.0$, and in figure 6.14 (f) for an anodized aluminium reactor walls and $x = 2.0$. Different from neutrals, the density of charged species have significant changes due to changes in the EEDF.

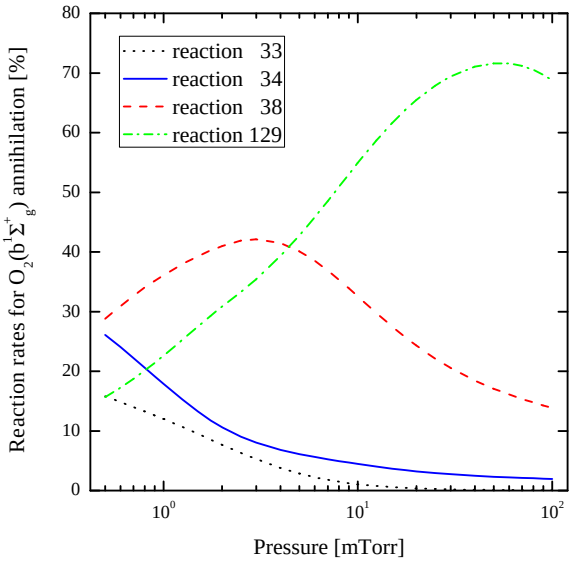

FIGURE 6.13 – Reactions rates for $O_2(b^1\Sigma_g^+)$ annihilation as a function of pressure for $x = 1.0$ in a stainless steel reactor – other reactions with very small reaction rates are not shown in this figure.

The density of electrons decreases as x increases. The increase of the effective electron temperature (see figure 6.3) and the decrease of the mean electron density as x increases were also found for Ar [47], N_2 [48], and Cl_2 [49, 50] discharges. There is an increase in the electron density with increased pressure to a peak value, then the electron density decreases as pressure increases further. This behavior of the mean electron density can be seen for the three values of x for stainless steel and anodized aluminium reactor walls.

Similar variation of the mean electron density with pressure was reported by Kim *et al.* [36,37]. They reported an initial increase in the electron density for absorbed power of 1000 W and 2000 W. Global model calculations for Cl_2 discharge [49] also show a similar decrease in the electron density as pressure increases. The center electron density in an inductively coupled oxygen discharge at 500 W has been measured to be $3 - 6 \times 10^{16}$ m^{-3} and increase with increased pressure in the pressure range 3 – 45 mTorr [38].

As the mean electron density is calculated through the charge neutrality requirement, its behaviour is related to the densities of the other charged species. Although the dominant negative charged species is always the electron, the difference between the desinties of electrons, O^-, and O_2^- decrease as x or pressure increases. At 100 mTorr, for $x = 2.0$, the densities of electrons, O^-, and O_2^- are close for both stainless steel and anodized aluminium reactors.

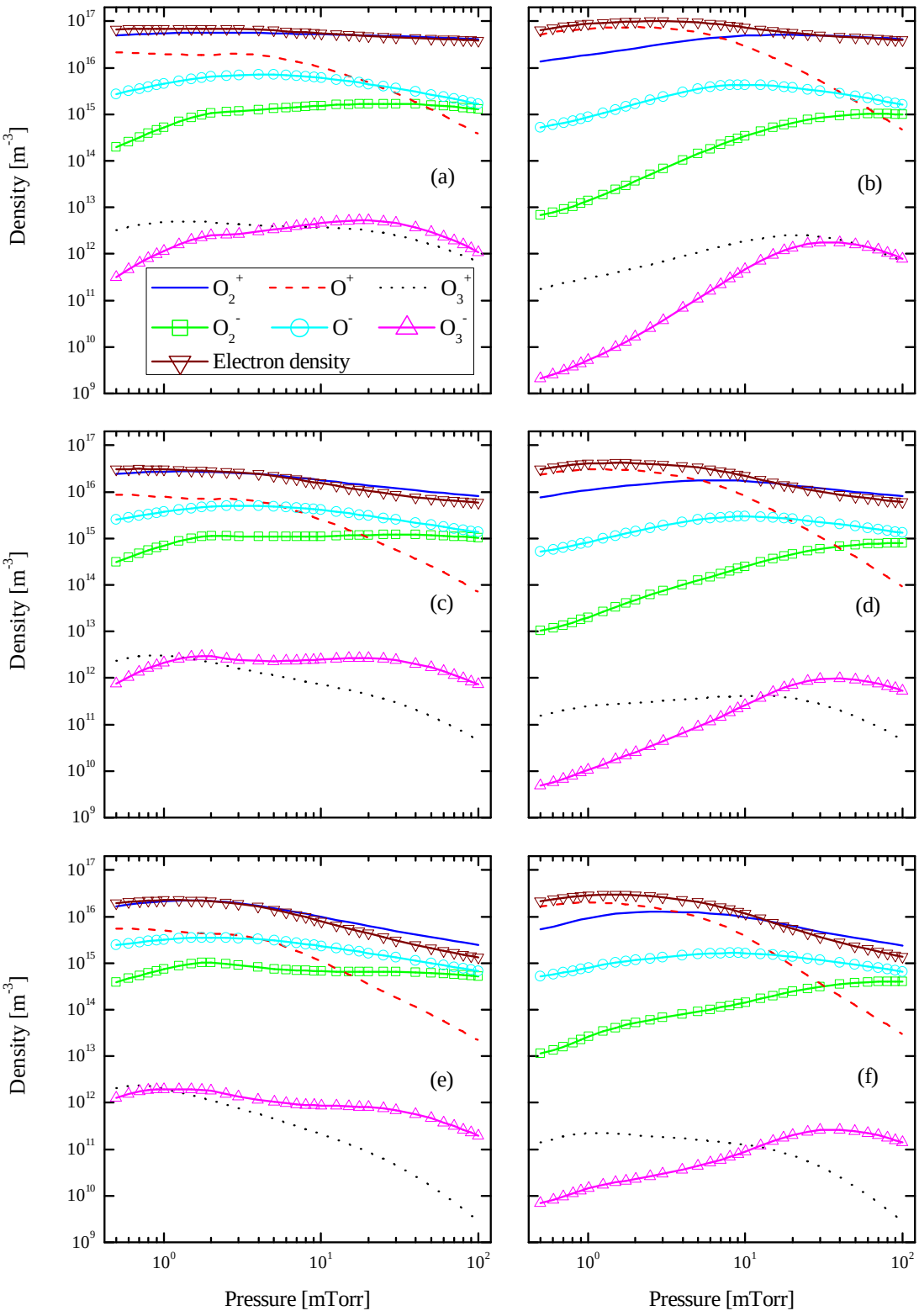

FIGURE 6.14 – Mean density of charged species as a function of pressure for (a) stainless steel reactor walls and $x = 0.5$, (b) anodized aluminium reactor walls and $x = 0.5$, (c) stainless steel reactor walls and $x = 1.0$, (d) anodized aluminium reactor walls and $x = 1.0$, (e) stainless steel reactor walls and $x = 2.0$, (f) anodized aluminium reactor walls and $x = 2.0$.

For stainless steel reactor walls, the dominant positive charged species is O_2^+ for the three x values. However, the density of O^+ is significant for low pressures. For anodized aluminium reactor walls, the oxygen atom ion O^+ is the dominant species for low pressures. As pressure decreases, the density of O^+ has a deep decrease and the density of O_2^+ increases therefore O_2^+ becomes the dominant positive charged species at high pressures in anodized aluminium reactors. The densities of ozone ions O_3^+ and O_3^- are very low when compared to the other ions due to the low amount of ozone in the plasma. Therefore, neglect these ions is also justified in oxygen discharge modelling.

For $x = 1.0$, the fractions of O^+ ions, defined as $[O^+]/([O^+]+[O_2^+])$, are 0.21 at 3 mTorr, 0.16 at 7 mTorr, and 0.07 at 20 mTorr. These results agree with mass spectrometer measurements reported in [40]. Mesurements show that O^- is the dominant negative ion and its density is always higher than the O_2^- density and the molecular ion corresponds to 10 – 20 % of the total density [137]. However, it should be kept in mind that these measurements were made in a capacitively coupled discharge that is operated at significantly lower power than what is assumed in our calculations. More recently Corr *et al* [42] measured the negative ion density in an inductively coupled discharge in the inductive mode. They found the negative ion density to initially increase with pressure to peak at 2×10^{16} m^3 for 275 W absorbed at roughly 20 mTorr and then fall again to about 2×10^{15} m^3 at 40 mTorr for a $R = 8.25$ cm and $L = 20.25$ cm. They found the negative ion density to increase with increased absorbed power.

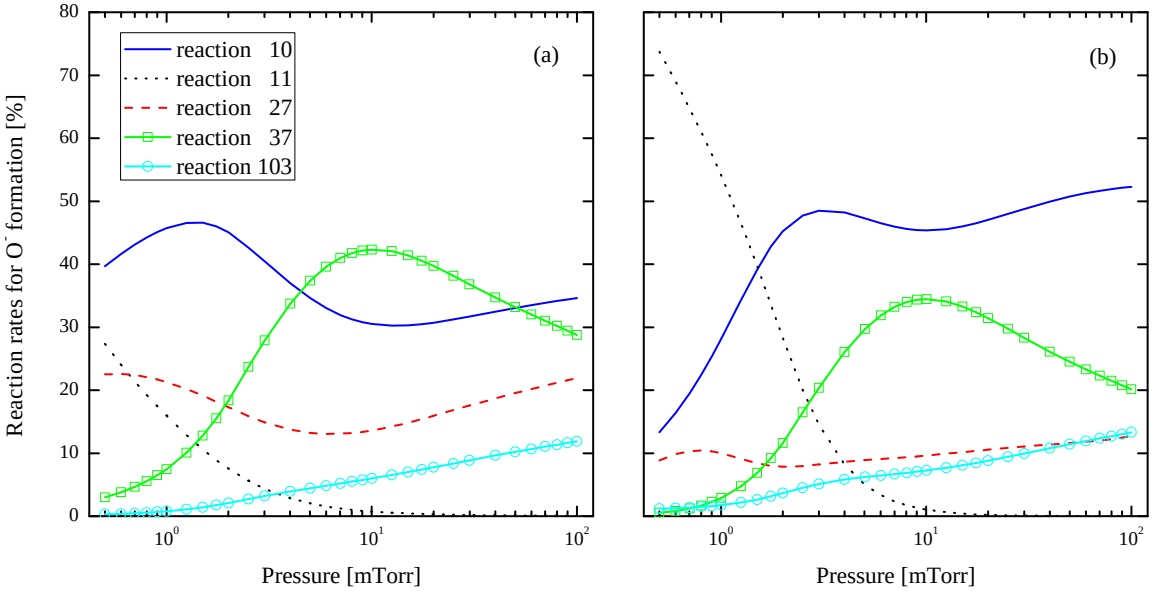

FIGURE 6.15 – Reactions rates for O^- formation as a function of pressure for stainless steel reactor walls for (a) $x = 0.5$ and (b) $x = 2.0$ – other reactions with very small reaction rates are not shown in this figure.

The main channels for formation of O^- are dissociative attachment (reaction 10),

$$e + O_2(X^3\Sigma_g^-) \longrightarrow O(^3P) + O^-,$$

electron impact polar dissociation (reaction 11),

$$e + O_2(X^3\Sigma_g^-) \longrightarrow e + O^+ + O^-,$$

dissociative attachment from the $a^1\Delta_g$ state (reaction 27),

$$e + O_2(a^1\Delta_g) \longrightarrow O(^3P) + O^-,$$

dissociative attachment from the $b^1\Sigma_g^+$ state (reaction 37),

$$e + O_2(b^1\Sigma_g^+) \longrightarrow O(^3P) + O^-,$$

and charge exchange between O_2^- and $O(^3P)$ (reaction 103),

$$O_2^- + O(^3P) \longrightarrow O_2(X^3\Sigma_g^-) + O^-.$$

It was stated in [53] that these channels are the main channels for formation of O^- for approximately all x values in a stainless steel and anodized aluminum reactors. However, there are differences that need to be discussed. In fact, there are no difference in the reaction rates due to the two different wall materials studied, but there are differences due to changes in the EEDF. Figure 6.15 shows the reaction rates for O^- formation as a function of pressure for stainless steel reactor walls for (a) $x = 0.5$ and (b) $x = 2.0$. At, the reaction rates of reactions 10 and 27 decrease while the reaction rate of reaction 11 increases as x increases. As x increases, the effective electron temperature increases (see figure 6.3) resulting in higher mean electron energy according to equation 5.6 that favor reaction with a higher threshold energy like reaction 11.

As the loss process of O^- has been a polemic issue [40, 42, 44, 138–142], first, the reaction rates for O^- annihilation will be studied for Maxwellian EEDF for stainless steel reactors. Then, the differences in the reaction rates for non-Maxwellian EEDFs and for anodized aluminium reactors will be discussed. The reaction rates for reactions 54, 113, 114, 115, 116, 117, 118, 119, and 120 are presented in figure 6.16 as a function of pressure for $x = 1.0$ and for stainless steel reactor walls. The results show that the electron impact detachment (reaction 54),

$$e + O^- \longrightarrow 2e + O(^3P),$$

is the main contributor to O^- annihilation at low pressures (< 20 mTorr) unlike of what was reported in a previous work [44].

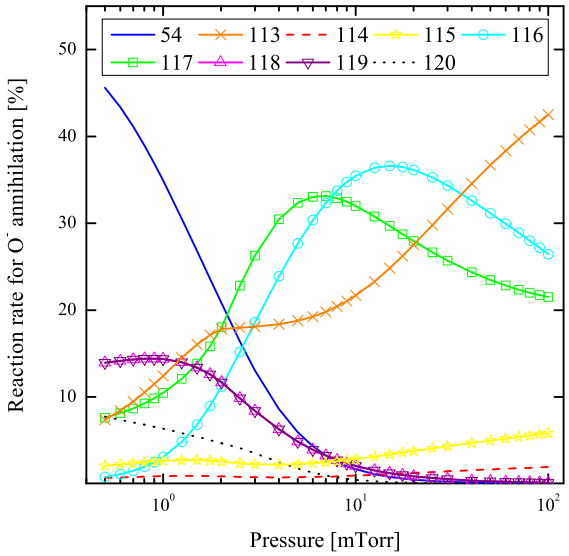

FIGURE 6.16 – Reaction rates for O^- annihilation as a function of pressure for $x = 1.0$ and for stainless steel reactor walls – other reactions with very small reaction rates are not shown in this figure.

Figure 6.17 (a) and (b) show the reaction rates for reactions that contribute to O^- annihilation reported in [44]. In these figures rec1 represents $O^- + O^+ \longrightarrow O(^3P) + O(^3P)$, rec2 represents $O^- + O_2^+ \longrightarrow O(^3P) + O_2(X^3\Sigma_g^-)$, det,e represents $e + O^- \longrightarrow 2e + O(^3P)$, det,O represents $O^- + O(^3P) \longrightarrow e + O_2(X^3\Sigma_g^-)$, det,a represents the sum of the reaction rates of $O^- + O_2(a^1\Delta_g) \longrightarrow O(^3P) + O_2^-$ and $O^- + O_2(a^1\Delta_g) \longrightarrow e + O_3$, and det,b represents $O^- + O_2(b^1\Sigma_g^+) \longrightarrow e + O(^3P) + O_2(X^3\Sigma_g^-)$. Reaction 120 in figure 6.16 is reaction rec1 in figures 6.17 (a) and (b). It was found here that reaction 120 contributes with less than 10 % for the loss of O^- while it was reported in [44] that mostly of the loss of O^- occurs through this reaction at low pressures.

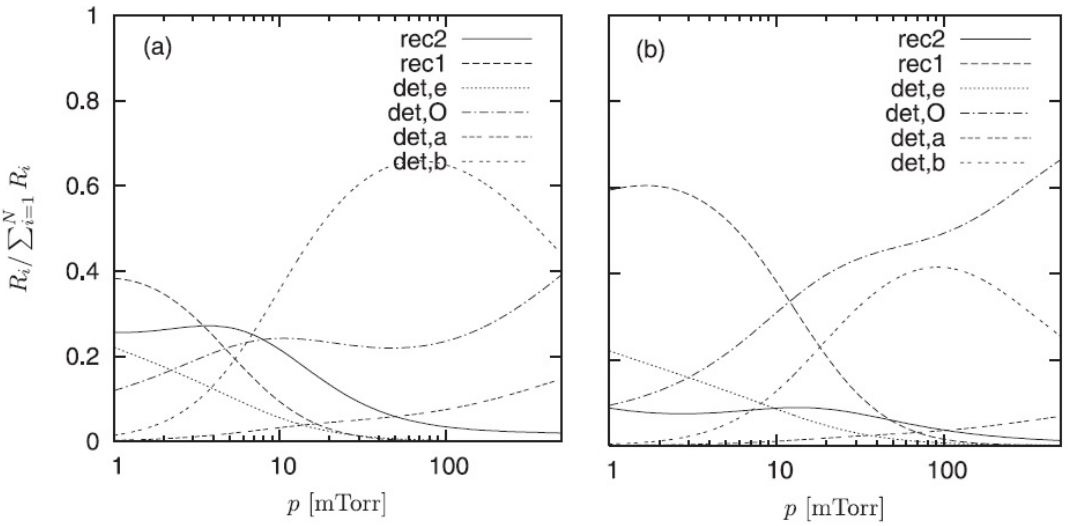

FIGURE 6.17 – Reaction rates as a function of pressure for O^- annihilation for a applied power of 300 W (a) and 1200 W (b) reported in [44].

Corr *et al.* [42] also reported that the main contributor to O^- annihilation at low pressures in an inductively coupled discharge is electron impact detachment. They reported results for an oxygen plasma in an inductive reactor in a pressure range of 1 – 50 mTorr for an applied power of 250 W. For pressures higher than 3 mTorr, they found that detachment by atomic oxygen in the main channel for O^- loss. Figure 6.16 also shows that the reaction rate of detachment by atomic oxygen (reaction 117) has an significant increase as pressure increases, but detachment by $O_2(b^1\Sigma_g^+)$ (reaction 116) and charge exchange between O^- and $O_2(X^3\Sigma_g^-)$ (reaction 113) also become important channels for O^- annihilation as pressure increases. Reactions 113 and 116 were not included in the model developed in [42].

Gudmundsson [44] also reported that detachment by atomic oxygen is significant for O^- annihilation at 25 mTorr and 300 W although the O^- annihilation was dominated by detachment by $O_2(b^1\Sigma_g^+)$. In [44], detachment by atomic oxygen overcomes detachment by $O_2(b^1\Sigma_g^+)$ at 25 mTorr and 1200 W. Corr *et al.* [42] also studied the power dependence of the reaction rates for O^- annihilation in an inductive discharge at 25 mTorr in the power range of 5 – 300 W (see figure 6.18). Their results showed that the O^- annihilation process is dominated by detachment by $O_2(a^1\Delta_g)$ at low powers (below 32 W approximately), while it is dominated by detachment by atomic oxygen at high powers (above 32 W approximately). Therefore, as the applied power increases, detachment by atomic oxygen overcomes detachment by the metastable state $b^1\Sigma_g^+$ in [44] while detachment by atomic oxygen overcomes detachment by the metastable state $a^1\Delta_g$ in [42]. It would be interesting if $O_2(b^1\Sigma_g^+)$ were included in the model developed in [42] to compare the results.

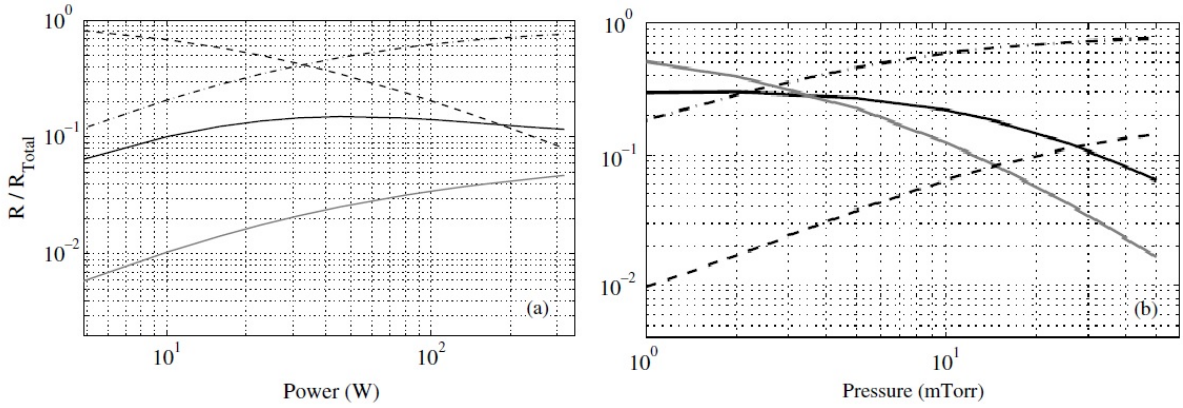

FIGURE 6.18 – Reaction rates as a function of pressure for O^- annihilation as a function of applied power for a pressure of 25 mTorr (a) and as a function of pressure for an applied power of 250 W (b) reported in [42].

Figure 6.18 (a) shows the reaction rates for O^- annihilation as a function of applied power for 25 mTorr and figure 6.18 (b) shows the reaction rates for O^- annihilation as a function of pressure for an applied power of 250 W reported in [42]. The dark full

line represents recombination reactions $O^- + O_2^+ \longrightarrow O(^3P) + O_2(X^3\Sigma_g^-)$, $O^- + O_2^+ \longrightarrow 3O(^3P)$, and $O^- + O^+ \longrightarrow 2O(^3P)$. The light full line represents electron impact detachment $e + O^- \longrightarrow 2e + O(^3P)$, the dash-dotted line represents detachment by atomic oxygen $O^- + O(^3P) \longrightarrow e + O_2(X^3\Sigma_g^-)$, and dashed line represents detachment by oxygen metastables $O^- + O_2(a^1\Delta_g) \longrightarrow e + O_3$.

There are not significant changes in the reaction rates for O^- annihilation for stainless steel reactor walls for $x = 0.5$ and $x = 2.0$. However, for anodized aluminum reactor walls, there is a significant increase in the reaction rate for detachment by the oxygen atom (reaction 117) which becomes increasingly more important as x increases. Figure 6.19 shows the reaction rates for O^- annihilation as a function of pressure for $x = 2.0$ and for anodized aluminium reactor walls.

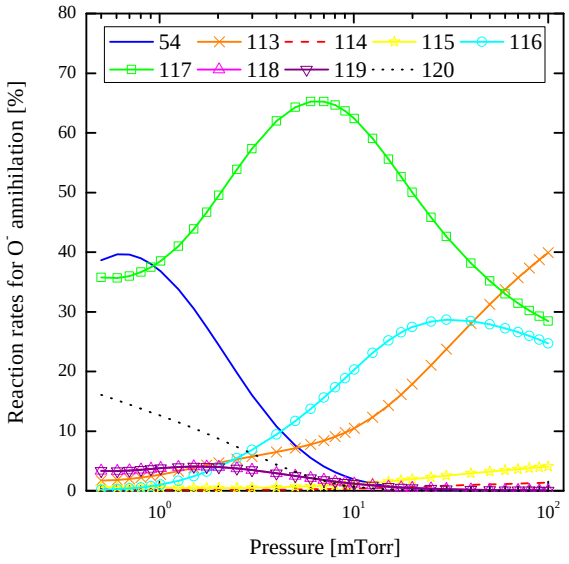

FIGURE 6.19 – Reaction rates for O^- annihilation as a function of pressure for $x = 2.0$ and for anodized aluminiuml reactor walls – other reactions with very small reaction rates are not shown in this figure.

Although density of O_2^- is lower than density of O^- at low pressure, it increases as pressure increases becoming comparable to density of O^- (see figure 6.14). The dominant channel for formation of O_2^- is charge exchange between O^- and $O_2(X^3\Sigma_g^-)$ (reaction 113) which represents approximately 90 % through the all range of pressure studied for the three values of x for stainless steel and anodized aluminium reactors.

Annihilation of O_2^- is not dominated by only one reaction, but many reactions contribute for it. Figure 6.20 shows the reaction rates for O_2^- annihilation as a function of pressure for reactions 101, 102, 103, 104, 105, 106, and 107 for $x = 1.0$ for (a) stainless steel and (b) anodized aluminium reactor walls. Reactions 99 and 100 also contribute to O_2^- annihilation, but their contributions are very small being neglected in these figures. Note that reaction rates for reactions 105 and 106 are the same because these reactions

have the same rate coefficients and they are recombinations of the same ions (see table 5.3).

For pressures below 2 mTorr, in stailess steel reactors, reactions 105 and 106 are the dominat channels, but their importance decreases as pressure increases while the contribution of reactions 101, 102, 103, and 104 increase. Thus, $O(^3P)$, $O_2(a^1\Delta_g)$, and $O_2(b^1\Sigma_g^+)$ are very important to the loss of O_2^- at high pressures. In anodized aluminium reactors, reactions 103 and 104 are the dominant channels in the all range of pressures studied due to the increase of the density of $O(^3P)$. For $x = 0.5$ and $x = 2.0$, there are minor changes in the reaction rates.

Formation of O_2^+ occurs mainly through electron impact ionization of the oxygen molecule in the ground state (reaction 7),

$$e + O_2(X^3\Sigma_g^-) \longrightarrow 2e + O_2^+.$$

This is the main channel in stainless steel or anodized aluminium reactors for the three x values studied. Annihilation of O_2^+ occurs mostly at the walls (reaction 135); however, for $x = 0.5$, in stainless steel and anodized aluminium reactors, dissociative recombination of the O_2^+-ion (reaction 45),

$$e + O_2^+ \longrightarrow O(^3P) + O(^1D),$$

also becomes an important channel for O_2^+ annihilation.

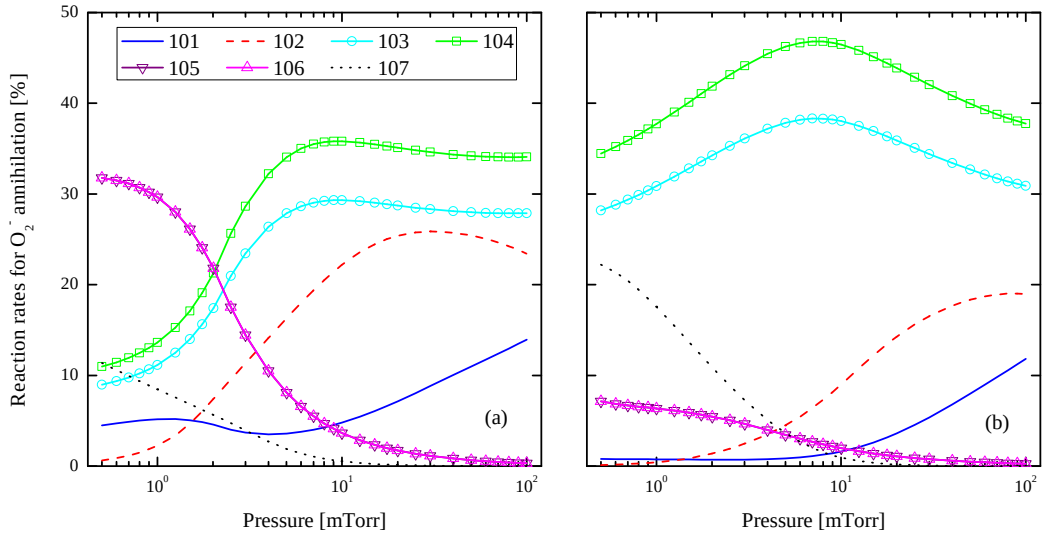

FIGURE 6.20 – Reaction rates for O_2^- annihilation as a function of pressure for $x = 1.0$ and for (a) stainless steel and (b) anodized aluminiuml reactor walls.

Figure 6.21 shows the reaction rates for the main channels for formation of O^+ as a function of pressure for $x = 1.0$ for (a) stailess steel and (b) anodized aluminium reactors. In stainless steel reactors, at low pressures, the main channels for formation of O^+ are

electron impact dissociative ionization of the ground state molecule (reaction 9),

$$e + O_2(X^3\Sigma_g^-) \longrightarrow 2e + O(^3P) + O^+,$$

and electron impact ionization of the oxygen atom in the ground state (reaction 47),

$$e + O(^3P) \longrightarrow 2e + O^+.$$

Electron impact ionization of the oxygen atomin the metastable state (reaction 55),

$$e + O(^1D) \longrightarrow 2e + O^+,$$

also has an important contribution to formation of O^+. As pressure increases, the contributions of reactions 9 and 55 decrease and reaction 47 becomes the dominant channel. In anodized aluminium reactors, reaction 47 is always the dominat channel. These results are also valid for $x = 2.0$ for stainless steel and anodized aluminium reactors. For $x = 0.5$, reaction 9 keeps as a significant contributor for formation of O^+ at high pressures in stainless steel reactors and becomes a significant contributor in anodized aluminium reactors.

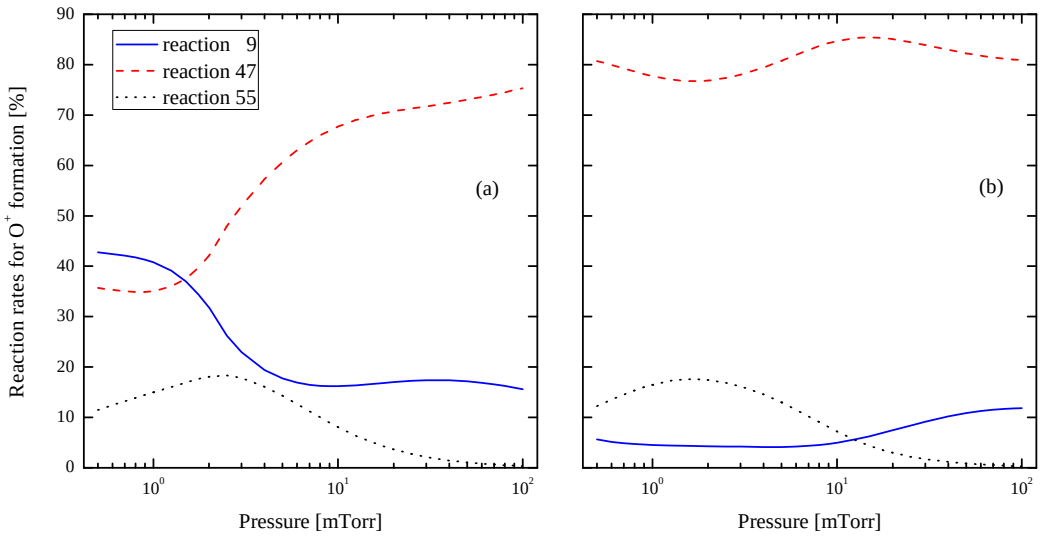

FIGURE 6.21 – Reaction rates for O^+ formation as a function of pressure for $x = 1.0$ and for (a) stainless steel and (b) anodized aluminiuml reactor walls.

The reaction rates for annihilation of O^+ do not show significant differences between stainless steel and anodized aluminium reactor walls. Figure 6.22 shows the reaction rates of reactions 121 and 136 for O^+ annihilation as a function of pressure in a stainless steel reactor for (a) $x = 0.5$ and (b) $x = 2.0$. The reaction rates of the other reactions that contribute for O^+ annihilation are very low being omitted in this figure. Results for $x = 1.0$ were also omitted because the interest here is show how the reaction rates change

as x increases. Note in the figure 6.22 (a) that the O^+ annihilation occurs mostly at the walls (reaction 136) at low pressures. As pressure increases, charge exchange (reaction 121),

$$O_2(X^3\Sigma_g^-) + O^+ \longrightarrow O(^3P) + O_2^+,$$

becomes an important channel for O^+ loss. As x increases, the increase of the reaction rate of the reaction 121 is less pronounced as one can note in the figure 6.22 (b) for $x = 2.0$. As results for O^+ annihilation does not depend on the wall materials studied, the increase of the density of O^+ is higher at low pressures due to the increase of the density of $O(^3P)$ that results in higher yield of O^+ through reaction 47 at low pressures as shown in figure 6.21 (b). These are similar findings reported earlier by Gudmundsson and Lieberman for an anodized aluminium chamber but assuming a low wall recombination coefficient for oxygen atoms [46].

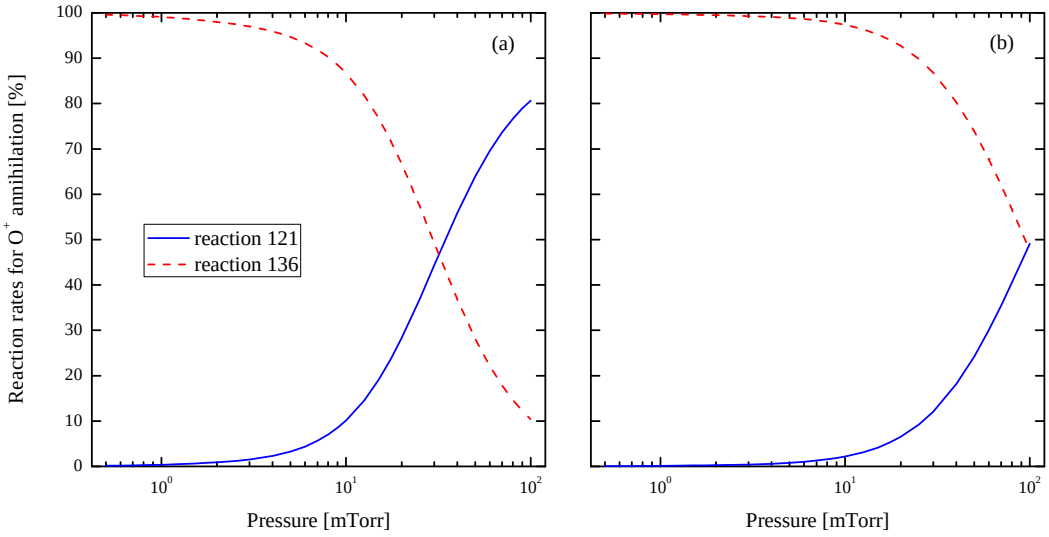

FIGURE 6.22 – Reaction rates for O^+ annihilation as a function of pressure for stainless steel reactor walls for (a) $x = 0.5$ and (b) $x = 2.0$.

Figure 6.23 shows the mean electronegativity $\alpha = n_-/n_e$ as a function of pressure for stainless steel and anodized aluminium reactor walls for $x = 0.5$, $x = 1.0$, and $x = 2.0$. The increase of the mean electronegativity as pressure increases due to the decrease of the mean electron density for high pressures. As x increases, the decrease of the mean electron density is more pronounced what explain the increase of the mean electronegativity. The variation of the electronegativity with EEDF in oxygen discharges is much more significant than what was observed for chlorine discharge in the same pressure range [50]. Measurements of the electronegativity in an inductively coupled oxygen discharge have given values in the range 1 – 1.5 in the pressure range 5 – 30 mTorr and 900 W input power and increasing with increasing pressure [143] and in the range 0.02 – 0.2 in the pressure range 1 – 45 mTorr and absorbed power of 220 W [42]. Furthermore, Corr *et*

al [42] show that the negative ion densities have maximum values around 20 mTorr in the inductively coupled mode. They also show that the electronegativity also displays a strong dependence on gas pressure.

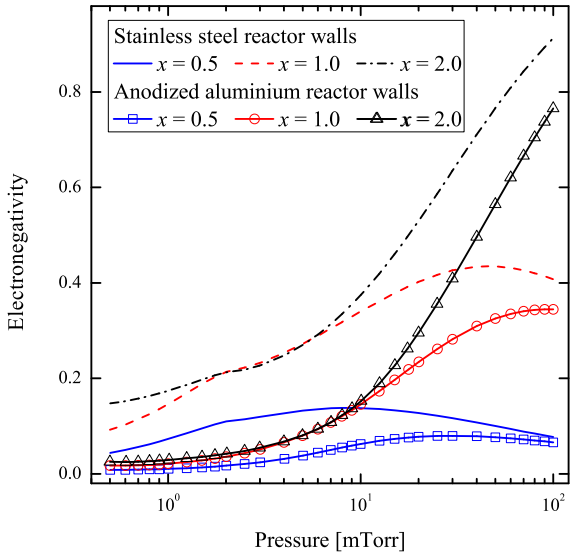

FIGURE 6.23 – The mean electronegativity as a function of pressure for $x = 0.5$, $x = 1.0$, and $x = 2.0$ for stainless steel and anodized aluminium reactors.

An additional study can be made by evaluating changes in the quenching coefficient at the walls for $O_2(b^1\Sigma_g^+)$ since this is a very important parameter and there are limited information about it. Figure 6.24 (a) shows the density of $O_2(b^1\Sigma_g^+)$ and figure 6.24 (b) shows the mean electronegativity both as a function of pressure for $x = 1.0$, stainless steel reactor walls, and $\gamma = 0.001$, 0.01, 0.1, and 1. The density of $O_2(b^1\Sigma_g^+)$ increases as γ decreases as expected; however, the density of $O_2(a^1\Delta_g)$ does not show any significant change. The density of $O_2(b^1\Sigma_g^+)$ can overcome the density of $O_2(a^1\Delta_g)$ for $\gamma = 0.001$, 0.01, and 0.1 while the density of $O_2(b^1\Sigma_g^+)$ does not overcome the density of $O_2(a^1\Delta_g)$ for $\gamma = 1$ in the range of pressure studied.

Since detachment by collision with $O_2(b^1\Sigma_g^+)$ (reaction 116),

$$O^- + O_2(b^1\Sigma_g^+) \longrightarrow e + O(^3P) + O_2(X^3\Sigma_g^-),$$

is an important channel for O^- annihilation for pressures above 2 mTorr [52], it would be expected the decrease of the density of O^- due to the increase of the density of $O_2(b^1\Sigma_g^+)$ for low quenching coefficients, nevertheless this does not happen. The annihilation of O^- through detachment by collision with $O_2(b^1\Sigma_g^+)$ is compensated by the formation of O^- through dissociative attachment from the $b^1\Sigma_g^+$ state (reaction 37),

$$e + O_2(b^1\Sigma_g^+) \longrightarrow O(^3P) + O^-,$$

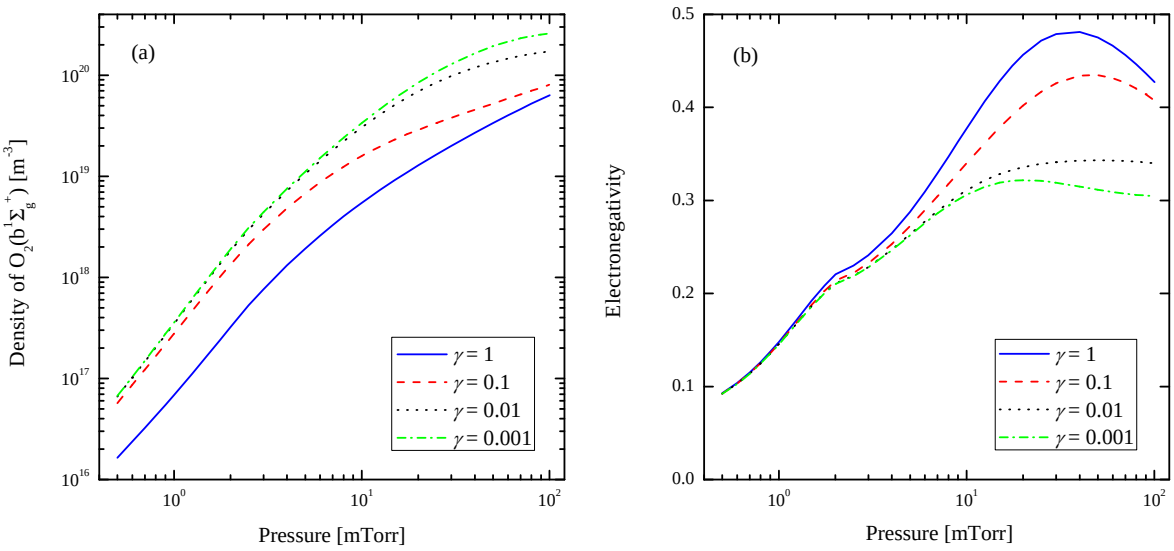

FIGURE 6.24 – (a) The mean density of $O_2(b^1\Sigma_g^+)$ and (b) the mean electronegativity as a function of pressure for $\gamma = 0.001$, 0.01, 0.1, and 1 for stainless steel reactor and $x = 1.0$.

resulting in a very small decrease of the density of O^- for pressures above 10 mTorr. The density of O_2^- decreases as the density of $O_2(b^1\Sigma_g^+)$ increases due to the decrease of the quenching coefficient at the walls. This occurs because detachment through collision with $O_2(b^1\Sigma_g^+)$ (reaction 102),

$$O_2^- + O_2(b^1\Sigma_g^+) \longrightarrow e + O_2(X^3\Sigma_g^-) + O_2(X^3\Sigma_g^-),$$

becomes an important channel for O_2^- annihilation. This explains the decrease of the mean electronegativity as the quenching coefficient decreases (see figure 6.24). Note that the difference in the mean electronegativity disappears for low pressures because the density of $O_2(b^1\Sigma_g^+)$ is small and its effects become negligible.

7 The Bohm criterion issue

Due to the mass difference, electrons acquire velocities much higher than the velocities of ions when they are subjected to an electric field. Hence, at bounded plasmas, the electron flux to the walls of the reactor is much higher than the ion flux. Thereby, the walls acquire a negative potential creating the sheath region that is the region where an electric field acts to repel electrons and negative ions and attract positive ions. Low energy electrons are repelled to the bulk of the plasma but high energy electrons can overcome the sheath potential reaching the walls. The sheath region promotes the equalization of the flux of electrons and positive ions to the walls. The velocity of the positive ions at the sheath edge in a weakly collisional plasma with a single-ion species is given by the Bohm criterion [144–146]

$$u_{\mathrm{B}} = \left(\frac{kT_{\mathrm{e}}}{M}\right)^{1/2}. \tag{7.1}$$

where k is the Boltzmann constant, T_{e} is the electron temperature, and M is the mass of the ion. For an electronegative plasma, the Bohm criterion becomes [129]

$$u_{\mathrm{B}} = \left[\frac{kT_{\mathrm{e}}(1+\alpha_{\mathrm{s}})}{M(1+\alpha_{\mathrm{s}}\gamma_{-})}\right]^{1/2}. \tag{7.2}$$

where α_{s} is the electronegativity at the sheath edge, i.e., the ratio between the negative ion density and the electron density, and γ_{-} is the ratio between the electron temperature T_{e} and the negative ion temperature T_{i}.

The equations 7.1 and 7.2 were obtained for a Maxwellian EEDF. To a EEDF that can be represented by the equation 5.3, the Bohm criterion for an electropsitive plasma becomes [47]

$$u_{\mathrm{B}} = \langle\varepsilon\rangle^{1/2}\left(\frac{2}{M}\right)^{1/2}\frac{\Gamma(\xi_1)}{[\Gamma(\xi_2)\Gamma(\xi_3)]^{1/2}}. \tag{7.3}$$

where $\xi_3 = 1/2x$. As a try to include the negative ion effects, the latter equation was

changed to [52]:

$$u_{\mathrm{B}} = \langle \varepsilon \rangle^{1/2} \left(\frac{2}{M} \right)^{1/2} \left[\frac{(1+\alpha_{\mathrm{s}})}{(1+\alpha_{\mathrm{s}}\gamma_{-})} \right]^{1/2} \frac{\Gamma(\xi_1)}{[\Gamma(\xi_2)\Gamma(\xi_3)]^{1/2}}. \tag{7.4}$$

The equations 7.1 and 7.3 are valid for electropositive plasmas which have only one positive ion species and the equation 7.2 is valid for electronegative plasmas which have only one positive ion species and one negative ion species. Many species of positive and negative ions in the plasma result in changes in these equations. Allen [147] showed that the velocity of the ions at the sheath edge could be calculated through the dispersion relation. At the sheath edge, the dispersion relation is given by [148, 149]

$$w_{\mathrm{pe}}^2 \int_{-\infty}^{+\infty} \frac{f_{\mathrm{e}}(v)}{(w-\kappa v)^2} \mathrm{d}v + \sum_i w_{\mathrm{pn},i}^2 \int_{-\infty}^{+\infty} \frac{f_{\mathrm{n},i}(v)}{(w-\kappa v)^2} \mathrm{d}v + \\ + \sum_j w_{\mathrm{pp},j}^2 \int_{-\infty}^{+\infty} \frac{f_{\mathrm{p},j}(v)}{(w-\kappa v)^2} \mathrm{d}v = 1, \tag{7.5}$$

where ω is the angular frequency, κ is the wave number, ω_{pe} is the angular plasma frequency of electron, ω_{pn} is the angular plasma frequency of negative ion, ω_{pp} is the angular plasma frequency of positive ion, f_{e} is the velocity distribution function of the electrons, $f_{\mathrm{n},i}$ is the velocity distribution function of the ith negative ion species, and $f_{\mathrm{p},j}$ is the velocity distribution function of the jth positive ion species. Substituting in the latter equation $\omega_{\mathrm{pe}}^2 = n_{\mathrm{e}}e^2/\varepsilon_0 m_{\mathrm{e}}$, $\omega_{\mathrm{pn}}^2 = n_{\mathrm{n}}e^2/\varepsilon_0 m_{\mathrm{n}}$, and $\omega_{\mathrm{pp}}^2 = n_{\mathrm{p}}e^2/\varepsilon_0 m_{\mathrm{p}}$ we have

$$\frac{n_{\mathrm{e}}e^2}{\varepsilon_0 m_{\mathrm{e}}} \int_{-\infty}^{+\infty} \frac{f_{\mathrm{e}}(v)}{(w-\kappa v)^2} \mathrm{d}v + \sum_i \frac{n_{\mathrm{n},i}e^2}{\varepsilon_0 m_{\mathrm{n}}} \int_{-\infty}^{+\infty} \frac{f_{\mathrm{n},i}(v)}{(w-\kappa v)^2} \mathrm{d}v + \\ + \sum_j \frac{n_{\mathrm{p},j}e^2}{\varepsilon_0 m_{\mathrm{p}}} \int_{-\infty}^{+\infty} \frac{f_{\mathrm{p},j}(v)}{(w-\kappa v)^2} \mathrm{d}v = 1, \tag{7.6}$$

where n_{e} is the density of electrons at the sheath edge, $n_{\mathrm{n},i}$ is the density of the ith negative ion species at the sheath edge, $n_{\mathrm{p},j}$ is the density of the jth positive ion species at the sheath edge, e is the elementary charge, ε_0 is the vacuum permittivity, m_{e} is the electron mass, $m_{\mathrm{n},i}$ is the mass of the ith negative ion species, and $m_{\mathrm{p},j}$ is the mass of the jth positive ion species. In the steady state, one can assume that the angular frequency is null [148, 149]. Thus, we have:

$$\frac{n_{\mathrm{e}}e^2}{\varepsilon_0 m_{\mathrm{e}}} \int_{-\infty}^{+\infty} \frac{f_{\mathrm{e}}(v)}{v^2} \mathrm{d}v + \sum_i \frac{n_{\mathrm{n},i}e^2}{\varepsilon_0 m_{\mathrm{n}}} \int_{-\infty}^{+\infty} \frac{f_{\mathrm{n},i}(v)}{v^2} \mathrm{d}v + \\ + \sum_j \frac{n_{\mathrm{p},j}e^2}{\varepsilon_0 m_{\mathrm{p}}} \int_{-\infty}^{+\infty} \frac{f_{\mathrm{p},j}(v)}{v^2} \mathrm{d}v = \kappa^2. \tag{7.7}$$

Multiplying the latter equation by $1/n_0$ and using the charge neutrality condition $n_0 = n_\mathrm{e} + \sum_i n_{\mathrm{n},i} = \sum_j n_{\mathrm{p},j}$ we have:

$$\left[1 - \left(\sum_i \frac{n_{\mathrm{n},i}}{n_0}\right)\right] \frac{e^2}{\varepsilon_0 m_\mathrm{e}} \int_{-\infty}^{+\infty} \frac{f_\mathrm{e}(v)}{v^2}\mathrm{d}v + \sum_i \frac{n_{\mathrm{n},i}}{n_0} \frac{e^2}{\varepsilon_0 m_\mathrm{n}} \int_{-\infty}^{+\infty} \frac{f_{\mathrm{n},i}(v)}{v^2}\mathrm{d}v + \\ + \sum_j \frac{n_{\mathrm{p},j}}{n_0} \frac{e^2}{\varepsilon_0 m_\mathrm{p}} \int_{-\infty}^{+\infty} \frac{f_{\mathrm{p},j}(v)}{v^2}\mathrm{d}v = \frac{\kappa^2}{n_0}. \tag{7.8}$$

Multiplying this equation by ε_0/e^2 we have:

$$\left[1 - \left(\sum_i \frac{n_{\mathrm{n},i}}{n_0}\right)\right] \frac{1}{m_\mathrm{e}} \int_{-\infty}^{+\infty} \frac{f_\mathrm{e}(v)}{v^2}\mathrm{d}v + \sum_i \frac{n_{\mathrm{n},i}}{n_0} \frac{1}{m_\mathrm{n}} \int_{-\infty}^{+\infty} \frac{f_{\mathrm{n},i}(v)}{v^2}\mathrm{d}v + \\ + \sum_j \frac{n_{\mathrm{p},j}}{n_0} \frac{1}{m_\mathrm{p}} \int_{-\infty}^{+\infty} \frac{f_{\mathrm{p},j}(v)}{v^2}\mathrm{d}v = \frac{\kappa^2}{n_0} = \frac{\kappa^2 {\lambda_\mathrm{D}}^2}{m_\mathrm{e} \left\langle v^2/2 \right\rangle^{1/2}}. \tag{7.9}$$

where $\lambda_\mathrm{D} \equiv \left\langle v_\mathrm{e}^2/2 \right\rangle^{1/2} \omega_\mathrm{pe}^{-1}$ is the Debey length. If sheath width is much larger than Debey length we can assume κ to be small, therefore $\kappa\lambda_\mathrm{D} \to 0$ [148, 149]. Then,

$$\sum_j \frac{n_{\mathrm{p},j}}{n_0} \frac{1}{m_\mathrm{p}} \int_{-\infty}^{+\infty} \frac{f_{\mathrm{p},j}(v)}{v^2}\mathrm{d}v = -\left[1 - \left(\sum_i \frac{n_{\mathrm{n},i}}{n_0}\right)\right] \frac{1}{m_\mathrm{e}} \int_{-\infty}^{+\infty} \frac{f_\mathrm{e}(v)}{v^2}\mathrm{d}v + \\ + \sum_i \frac{n_{\mathrm{n},i}}{n_0} \frac{1}{m_\mathrm{n}} \int_{-\infty}^{+\infty} \frac{f_{\mathrm{n},i}(v)}{v^2}\mathrm{d}v. \tag{7.10}$$

Using $\langle v^{-2} \rangle = \int f(v)/v^2 \mathrm{d}v$ for positive ions, we have:

$$\sum_j \frac{n_{\mathrm{p},j}}{n_0} \frac{\left\langle {v_{\mathrm{p},j}}^{-2} \right\rangle}{m_\mathrm{p}} = -\left[1 - \left(\sum_i \frac{n_{\mathrm{n},i}}{n_0}\right)\right] \frac{1}{m_\mathrm{e}} \int_{-\infty}^{+\infty} \frac{f_\mathrm{e}(v)}{v^2}\mathrm{d}v + \\ + \sum_i \frac{n_{\mathrm{n},i}}{n_0} \frac{1}{m_\mathrm{n}} \int_{-\infty}^{+\infty} \frac{f_{\mathrm{n},i}(v)}{v^2}\mathrm{d}v. \tag{7.11}$$

Since the distribution functions annul in $\pm\infty$, one can use integration by parts to obtain:

$$\sum_j \frac{n_{\mathrm{p},j}}{n_0} \frac{\left\langle {v_{\mathrm{p},j}}^{-2} \right\rangle}{m_\mathrm{p}} = \left[1 - \left(\sum_i \frac{n_{\mathrm{n},i}}{n_0}\right)\right] \int_0^{+\infty} \frac{F_\mathrm{e}(\varepsilon)}{2\varepsilon}\mathrm{d}\varepsilon + \\ + \sum_i \frac{n_{\mathrm{n},i}}{n_0} \int_0^{+\infty} \frac{F_{\mathrm{n},i}(\varepsilon)}{2\varepsilon}\mathrm{d}\varepsilon. \tag{7.12}$$

Using the approximation $\langle {v_\mathrm{p}}^{-2} \rangle = \langle {v_\mathrm{p}}^{2} \rangle^{-1}$ [148, 149] we have:

$$\sum_j \frac{n_{\mathrm{p},j}}{n_0} \frac{1}{m_\mathrm{p} \langle {v_{\mathrm{p},j}}^2 \rangle} = \left[1 - \left(\sum_i \frac{n_{\mathrm{n},i}}{n_0} \right) \right] \int_0^{+\infty} \frac{F_\mathrm{e}(\varepsilon)}{2\varepsilon} \mathrm{d}\varepsilon + \\ + \sum_i \frac{n_{\mathrm{n},i}}{n_0} \int_0^{+\infty} \frac{F_{\mathrm{n},i}(\varepsilon)}{2\varepsilon} \mathrm{d}\varepsilon. \tag{7.13}$$

Assuming that all positive ion species reach the walls at the same velocity, we have:

$$\langle {v_\mathrm{p}}^2 \rangle = \sum_j \frac{n_{\mathrm{p},j}}{n_0 m_{\mathrm{p},j}} \left\{ \left[1 - \left(\sum_i \frac{n_{\mathrm{n},i}}{n_0} \right) \right] \int_0^{+\infty} \frac{F_\mathrm{e}(\varepsilon)}{2\varepsilon} \mathrm{d}\varepsilon + \sum_i \frac{n_{\mathrm{n},i}}{n_0} \int_0^{+\infty} \frac{F_{\mathrm{n},i}(\varepsilon)}{2\varepsilon} \mathrm{d}\varepsilon \right\}^{-1} \tag{7.14}$$

As [47]

$$\int_0^{+\infty} \frac{F(\varepsilon)}{\varepsilon} \mathrm{d}\varepsilon = \frac{c_1}{{c_2}^{\xi_3} x} \Gamma(\xi_3) \tag{7.15}$$

and assuming that all negative ion species have the same energy distribution function, we have:

$$\langle {v_\mathrm{p}}^2 \rangle = \sum_j \frac{2n_{\mathrm{p},j}}{n_0 m_{\mathrm{p},j}} \left\{ \left[1 - \left(\sum_i \frac{n_{\mathrm{n},i}}{n_0} \right) \right] \frac{c_{1,\mathrm{e}}}{{c_{2,\mathrm{e}}}^{\xi_{3,\mathrm{e}}} x_\mathrm{e}} \Gamma(\xi_{3,\mathrm{e}}) + \sum_i \frac{n_{\mathrm{n},i}}{n_0} \frac{c_{1,\mathrm{n}}}{{c_{2,\mathrm{n}}}^{\xi_{3,\mathrm{n}}} x_\mathrm{n}} \Gamma(\xi_{3,\mathrm{n}}) \right\}^{-1} \tag{7.16}$$

where

$$c_{1,\mathrm{e}} = \frac{x_\mathrm{e}}{\langle \varepsilon_\mathrm{e} \rangle^{3/2}} \frac{\Gamma(\xi_{2,\mathrm{e}})^{3/2}}{\Gamma(\xi_{1,\mathrm{e}})^{5/2}}, \tag{7.17}$$

$$c_{2,\mathrm{e}} = \frac{1}{\langle \varepsilon_\mathrm{e} \rangle^{x_\mathrm{e}}} \left[\frac{\Gamma(\xi_{2,\mathrm{e}})}{\Gamma(\xi_{1,\mathrm{e}})} \right]^{x_\mathrm{e}}, \tag{7.18}$$

$$c_{1,\mathrm{n}} = \frac{x_\mathrm{n}}{\langle \varepsilon_\mathrm{n} \rangle^{3/2}} \frac{\Gamma(\xi_{2,\mathrm{n}})^{3/2}}{\Gamma(\xi_{1,\mathrm{n}})^{5/2}} \tag{7.19}$$

and

$$c_{2,\mathrm{n}} = \frac{1}{\langle \varepsilon_\mathrm{n} \rangle^{x_\mathrm{n}}} \left[\frac{\Gamma(\xi_{2,\mathrm{n}})}{\Gamma(\xi_{1,\mathrm{n}})} \right]^{x_\mathrm{n}}, \tag{7.20}$$

wherein $\xi_{1,\mathrm{e}} = 3/2x_\mathrm{e}$, $\xi_{2,\mathrm{e}} = 5/2x_\mathrm{e}$, $\xi_{3,\mathrm{e}} = 1/2x_\mathrm{e}$, $\xi_{1,\mathrm{n}} = 3/2x_\mathrm{n}$, $\xi_{2,\mathrm{n}} = 5/2x_\mathrm{n}$, $\xi_{3,\mathrm{n}} = 1/2x_\mathrm{n}$,

$\langle \varepsilon_{\rm e} \rangle = 3kT_{\rm eff}/2$, and $\langle \varepsilon_{\rm n} \rangle = 3kT_{\rm i}/2$. Note

$$1 - \sum_i \frac{n_{{\rm n},i}}{n_0} = \frac{n_0 - \sum_i n_{{\rm n},i}}{n_0} = \frac{n_{\rm e}}{n_0} = \left(\frac{n_0}{n_{\rm e}}\right)^{-1} = \left(\frac{n_{\rm e} + \sum_i n_{{\rm n},i}}{n_{\rm e}}\right)^{-1} = \quad (7.21)$$
$$= (1+\alpha_{\rm s})^{-1} = \frac{1}{1+\alpha_{\rm s}}$$

and

$$\sum_i \frac{n_{{\rm n},i}}{n_0} = \left(\frac{n_0}{\sum_i n_{{\rm n},i}}\right)^{-1} = \left(\frac{\sum_i n_{{\rm n},i} + n_{\rm e}}{\sum_i n_{{\rm n},i}}\right)^{-1} = \left(1 + \frac{n_{\rm e}}{\sum_i n_{{\rm n},i}}\right)^{-1} = \quad (7.22)$$
$$= \left(1 + \frac{1}{\alpha_{\rm s}}\right)^{-1} = \left(\frac{\alpha_{\rm s}+1}{\alpha_{\rm s}}\right)^{-1} = \frac{\alpha_{\rm s}}{\alpha_{\rm s}+1},$$

therefore

$$\left\langle {v_{\rm p}}^2 \right\rangle = \sum_j \frac{2n_{{\rm p},j}}{n_0 m_{{\rm p},j}} \left[\frac{1}{1+\alpha_{\rm s}} \frac{c_{1,{\rm e}}}{{c_{2,{\rm e}}}^{\xi_{3,{\rm e}}} x_{\rm e}} \Gamma(\xi_{3,{\rm e}}) + \frac{\alpha_{\rm s}}{\alpha_{\rm s}+1} \frac{c_{1,{\rm n}}}{{c_{2,{\rm n}}}^{\xi_{3,{\rm n}}} x_{\rm n}} \Gamma(\xi_{3,{\rm n}}) \right]^{-1} \quad (7.23)$$

or

$$c_{\rm s} = \left\{ \sum_j \frac{2n_{{\rm p},j}}{n_0 m_{{\rm p},j}} \left[\frac{1}{1+\alpha_{\rm s}} \frac{c_{1,{\rm e}}}{{c_{2,{\rm e}}}^{\xi_{3,{\rm e}}} x_{\rm e}} \Gamma(\xi_{3,{\rm e}}) + \frac{\alpha_{\rm s}}{\alpha_{\rm s}+1} \frac{c_{1,{\rm n}}}{{c_{2,{\rm n}}}^{\xi_{3,{\rm n}}} x_{\rm n}} \Gamma(\xi_{3,{\rm n}}) \right]^{-1} \right\}^{1/2}. \quad (7.24)$$

For $x_{\rm e} = 1$ and $x_{\rm n} = 1$ (Maxwellian distributions for electrons and negative ions), equation 7.24 becomes

$$c_{\rm s} = \left\{ \sum_j \frac{n_{{\rm p},j}}{n_0 m_{{\rm p},j}} \left[\frac{1}{kT_{\rm e}(1+\alpha_{\rm s})} + \frac{\alpha_{\rm s}}{kT_{\rm i}(\alpha_{\rm s}+1)} \right]^{-1} \right\}^{1/2}. \quad (7.25)$$

For one species of positive ion, equation 7.25 becomes

$$c_{\rm s} = \left[\frac{kT_{\rm e}(1+\alpha_{\rm s})}{M(1+\alpha_{\rm s}\gamma_-)} \right]^{1/2} \quad (7.26)$$

which is equation 7.2.

The approximation $\langle {v_{\rm p}}^{-2} \rangle = \langle {v_{\rm p}}^2 \rangle^{-1}$ does not hold for most distribution functions of interest; however, Amemiya [148, 149] justify it arguing that positive ions at the plasma-sheath edge have a velocity distribution function with a narrow velocity width due to the acceleration by a weak electric field. The other controversial issue is the assumption that all positive ion species have the same velocity at the plasma-sheath edge. Lee *et al* [54] reported experimental results for a Ar/Xe plasma claiming that the velocities of the Ar^+ and Xe^+ ions at the plasma-sheath edge does not satisfy the Bohm criterion

being closer to the ion sound speed of the system that is the velocity obtained by solving the generalized Bohm criterion with the assumption that all ions reach the plasma-sheath edge with the same velocity. Baalrud *et al* [150] explained these results by the theory of instability-induced friction. Gudmundsson and Lieberman [151] through a 1 D particle-in-cell Monte Carlo simulation of an Ar/Xe plasma reported that Ar^+ and Xe^+ ions have their own Bohm velocity contradicting the previous experimental results. However, the computational results of Gudmundsson and Lieberman were contested [152].

There are two experimental results published recently. Yip *et al* [55] added krypton to an Ar/Xe plasma and found that the Ar^+ and Xe^+ velocities at the plasma-sheath edge approximate to their own Bohm velocities as the krypton quantity in the plasma increases which support the theory proposed by Baalrud *et al* [150]. Sobolewski *et al* [56] measured the velocities of the ions CF_3^+, CF_2^+, CF^+, and F^+ at the plasma-sheath edge in a RF ICP in CF_4. They found that all ions have the same velocity which is lower than their Bohm velocity and the ion sound speed of the system. They also claimed that the sheath models will need to be revised.

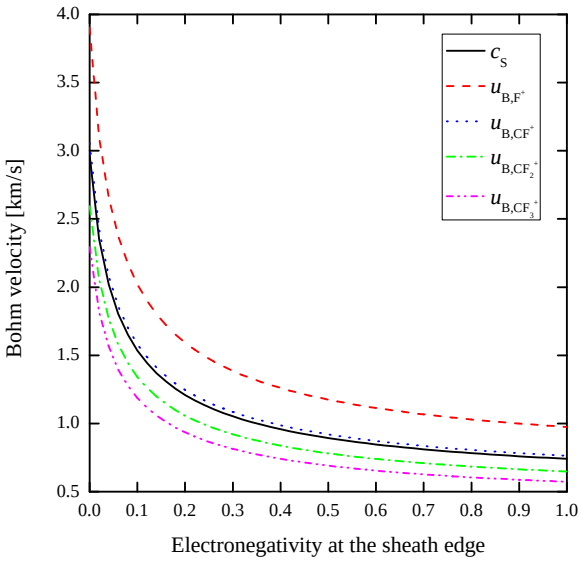

FIGURE 7.1 – Bohm velocity of CF_3^+, CF_2^+, CF^+, and F^+ ions calculated by equation 7.2 and the ion sound speed of the system calculated by equation 7.24 as a function of the electronegativity at the sheath edge for T_e=3 eV and p=10 mTorr.

Equation 7.24 could be taken as the ion sound speed of the system for a plasma with different positive and negative ions. It still considers distribution functions for electrons and negative ions that can be expressed by equation 5.3. Studies that seek for a Bohm criterion for general distribution functions can be found in [153–157]. To explain their results, Sobolewski *et al* [56] suggested that the negative ions would reduce the ion sound speed. Although equation 7.24 was obtained through assumptions that can be criticized, it predicts that the ion sound speed decreases due to negative ion effects at the sheath

edge as can be seen in figure 6.1. The ion densities at the sheath edge were assumed as $n_{F^+} = 0.6 \times 10^{-16}\mathrm{m}^{-3}$, $n_{CF^+} = 0.77 \times 10^{-16}\mathrm{m}^{-3}$, $n_{CF_2^+} = 0.63 \times 10^{-16}\mathrm{m}^{-3}$, and $n_{CF_3^+} = 0.84 \times 10^{-16}\mathrm{m}^{-3}$ that are values reported for 1 mTorr and 550 W [158]. Note that equation 7.24 results in values between the Bohm velocities of the ions.

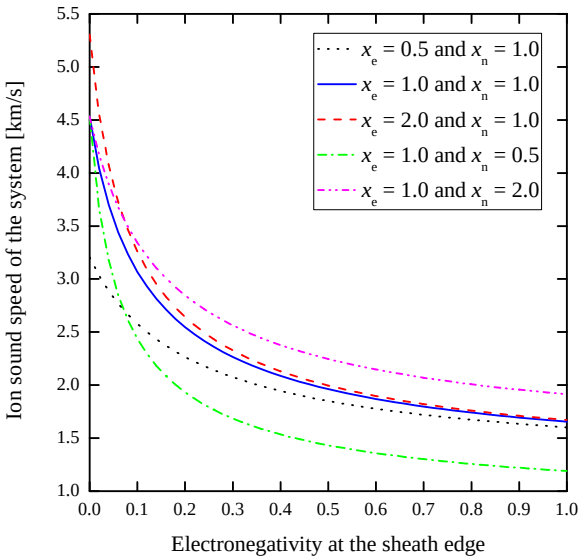

FIGURE 7.2 – The ion sound speed of the system calculated by equation 7.24 as a function of the electronegativity at the sheath edge for different values of x_n and x_e, T_e=7 eV, and p=3 mTorr for a CF_4 plasma considering the CF_3^+, CF_2^+, CF^+, and F^+ ions.

Figure 6.2 shows the changes in the ion sound speed of the system caused by changes in the energy distribution functions of electrons and negative ions. From the first three curves for $x_e = 0.5$ and $x_n = 1.0$, for $x_e = 1.0$ and $x_n = 1.0$, for $x_e = 2.0$ and $x_n = 1.0$, one can see that changes in the EEDF are significant for low values of the electronegativity ate the sheath edge, i.e., when the density of negative ions is low in that region. Increasing the density of negative ions at the sheath edge, changes in the EEDF can be neglected. Changes in the energy distribution function for negative ions results in significant differences in the ion sound speed of the system in almost all the range of the electronegativity evaluated here as one can see in the curves for $x_e = 1.0$ and $x_n = 0.5$, for $x_e = 1.0$ and $x_n = 1.0$, and for $x_e = 1.0$ and $x_n = 2.0$. Increasing x_n the ion sound speed of the system increases. Note that the results for different values of x_n are close only for low electronegativity values as expected due to the low density of negative ions.

8 Conclusions

A volume averaged global model was developed in this work to study the effects of changes in the EEDF in a low pressure high density oxygen discharges for a stainless steel reactor and an anodized aluminium reactor. The EEDF was represented by equation 5.3 which is a function of the parameter x. Equation 5.3 represents an EEDF that approximates an bi-Maxwellian EEDF as $x = 0.5$, a Maxwellian EEDF as $x = 1.0$, and a Druyvesteyn EEDF as $x = 2.0$. Although bi-Maxwellian EEDFs are not usually verified experimentally for planar inductive oxygen discharges, calculations for $x = 0.5$.

Results showed minor changes in the density of neutral species for the three values of x. Regarding the differences in the density of neutral species due to the wall material of the reactor, the most significant change was the increase of the density of the oxygen atom for low pressures because of the low recombination coefficient for oxygen atoms at anodized aluminium surfaces. Results also showed values for the density of $O_2(b^1\Sigma_g^+)$ higher than it was expected. Analyzing the reaction rates for formation of $O_2(b^1\Sigma_g^+)$, one could conclude that the reaction of energy transfer from the singlet metastable oxygen atom $O(^1D)$ to the oxygen molecule in the ground state $O_2(X^3\Sigma_g^-)$, $O(^1D) + O_2(X^3\Sigma_g^-) \longrightarrow O(^3P) + O_2(b^1\Sigma_g^+)$, is the responsible for it. This reaction is usually not included in the reaction set for modelling of oxygen discharges which explain the different results.

The densities of the Herzberg states $O_2(A^3\Sigma_u^+, A'^3\Delta_u, c^1\Sigma_u^-)$ and ozone O_3 are low if compared to the other neutral species. Therefore, neglecting these species in the reaction set in more computationally intensive models such as fluid models and particle-in-cell Monte Carlo collision simulations may be justified.

Different from the neutral species, the charged species showed significant changes for different EEDFs. Results showed that the density of electrons decreases as x increases. This implies in an increase in the effective electron temperature as x increases due to the mathematical relationship between mean electron density and effective electron temperature presented in the chapter5. Therefore, when EEDFs depleted of high energy electrons are used in the calculations like Druyvesteyn EEDF, the mean electron energy is higher favoring reactions with higher threshold energy as dicussed for the reaction rates for formation of O^-. As the density of O^- is higher than the densities of O_2^- and O_3^-,

it is important to the charge equilibrium of the plasma. Therefore, the loss of O^- in the plasma is a polemic issue. Results showed that the electron-impact detachment, e + O^- $\longrightarrow$ 2e + $O(^3P)$, is the main channel for O^- loss at low pressures in stainless steel reactors. As pressure increases, the main channels for O^- annihilation in stainless steel reactors becomes charge exchange between O^- and $O_2(X^3\Sigma_g^-)$, $O^- + O_2(X^3\Sigma_g^-) \longrightarrow O(^3P) + O_2^-$, electron detachment by collision with $O_2(b^1\Sigma_g^+)$, $O^- + O_2(b^1\Sigma_g^+) \longrightarrow e + O(^3P) + O_2(X^3\Sigma_g^-)$, and electron detachment by collision with $O(^3P)$, $O^- + O(^3P) \longrightarrow e + O_2(X^3\Sigma_g^-)$. These results were compared with the results reported in the literature. In anodized aluminium reactors, there is a pronounced increase in the rection rate for electron detachment by collision with $O(^3P)$ for annihilation of O^-. Although the density of O_2^- is lower than the density of O^-, it increases as pressure increases.

In stainless steel reactor, O_2^+ is the positive charged species that is found in higher amount for the three x values. In anodized aluminium reactors, the oxygen atom ion O^+ is the dominant species for low pressures. As pressure decreases, the density of O^+ has a deep decrease and the density of O_2^+ increases, therefore O_2^+ becomes the dominant positive charged species at high pressures in anodized aluminium reactors. The densities of ozone ions O_3^+ and O_3^- are very low; therefore, neglect these ions is also justified in oxygen discharge modelling.

In previous works, an expression for the Bohm velocity for non-Maxwellian EEDF were obtained from the dispersion relation. Through some approximations, the previous calculations were extended resulting in an expression for the ion sound speed of the system which include many species of positive and negative ions and non-Maxwellian energy distribution functions for negative ions and electrons. This expression shows that the ion sound speed of the system decreases as the density of negative ions at the sheath edge increases as the Bohm velocity in an electronegative plasma. It also shows that changes in the EEDF are significant when the density of negative ions at the sheath edge is low. As the densinty of the negative ions at the sheath edge increases, changes in the ion sound speed of the system due to different EEDFs can be neglected. However, changes in the energy distribution functions for negative ions result in significant changes in the ion sound speed of the system in the range of electronegativity studied for different values of electron temperatures and pressures.

In future works, it is intended to develop a volume averaged global model to study oxygen plasmas in capacitive reactors. Then, metastable states in CF_4 plasma will be studied for inductive and capacitive reactors. The expression for the ion sound speed of the system obtained in this work will be implemented in the model allowing a proper evaluation of its results. Mixtures of CF_4 and O_2 will aldo be studied in future works due to the importance of CF_4/O_2 plasmas for etching processes.

It is hoped that this study may shine a light on the role of the singlet metastable

molecules and the energy distribution functions for electrons and ions in the oxygen discharge. It can also serve as a guide when selecting reactions in computationally intensive models of the oxygen discharges.

Bibliography

[1] LANGMUIR, I. Oscillations in ionized gases. **Proc. Natl. Acad. Sci.**, v. 14, p. 627–637, 1928.

[2] TONKS, L. The birth of "plasma". **Am. J. Phys.**, v. 35, p. 857–858, 1967.

[3] MOTT-SMITH, H. M. History of "plasmas". **Nature**, v. 233, p. 219, 1971.

[4] CROOKES, W. On radiant matter. **J. Franklin Inst.**, v. 108, p. 305–316, 1879.

[5] BURM, K. T. A. L. Plasma: The fourth state of matter. **Plasma Chem. Plasma Process.**, v. 32, p. 401–407, 2012.

[6] CHEN, F. F. **Introduction to Plasma Physics and Controlled Fusion**. New York: Spring US, 2010. 421 p.

[7] OSAKA, Y. et al. Measurement of plasma properties of the atmospheric oxy-combustion flame by using double probe method. **Contrib. Plasma Phys.**, v. 48, p. 485–490, 2008.

[8] VON ENGEL, A.; COZENS, J. R. Flame plasmas. **Adv. Electron. El. Phys.**, v. 20, p. 99–146, 1965.

[9] SARANTARIDIS, D.; FOWOWE, T.; CARUANA, D. J. Electrochemistry in flames. **Sci. Prog.**, v. 93, p. 301–317, 2010.

[10] IKEYA, M.; MATSUMOTO, H. Reproduced earthquake precursor legends using a van de graaff electrostatic generator: Candle flame and dropped nails. **Naturwissenschaften**, v. 84, p. 539–541, 1997.

[11] NAULIN, V.; JACQUEMOT, S. 40th european physical society conference on plasma physics. **Plasma Phys. Control. Fusion**, v. 55, p. 120301, 2013.

[12] HUANG, H.; TANG, L. Treatment of organic waste using thermal plasma pyrolysis technology. **Energ. Convers. Manage.**, v. 48, p. 1331–1337, 2007.

[13] MEICHSNER, J. Low temperature plasmas. In: **Plasma Physics**. Heidelberg: Springer, 2005. p. 95–116.

[14] CHU, P. K.; LU, X. **Low temperature plasma technology**. New York: CRC Press, 2013. 493 p.

[15] BOULOS, M. I.; FAUCHAIS, P.; PFENDER, E. **Thermal Plasmas**. New York: Springer Science & Business Media, 1994. 452 p.

[16] BOSCARIOL, M. R. et al. Sterilization by pure oxygen plasma and by oxygen–hydrogen peroxide plasma: An efficacy study. **Int. J. Pharm.**, v. 353, p. 170–175, 2008.

[17] GRAVES, D. B. The emerging role of reactive oxygen and nitrogen species in redox biology and some implications for plasma applications to medicine and biology. **J. Phys. D: Appl. Phys.**, v. 45, p. 263001, 2012.

[18] LODIN, V. J. et al. Investigations of processes in a glow electrical discharge singlet-oxygen generator for oxygen-iodine laser. In: **Proceedings of SPIE – XV International Symposium on Gas Flow, Chemical Lasers, and High-Power Lasers**. Prague: SPIE, 2005. v. 5777, p. 221–225.

[19] TOLLIVER, D. L. The history of plasma processing. In: EINSPRUCH, N. G.; BROWN, D. M. (Ed.). **VLSI Electronics: Microstructure Science**. Orlando: Academic Press, 1984. p. 1–24.

[20] HARTNEY, M. A.; HESS, D. W.; SOANE, D. S. Oxygen plasma etching for resist stripping and multilayer lithography. **J. Vac. Sci. Technol. B**, v. 7, p. 1–13, 1989.

[21] CARL, D. A.; HESS, D. W.; LIEBERMAN, M. A. Kinetics of photoresist etching in an electron cyclotron resonance plasma. **J. Appl. Phys.**, v. 68, p. 1859–1865, 1990.

[22] LEE, H.-C.; CHUNG, C.-W. Electron heating and control of electron energy distribution for the enhancement of the plasma ashing processing. **Plasma Sources Sci. Technol.**, v. 24, p. 024001, 2015.

[23] GRACE, J. M.; GERENSER, L. J. Plasma treatment of polymers. **J. Disp. Sci. Technol.**, v. 24, p. 305–341, 2003.

[24] VESEL, A.; MOZETIC, M. Surface modification and ageing of pmma polymer by oxygen plasma treatment. **Vacuum**, v. 86, p. 634–637, 2012.

[25] CARL, D. A. et al. Effects of dc bias on the kinetics and electrical properties of silicon dioxide grown in an electron cyclotron resonance plasma. **J. Appl. Phys.**, v. 70, p. 3301–3313, 1991.

[26] AGNARSSON, B. et al. Rutile TiO_2 thin films grown by reactive high power impulse magnetron sputtering. **Thin Solid Films**, v. 545, p. 445–450, 2013.

[27] LIEBERMAN, M. A.; GOTTSCHO, R. A. Design of high-density plasma sources for materials processing. In: FRANCOMBE, M. H.; VOSSEN, J. L. (Ed.). **Plasma Sources for Thin Film Deposition and Etching**. San Diego: Academic Press, 1994. p. 1–119.

[28] LEE, C. et al. Global model of plasma chemistry in a high density oxygen discharge. **J. Electrochem. Soc.**, v. 141, p. 1546–1555, 1994.

[29] LEE, C.; LIEBERMAN, M. A. Global model of Ar, O_2, Cl_2, and Ar/O_2 high-density plasma discharges. **J. Vac. Sci. Technol.**, v. 13, p. 368–380, 1995.

[30] KIMURA, T.; OHE, K. Probe measurements and global model of inductively coupled Ar/CF4 discharges. **Plasma Sources Sci. Technol.**, v. 8, p. 553–560, 1999.

[31] ELIASSON, B.; KOGELSCHATZ, U. **Basic data for modelling of electrical discharges in gases**. Baden: Brown Boveri Konzernforschung, 1986. 148 p.

[32] KOSSYI, I. et al. Kinetic scheme of the non-equilibrium discharge in nitrogen-oxygen mixtures. **Plasma Sources Sci. Technol.**, v. 1, p. 207–220, 1992.

[33] ITIKAWA, Y. Cross sections for electron collisions with oxygen molecules. **J. Phys. Chem. Ref. Data**, v. 38, p. 1–20, 2009.

[34] ITIKAWA, Y.; ICHIMURA, A. Cross sections for collisions of electrons and photons with atomic oxygen. **J. Phys. Chem. Ref. Data**, v. 19, p. 637–651, 1990.

[35] BAULCH, D. L. et al. Evaluated kinetic and photochemical data for atmospheric chemistry: Supplement i codata task group on chemical kinetics. **J. Phys. Chem. Ref. Data**, v. 11, p. 327–496, 1982.

[36] KIM, S. **An Improved Global Model for Electronegative Discharge and Ignition Conditions for Peripheral Plasma Connected to a Capacitive Discharge**. Tese (Doutorado) — Berkeley: University of California, 2006.

[37] KIM, S. et al. Improved volume-averaged model for steady and pulsed-power electronegative discharges. **J. Vac. Sci. Technol. A**, v. 26, p. 2025–2040, 2006.

[38] THOMPSON, J. B. The ion balance of the oxygen dc glow discharge. **Proc. R. Soc. Lond. A**, v. 262, p. 503–518, 1961.

[39] BARNES, M. S.; FORSTER, J. C.; KELLER, J. H. Electron energy distribution function measurements in a planar inductive oxygen radio frequency glow discharge. **Appl. Phys. Lett.**, v. 62, p. 2622–2624, 1993.

[40] GUDMUNDSSON, J. T. et al. On the plasma parameters of a planar inductive oxygen discharge. **J. Phys. D: Appl. Phys.**, v. 33, p. 1323–1331, 2000.

[41] FULLER, N. C. et al. Characterization of transformer coupled oxygen plasmas by trace rare gases-optical emission spectroscopy and langmuir probe analysis. **Plasma Sources Sci. Technol.**, v. 9, p. 116–127, 2000.

[42] CORR, C. S.; GOMEZ, S.; GRAHAM, W. G. Discharge kinetics of inductively coupled oxygen plasmas: experiment and model. **Plasma Sources Sci. Technol.**, v. 21, p. 055024, 2012.

[43] KIEHLBAUCH, M. W.; GRAVES, D. B. Inductively coupled plasmas in oxygen: Modeling and experiment. **J. Vac. Sci. Technol. A**, v. 21, p. 660–670, 2003.

[44] GUDMUNDSSON, J. T. Recombination and detachment in oxygen discharges: the role of metastable oxygen molecules. **J. Phys. D: Appl. Phys.**, v. 37, p. 2073–2081, 2004.

[45] MONAHAN, D. D.; TURNER, M. M. Global models of electronegative discharges: critical evaluation and practical recommendations. **Plasma Sources Sci. Technol.**, v. 17, p. 045003, 2008.

[46] GUDMUNDSSON, J. T.; LIEBERMAN, M. A. Model and measurements for a planar inductive oxygen discharge. **Plasma Sources Sci. Technol.**, v. 7, p. 1–12, 1998.

[47] GUDMUNDSSON, J. T. On the effect of the electron energy distribution on the plasma parameters of an argon discharge: a global (volume-averaged) model study. **Plasma Sources Sci. Technol.**, v. 10, p. 76–81, 2001.

[48] THORSTEINSSON, E. G.; GUDMUNDSSON, J. T. A global (volume averaged) model of a nitrogen discharge: I. steady state. **Plasma Sources Sci. Technol.**, v. 18, p. 045001, 2009.

[49] THORSTEINSSON, E. G.; GUDMUNDSSON, J. T. A global (volume averaged) model of a chlorine discharge. **Plasma Sources Sci. Technol.**, v. 19, p. 015001, 2009.

[50] GUDMUNDSSON, J. T.; HJARTARSON, A. T.; THORSTEINSSON, E. G. The influence of the electron energy distribution on the low pressure chlorine discharge. **Vacuum**, v. 86, p. 808–812, 2012.

[51] KOKURA, H.; SUGAI, H. Dependence of fluorocarbon plasma chemistry on the electron energy distribution function. **Jpn. J. Appl. Phys.**, v. 39, p. 2847–2853, 2000.

[52] TONELI, D. A. et al. On the formation and annihilation of the singlet molecular metastables in an oxygen discharge. **J. Phys. D: Appl. Phys.**, v. 48, p. 325202, 2015.

[53] TONELI, D. A. et al. A volume averaged global model study of the influence of the electron energy distribution and the wall material on an oxygen discharge. **J. Phys. D: Appl. Phys.**, v. 48, p. 495203, 2015.

[54] LEE, D.; HERSHKOWITZ, N.; SEVERN, G. D. Measurements of Ar^+ and Xe^+ velocities near the sheath boundary of Ar–Xe plasma using two diode lasers. **Appl. Phys. Lett.**, v. 91, p. 041505, 2007.

[55] YIP, C. -S. et al. Laser-induced fluorescence measurements of argon and xenon ion velocities near the sheath boundary in 3 ion species plasmas. **Phys. Plasmas**, v. 23, p. 050703, 2016.

[56] SOBOLOEWSKI, M. A.; YICHENG, W.; GOYETTE, A. Ion velocities in the presheath of electronegative, radio-frequency plasmas measured by low-energy cutoff. **Appl. Phys. Lett.**, v. 109, p. 024105, 2016.

[57] CHAPMAN, B. **Glow Discharge Processes**. New York: John Wiley & Sons, 1980. 406 p.

[58] HERBERT, C. G.; JOHNSTONE, R. A. W. **Mass spectrometry basics**. New York: CRC press, 2002. 474 p.

[59] LIEBERMAN, M. A.; LICHTENBERG, A. J. **Principles of plasma discharges and materials processing**. New Jersey: John Wiley & Sons, 2005. 730 p.

[60] CHABERT, P.; BRAITHWAITE, N. **Physics of radio-frequency plasmas**. New York: Cambridge University Press, 2011. 385 p.

[61] HOPWOOD, J. Planar rf induction plasma coupling efficiency. **Plasma Sources Sci. Technol.**, v. 3, p. 460–464, 1994.

[62] HOPWOOD, J. Review of inductively coupled plasmas for plasma processing. **Plasma Sources Sci. Technol.**, v. 1, p. 109–116, 1992.

[63] HOPWOOD, J. et al. Electromagnetic fields in a radio-frequency induction plasma. **J. Vac. Sci. Technol. A**, v. 11, p. 147–151, 1993.

[64] TENDERO, C. et al. Atmospheric pressure plasmas: A review. **Spectrochim. Acta, Part B**, v. 61, p. 2–30, 2006.

[65] DE TOLEDO PIZA, A. F. R. **Mecânica quântica**. São Paulo: Edusp, 2003. 605 p.

[66] ELLIS, A. M.; FEHER, M.; WRIGHT, T. G. **Electronic and photoelectron spectroscopy: fundamentals and case studies**. New York: Cambridge University Press, 2005. 286 p.

[67] DE GRAAF, C.; BROER, R. **Magnetic interactions in molecules and solids**. Switzerland: Springer, 2016. 246 p.

[68] BARYSZ, M.; ISHIKAWA, Y. **Relativistic methods for chemists**. New York: Springer Science & Business Media, 2010. 613 p.

[69] TENNYSON, J. **Astronomical spectroscopy**. London: World Scientific, 2010. 223 p.

[70] HOLLAS, J. M. **Modern spectroscopy**. Chichester: John Wiley & Sons, 2004. 480 p.

[71] STRUVE, W. S. **Fundamentals of molecular spectroscopy**. New York: Wiley, 1989. 299 p.

[72] WAYNE, R. P. Singlet molecular oxygen. In: PITTS JR., J. N.; HAMMOND, G. S.; NOYES JR., W. A. (Ed.). **Advances in Photochemistry**. New Jersey: John Wiley & Sons, Inc., 1969. p. 311–371.

[73] ZHANG, S. et al. Spatially resolved ozone densities and gas temperatures in a time modulated RF driven atmospheric pressure plasma jet: an analysis of the production and destruction mechanisms. **J. Phys. D: Appl. Phys.**, v. 46, p. 205202, 2013.

[74] GRAVES, D. B. Low temperature plasma biomedicine: A tutorial review. **Phys. Plasmas**, v. 21, p. 080901, 2014.

[75] IZOD, T. P. J.; WAYNE, R. P. The formation, reaction and deactivation of $O_2(^1\Sigma_g^+)$. **Proc. Roy. Soc. A**, v. 308, p. 81–94, 1968.

[76] O'BRIEN, R. J.; MYERS, G. H. Direct flow measurement of $O_2(b^1\Sigma_g^+)$ quenching rates. **J. Chem. Phys.**, v. 53, p. 3832–3835, 1970.

[77] BURROW, P. D. Dissociative attachment from the $O_2(a^1\Delta_g)$ state. **J. Chem. Phys.**, v. 59, p. 4922–4931, 1973.

[78] VIDAUD, P. H.; WAYNE, R. P.; YARON, M. Diffusion coefficient measurement of $O_2^*(^1\Delta_g)$ in ground state O_2. **Chem. Phys. Lett.**, v. 38, p. 306–309, 1976.

[79] THORSTEINSSON, E. G.; GUDMUNDSSON, J. T. The low pressure Cl_2/O_2 discharge and the role of ClO. **Plasma Sources Sci. Technol.**, v. 19, p. 055008, 2010.

[80] SIEGEL, M. W. Cross sections for production of O_3^+, O_2^+ and O^+ by electron impact ionization of ozone between threshold and 100 eV. **Int. J. Mass Spectrom. Ion Physics**, v. 44, p. 19–36, 1982.

[81] GUDMUNDSSON, J. T. **A critical review of the reaction set for a low pressure oxygen processing discharge**. Technical Report RH-17-2004. Reykjavik: University of Iceland, 2004.

[82] LINDSAY, B. G.; MANGAN, M. A. Ionization. In: ITIKAWA, Y. (Ed.). **Interactions of Photons and Electrons with Molecules**. Heidelberg: Springer, 2003. p. 5001–5077.

[83] KRISHNAKUMAR, E.; SRIVASTAVA, S. K. Cross-sections for electron impact ionization of O_2. **Int. J. Mass Spectrom. Ion Proc.**, v. 113, p. 1–12, 1992.

[84] PHELPS, A. V. **Tabulations of Collision Cross Sections and Calculated Transport and Reaction Coefficients for Electron Collisions with O_2**. JILA Information Center Report, 1985.

[85] RAPP, D.; BRIGLIA, D. D. Total cross sections for ionization and attachment in gases by electron impact. ii. negative-ion formation. **J. Chem. Phys.**, v. 43, p. 1480–1489, 1995.

[86] HAYASHI, D.; KADOTA, K. Efficient production of O^- by dissociative attachment of slow electrons to highly excited metastable oxygen molecules. **Jpn. J. Appl. Phys.**, v. 37, p. 225–230, 1999.

[87] CHERKANI-HASSANI, H. et al. Absolute cross sections for electron impact ionization and dissociation of O_2^+. **J. Phys. B: At. Mol. Opt. Phys.**, v. 39, p. 5105–5117, 2006.

[88] PEVERALL, R. et al. Dissociative recombination and excitation of O-2(+): Cross sections, product yields and implications for studies of ionospheric airglows. **J. Chem. Phys.**, v. 114, p. 6679–6689, 2001.

[89] TRAJMAR, S.; CARTWRIGHT, D. C.; WILLIAMS, W. Differential and integral cross sections for the electron-impact excitation of the a1Δg and b1Σg states of O_2. **Phys. Rev. A**, v. 4, p. 1482–1492, 1971.

[90] KIM, Y.-K.; DESCLAUX, J.-P. Ionization of carbon, nitrogen, and oxygen by electron impact. **Phys. Rev. A**, v. 66, p. 012708, 2002.

[91] LAHER, R. R.; GILMORE, F. R. Updated excitation and ionization cross sections for electron impact on atomic oxygen. **J. Phys. Chem. Ref. Data**, v. 19, p. 277–305, 1990.

[92] VEJBY-CHRISTENSEN, L. et al. Electron-impact detachment from negative ions. **Phys. Rev. A**, v. 53, p. 2371–2378, 1996.

[93] JAFFKE, T. et al. Dissociative electron attachment to singlet oxygen. **Chem. Phys. Lett.**, v. 193, p. 62–68, 1992.

[94] JOHNSTON, H. S. **Gas phase reaction kinetics of neutral oxygen species**. NSRDS-NBS 20. Berkeley: University of California, 1968.

[95] BAEVA, M. et al. Experimental investigation and modelling of a low-pressure pulsed microwave discharge in oxygen. **Plasma Sources Sci. Technol.**, v. 9, p. 128–145, 2000.

[96] STAFFORD, D. S.; KUSHNER, M. J. $O_2(^1\Delta)$ production in He/O_2 mixtures in flowing low pressure plasmas. **J. Appl. Phys.**, v. 96, p. 2451–2465, 2004.

[97] BORRELL, P. M. et al. Rate constants for the energy-pooling and-quenching reactions of singlet molecular oxygen at high temperatures. **J. Phys. Chem.**, v. 86, p. 700–703, 1982.

[98] KENNER, R. D.; OGRYZLO, E. A. Deactivation of O_2 $(A^3\Sigma_u^+)$ by O_2, O, and Ar. **I. J. Chem. Kinet.**, v. 12, p. 501–508, 1980.

[99] JEONG, J. Y. et al. Reaction chemistry in the afterglow of an oxygen-helium, atmospheric-pressure plasma. **J. Phys. Chem. A**, v. 104, p. 8027–8032, 2000.

[100] DETTMER, J. W. **Discharge processes in the oxygen plasma**. Wright-Patterson AFB, 1981. ADA100653.

[101] COHEN, N.; WESTBERG, K. R. Chemical kinetic data sheets for high-temperature chemical reactions. **J. Phys. Chem. Ref. Data**, v. 12, p. 531–591, 1983.

[102] BORRELL, P.; RICH, N. H. The rate constant for the "dimol" transition of singlet oxygen, $O_2(a^1\Delta_g)$, and the likely symmetry of the emitting species. **Chem. Phys. Lett.**, v. 99, p. 144–147, 1983.

[103] JACOBS, H. et al. Reaction kinetics and chemical quasi-equilibria of the ozone synthesis in oxygen DC discharges. **Contrib. Plasma Phys.**, v. 36, p. 471–486, 1996.

[104] CLARK, I. D.; WAYNE, R. P. The reaction of $O_2(^1\Delta_g)$ with atomic nitrogen and with atomic oxygen. **Chem. Phys. Lett.**, v. 3, p. 405–407, 1969.

[105] SLANGER, T. G.; BLACK, G. Interactions of $O_2(b^1\Sigma_g^+)$ with $O(^3P)$ and O_3. **J. Chem. Phys.**, v. 70, p. 3434–3438, 1979.

[106] VASILJEVA, A. N. et al. On the possibility of $O_2(a^1\Delta_g)$ production by a non-self-sustained discharge for oxygen-iodine laser pumping. **J. Phys. D: Appl. Phys.**, v. 37, p. 2455–2468, 2004.

[107] ABREU, V. J. et al. The quenching rate of $O(^1D)$ by $O(^3P)$. **Planet. Space Sci.**, v. 34, p. 1143–1145, 1986.

[108] WILLIAMS, S. et al. Negative ion chemistry of ozone in the gas phase. **J. Phys. Chem. A**, v. 106, p. 997–1003, 2002.

[109] FEHSENFELD, F. C. et al. Associative-detachment reactions of O^- and $O_2{}^-$ by $O_2(^1\Delta_g)$. **Can. J. Chem.**, v. 47, p. 1793–1795, 1969.

[110] POUTSMA, J. C.; MIDEY, A. J.; VIGGIANO, A. A. Absolute rate coefficients for the reactions of O_2^-+N($^4S_{3/2}$) and O_2^-+ O(^{3}P) at 298 k in a selected-ion flow tube instrument. **J. Chem. Phys.**, v. 124, p. 074301, 2006.

[111] PANCHESHNYI, S. Effective ionization rate in nitrogen-oxygen mixtures. **J. Phys. D: Appl. Phys.**, v. 46, p. 155201, 2013.

[112] BELOSTOTSKY, S. G. et al. Negative ion destruction by O(^{3}P) atoms and $O_2(a^1\Delta_g)$ molecules in an oxygen plasma. **Plasma Sources Sci. Technol.**, v. 14, p. 532–542, 2005.

[113] ALEKSANDROV, N. L. Electron detachment from O^- and O_2^- ions in excited molecules in an air discharge. **Sov. Phys. Tech. Phys.**, v. 23, p. 806–808, 1978.

[114] GUDMUNDSSON, J. T.; LIEBERMAN, M. A. **Recombination rate coefficients in oxygen discharges**. Technical Report RH-16-2004. Reykjavik: University of Iceland, 2004.

[115] GORDIETS, B. F. et al. Self-consistent kinetic model of low-pressure-flowing discharges: I. volume processes. **IEEE Trans. Plasma Sci.**, v. 23, p. 750–768, 1995.

[116] MARTIN, L. R.; COHEN, R. B.; SCHATZ, J. F. Quenching of laser induced fluorescence of $O_2(b^1\Sigma_g^+)$ by O_2 and N_2. **Chem. Phys. Lett.**, v. 41, p. 394–396, 1976.

[117] LAWTON, S. A. et al. Quenching of optically pumped $O_2(b^1\Sigma_g^+)$ by ground state O_2 molecules. **J. Chem. Phys.**, v. 66, p. 1381–1382, 1977.

[118] SHUMAN, N. S. et al. Kinetics of ion-ion mutual neutralization: Halide anions with polyatomic cations. **J. Chem. Phys.**, v. 140, p. 224309, 2014.

[119] KENNER, R. D.; OGRYZLO, E. A. Rate constant for the deactivation of $O_2(A^3\Sigma_u^+)$ by N_2. **Chem. Phys. Lett.**, v. 103, p. 209–212, 1983.

[120] NEWMAN, S. M. et al. Temperature and pressure dependence of line widths and integrated absorption intensities for the O_2 $a^1\Delta_g$–$X^3\Sigma_g^-$ (0,0) transition. **J. Chem. Phys. A**, v. 104, p. 9467–9480, 2000.

[121] SCHWEITZER, C.; SCHMIDT, R. Physical mechanisms of generation and deactivation of singlet oxygen. **Chem. Rev.**, v. 103, p. 1685–1757, 2003.

[122] GUDMUNDSSON, J. T.; THORSTEINSSON, E. G. Oxygen discharges diluted with argon: dissociation processes. **Plasma Sources Sci. Technol.**, v. 16, p. 399–412, 2007.

[123] SHARPLESS, R. L.; SLANGER, T. G. Surface chemistry of metastable oxygen. II. destruction of $O_2(a^1\Delta_g)$. **J. Chem. Phys.**, v. 91, p. 7947–7950, 1989.

[124] HICKMAN, A. P. et al. Fine structure effects in the O^+–O collision frequency. **Geophys. Res. Lett.**, v. 24, p. 119–122, 1997.

[125] GUHA, J. et al. In-situ surface recombination measurements of oxygen atoms on anodized aluminum in an oxygen plasma. **J. Phys. Chem. C**, v. 112, p. 8963–8968, 2008.

[126] DU, S. et al. $O_2(^1\Delta_g)$ deactivation on O2-adsorbed metal surfaces. **Chin. J. Chem. Phys.**, v. 24, p. 256–260, 2011.

[127] BIRDSALL, C. K.; LANGDON, A. B. **Plasma Physics Via Computer**. New York: CRC Press, 2004. 504 p.

[128] CASAS-VÁZQUEZ, J.; JOU, D. Temperature in non-equilibrium states: a review of open problems and current proposals. **Rep. Prog. Phys.**, v. 66, p. 1937–2023, 2003.

[129] BOYD, R. L. F.; THOMPSON, J. B. The operation of langmuir probes in electro-negative plasmas. **Proc. R. Soc.**, v. 252, p. 102–119, 1959.

[130] SINGH, H.; GRAVES, D. B. Measurements of the electron energy distribution function in molecular gases in an inductively coupled plasma. **J. Appl. Phys.**, v. 87, p. 4098–4106, 2000.

[131] SEO, D. C. et al. Electrostatic probe diagnostics of a planar-type radio-frequency inductively coupled oxygen plasma. **J. Appl. Phys.**, v. 89, p. 4218–4223, 2001.

[132] CHUNG, T. H.; SHIN, Y. M.; SEO, D. C. Comparison of two methods of interpretation of langmuirprobe data for an inductively coupled oxygen plasma. **Contrib. Plasma Phys.**, v. 46, p. 348–353, 2006.

[133] LEE, M.-H.; LEE, H.-C.; CHUNG, C.-W. Comparison of pressure dependence of electron energy distributions in oxygen capacitively and inductively coupled plasmas. **Phys. Rev. E**, v. 81, p. 046402, 2010.

[134] STREIT, G. E. et al. Temperature dependence of $O(^1D)$ rate constants for reactions with O_2, N_2, CO_2, O_3, and H_2O. **J. Chem. Phys.**, v. 65, p. 4761–4764, 1976.

[135] AMIMOTO, S. T. et al. Collisional deactivation of $O(2^1D_2)$ by the atmospheric gases. **J. Chem. Phys.**, v. 71, p. 3640–3647, 1979.

[136] DEMORE, W. B.; RAPER, O. F. Deactivation of $O(^1D)$ in the atmosphere. **Astrophys. J.**, v. 139, p. 1381–1383, 1964.

[137] STOFFELS, E. et al. Negative ions in a radio-frequency oxygen plasma. **Phys. Rev. E**, v. 51, p. 2425–2435, 1995.

[138] IVANOV, V. V. et al. Experimental and theoretical investigation of oxygen glow discharge structure at low pressures. **IEEE Trans. Plasma Sci.**, v. 27, p. 1279–1287, 1999.

[139] FRANKLIN, R. N. Is oxygen a detachment-dominated gas or not? **J. Phys. D: Appl. Phys.**, v. 33, p. 3009, 2000.

[140] GUDMUNDSSON, J. T. et al. A reply to a comment on:on the plasma parameters of a planar inductive oxygen discharge. **J. Phys. D: Appl. Phys.**, v. 33, p. 3010–3012, 2000.

[141] FRANKLIN, R. N. The role of $O_2(a^1\Delta_g)$ metastables and associative detachment in discharges in oxygen. **J. Phys. D: Appl. Phys.**, v. 34, p. 1834–1839, 2001.

[142] GUDMUNDSSON, J. T.; LIEBERMAN, M. A. On the role of metastables in capacitively coupled oxygen discharges. **Plasma Sources Sci. Technol.**, v. 24, p. 035016, 2015.

[143] LEE, J. -B. et al. Time evolution of electronegativity in a pulsed inductively coupled oxygen plasma. **Thin Solid Films**, v. 518, p. 6573–6577, 2010.

[144] BOHM, D. Minimum ionic kinetic energy for a stable sheath. In: GUTHRIE, A.; WAKERLING, R. K. (Ed.). **The Characteristics of Electrical Discharges in Magnetic Fields**. New York: McGraw-Hill, 1949. p. 77–86.

[145] RIEMANN, K.-U. The influence of collisions on the plasma sheath transition. **Phys. Plasmas**, v. 4, p. 4158–4166, 1997.

[146] OKSUZ, L.; HERSHKOWITZ, N. First experimental measurements of the plasma potential throughout the presheath and sheath at a boundary in a weakly collisional plasma. **Phys. Rev. Lett.**, v. 89, p. 145001, 2002.

[147] ALLEN, J. E. A note on the generalized sheath criterion. **J. Phys. D: Appl. Phys.**, v. 9, p. 2331, 1976.

[148] AMEMIYA, H. Sheath formation criterion and ion flux for non-maxwellian plasma. **J. Phys. Soc. Jpn.**, v. 66, p. 1335–1338, 1997.

[149] AMEMIYA, H. Sheath formation criterion and ion flux for a non-maxwellian plasma containing negative ions. **J. Phys. Soc. Jpn.**, v. 67, p. 1955–1962, 1998.

[150] BAALRUD, S. D.; HEGNA, C. C.; CALLEN, J. D. Instability-enhanced collisional friction can determine the bohm criterion in multiple-ion-species plasmas. **Phys. Rev. Lett.**, v. 103, p. 205002, 2009.

[151] GUDMUNDSSON, J. T.; LIEBERMAN, M. A. Ar^+ and Xe^+ velocities near the presheath-sheath boundary in an Ar/Xe discharge. **Phys. Rev. Lett.**, v. 107, p. 045002, 2011.

[152] HERSHKOWITZ, N.; SEVERN, G. D.; BAALRUD, S. D. Comment on "Ar^+ and Xe^+ velocities near the presheath-sheath boundary in an Ar/Xe discharge". **Phys. Rev. Lett.**, v. 108, p. 139501, 2012.

[153] RIEMANN, K. -U. Kinetic theory of the plasma sheath transition in a weakly ionized plasma. **Phys. Fluids**, v. 24, p. 2163–2172, 1981.

[154] RIEMANN, K.-U. The bohm criterion and sheath formation. **J. Phys. D: Appl. Phys.**, v. 24, p. 493–518, 1991.

[155] BAALRUD, S. D.; HEGNA, C. C. Kinetic theory of the presheath and the bohm criterion. **Plasma Sources Sci. Technol.**, v. 20, p. 025013, 2011.

[156] RIEMANN, K.-U. Comment on 'kinetic theory of the presheath and the bohm criterion'. **Plasma Sources Sci. Technol.**, v. 21, p. 068001, 2012.

[157] BAALRUD, S. D.; HEGNA, C. C. Reply to comment on 'Kinetic theory of the presheath and the Bohm criterion'. **Plasma Sources Sci. Technol.**, v. 21, p. 068002, 2012.

[158] SINGH, H.; COBURN, J. W.; GRAVES, D. B. Measurements of neutral and ion composition, neutral temperature, and electron energy distribution function in a CF_4 inductively coupled plasma. **J. Vac. Sci. Technol. A**, v. 19, p. 718–729, 2001.

Annex A - Cross sections

Reaction 1		**Reaction 2**		**Reaction 3**	
Energy [eV]	$\sigma \times 10^{-20}$ [m^{-3}]	Energy [eV]	$\sigma \times 10^{-20}$ [m^{-3}]	Energy [eV]	$\sigma \times 10^{-20}$ [m^{-3}]
12.67	0.000	13.14	0.0000		
20.00	0.179	20.00	0.0741	18.35	0.0000
30.00	0.636	30.00	0.4880	30.00	0.0508
40.00	0.888	40.00	0.7110	40.00	0.1400
50.00	1.000	50.00	0.8420	50.00	0.2050
60.00	1.070	60.00	0.9170	60.00	0.3080
70.00	1.110	70.00	0.9580	70.00	0.3080
80.00	1.120	80.00	0.9680	80.00	0.3380
90.00	1.100	90.00	0.9780	90.00	0.3610
100.00	1.060	100.00	0.9940	100.00	0.3800

Reaction 4					
Energy [eV]	$\sigma \times 10^{-22}$ [m^{-3}]	Energy [eV]	$\sigma \times 10^{-22}$ [m^{-3}]	Energy [eV]	$\sigma \times 10^{-22}$ [m^{-3}]
0.0	8.06	3.4	7.85	6.8	3.72
0.1	7.50	3.5	7.66	6.9	4.36
0.2	6.92	3.6	6.86	7.0	4.98
0.3	8.20	3.7	6.62	7.1	5.56
0.4	10.01	3.8	6.12	7.2	5.71
0.5	11.94	3.9	6.29	7.3	6.01
0.6	14.69	4.0	5.53	7.4	6.31
0.7	18.70	4.1	4.62	7.5	5.71
0.8	20.87	4.2	4.00	7.6	6.08
0.9	24.88	4.3	3.85	7.7	5.86
1.0	28.24	4.4	2.84	7.8	5.03
1.1	31.58	4.5	2.77	7.9	5.35
1.2	36.21	4.6	2.34	8.0	5.30
1.3	37.03	4.7	2.10	8.1	4.07
1.4	37.21	4.8	2.00	8.2	3.89
1.5	36.47	4.9	1.77	8.3	3.58
1.6	34.67	5.0	1.08	8.4	2.58
1.7	31.29	5.1	1.31	8.5	2.46
1.8	27.97	5.2	1.03	8.6	1.81
1.9	23.78	5.3	0.72	8.7	1.37
2.0	21.11	5.4	0.59	8.8	1.35
2.1	19.05	5.5	0.76	8.9	1.01
2.2	15.99	5.6	1.06	9.0	0.79
2.3	13.30	5.7	1.27	9.1	0.60
2.4	11.51	5.8	1.39	9.2	0.43
2.5	11.25	5.9	1.37	9.3	0.38
2.6	9.59	6.0	1.67	9.4	0.31
2.7	8.93	6.1	1.82	9.5	0.19
2.8	8.63	6.2	2.12	9.6	0.42
2.9	9.18	6.3	2.31	9.7	0.31
3.0	8.47	6.4	2.56	9.8	0.19
3.1	8.94	6.5	2.79	9.9	0.16
3.2	8.25	6.6	3.07	10.0	0.17
3.3	8.20	6.7	3.92		

Reaction 5					
Energy [eV]	$\sigma \times 10^{-22}$ [m^{-3}]	Energy [eV]	$\sigma \times 10^{-22}$ [m^{-3}]	Energy [eV]	$\sigma \times 10^{-22}$ [m^{-3}]
0.0	2.00	3.4	0.21	6.8	0.32
0.1	2.22	3.5	0.20	6.9	0.33
0.2	1.80	3.6	0.20	7.0	0.34
0.3	2.00	3.7	0.19	7.1	0.34
0.4	2.16	3.8	0.18	7.2	0.34
0.5	3.06	3.9	0.18	7.3	0.33
0.6	4.02	4.0	0.17	7.4	0.33
0.7	6.24	4.1	0.16	7.5	0.32
0.8	8.64	4.2	0.16	7.6	0.31
0.9	11.88	4.3	0.16	7.7	0.30
1.0	13.26	4.4	0.16	7.8	0.29
1.1	15.00	4.5	0.15	7.9	0.29
1.2	16.80	4.6	0.14	8.0	0.26
1.3	15.48	4.7	0.14	8.1	0.25
1.4	14.16	4.8	0.14	8.2	0.23
1.5	11.52	4.9	0.14	8.3	0.22
1.6	9.30	5.0	0.14	8.4	0.20
1.7	6.96	5.1	0.14	8.5	0.18
1.8	4.68	5.2	0.14	8.6	0.16
1.9	3.96	5.3	0.15	8.7	0.14
2.0	2.28	5.4	0.16	8.8	0.13
2.1	1.86	5.5	0.17	8.9	0.11
2.2	1.56	5.6	0.17	9.0	0.10
2.3	1.20	5.7	0.19	9.1	0.08
2.4	0.60	5.8	0.20	9.2	0.07
2.5	0.69	5.9	0.21	9.3	0.06
2.6	0.30	6.0	0.22	9.4	0.06
2.7	0.24	6.1	0.24	9.5	0.05
2.8	0.24	6.2	0.25	9.6	0.05
2.9	0.18	6.3	0.27	9.7	0.05
3.0	0.18	6.4	0.28	9.8	0.05
3.1	0.18	6.5	0.30	9.9	0.04
3.2	0.19	6.6	0.31	10.0	0.04
3.3	0.20	6.7	0.32		

Reaction 6					
Energy [eV]	$\sigma \times 10^{-20}$ [m^{-3}]	Energy [eV]	$\sigma \times 10^{-20}$ [m^{-3}]	Energy [eV]	$\sigma \times 10^{-20}$ [m^{-3}]
1	5.97	12	9.00	100	4.78
2	6.45	15	8.89	200	3.15
3	6.74	20	8.60	300	2.40
4	6.93	30	8.09	400	2.00
5	7.20	40	7.30	500	1.72
6	7.52	50	6.59	600	1.53
7	7.86	60	6.08	700	1.37
8	8.21	70	5.63	800	1.27
9	8.49	80	5.29	900	1.18
10	8.80	90	5.01	1000	1.10

Reaction 7					
Energy [eV]	$\sigma \times 10^{-22}$ [m^{-3}]	Energy [eV]	$\sigma \times 10^{-22}$ [m^{-3}]	Energy [eV]	$\sigma \times 10^{-22}$ [m^{-3}]
13.0	2.0	90.0	187.9	220.0	165.0
14.0	4.1	95.0	190.5	230.0	162.8
15.0	6.5	100.0	192.3	240.0	159.8
16.0	10.9	105.0	193.3	250.0	156.9
17.0	15.8	110.0	193.4	260.0	154.7
18.0	20.3	115.0	193.3	270.0	152.0
19.0	24.6	120.0	192.8	280.0	149.4
20.0	28.8	125.0	192.0	290.0	147.3
22.5	42.0	130.0	190.8	300.0	145.6
25.0	51.9	135.0	189.6	350.0	135.5
27.5	61.8	140.0	188.2	400.0	126.2
30.0	69.3	145.0	186.6	450.0	118.8
32.5	77.2	150.0	185.3	500.0	111.2
35.0	86.1	155.0	184.1	550.0	105.8

Reaction 7 (*continued*)					
Energy [eV]	$\sigma \times 10^{-22}$ [m^{-3}]	Energy [eV]	$\sigma \times 10^{-22}$ [m^{-3}]	Energy [eV]	$\sigma \times 10^{-22}$ [m^{-3}]
40.0	104.1	160.0	182.3	600.0	99.9
45.0	120.6	165.0	180.8	650.0	94.5
50.0	134.4	170.0	179.3	700.0	90.0
55.0	148.0	175.0	178.0	750.0	85.8
60.0	153.8	180.0	176.7	800.0	81.9
65.0	161.8	185.0	175.3	850.0	78.3
70.0	169.2	190.0	174.0	900.0	75.5
75.0	174.6	195.0	172.1	950.0	72.8
80.0	179.5	200.0	170.3	1000.0	70.5
85.0	184.1	210.0	167.4		

Reaction 8					
Energy [eV]	$\sigma \times 10^{-20}$ [m^{-3}]	Energy [eV]	$\sigma \times 10^{-20}$ [m^{-3}]	Energy [eV]	$\sigma \times 10^{-20}$ [m^{-3}]
0.0000	0.0000	9.0000	0.2300	17.000	0.0650
6.0000	0.0000	10.000	0.2100	20.000	0.0475
7.0000	0.1500	12.000	0.1650	45.000	0.0190
7.8000	0.2300	15.000	0.1050	10000	0.0000

Reaction 9					
Energy [eV]	$\sigma \times 10^{-22}$ [m^{-3}]	Energy [eV]	$\sigma \times 10^{-22}$ [m^{-3}]	Energy [eV]	$\sigma \times 10^{-22}$ [m^{-3}]
18.0	0.19	105.0	99.1	230.0	94.2
19.0	0.27	110.0	100.7	240.0	92.5
20.0	0.48	115.0	102.0	250.0	90.7
22.5	1.80	120.0	102.8	260.0	89.0
25.0	4.20	125.0	103.4	270.0	87.3
27.5	7.80	130.0	103.7	280.0	85.6
30.0	11.5	135.0	104.0	290.0	84.0
32.5	16.2	140.0	104.3	300.0	82.0
35.0	22.8	145.0	104.4	350.0	74.2
40.0	32.2	150.0	104.2	400.0	67.2
45.0	40.8	155.0	103.9	450.0	60.9
50.0	48.0	160.0	103.6	500.0	56.2
55.0	55.8	165.0	103.2	550.0	52.1
60.0	63.1	170.0	102.8	600.0	48.7
65.0	70.7	175.0	102.1	650.0	45.6
70.0	76.2	180.0	101.8	700.0	43.0
75.0	81.8	185.0	101.0	750.0	40.7
80.0	86.6	190.0	100.4	800.0	38.5
85.0	89.0	195.0	99.7	850.0	36.5
90.0	91.9	200.0	99.0	900.0	34.9
95.0	94.7	210.0	97.6	950.0	33.6
100.0	97.2	220.0	96.0	1000.0	33.0

Reaction 10					
Energy [eV]	$\sigma \times 10^{-22}$ [m^{-3}]	Energy [eV]	$\sigma \times 10^{-22}$ [m^{-3}]	Energy [eV]	$\sigma \times 10^{-22}$ [m^{-3}]
4.2	0	6.1	1.23	8.1	0.387
4.3	0.0088	6.2	1.31	8.2	0.334
4.4	0.0264	6.3	1.36	8.3	0.282
4.5	0.0440	6.5	1.41	8.4	0.238
4.6	0.0704	6.6	1.4	8.5	0.202
4.7	0.0968	6.7	1.37	8.6	0.167
4.8	0.132	6.8	1.34	8.7	0.141
4.9	0.176	6.9	1.28	8.8	0.123
5.0	0.22	7.0	1.22	8.9	0.106
5.1	0.29	7.1	1.14	9.0	0.088
5.2	0.361	7.2	1.06	9.1	0.0704
5.3	0.449	7.3	0.985	9.2	0.0704
5.4	0.537	7.4	0.897	9.3	0.0616
5.5	0.633	7.5	0.818	9.4	0.0528
5.6	0.748	7.6	0.739	9.5	0.0440
5.7	0.853	7.7	0.642	9.6	0.0440
5.8	0.959	7.8	0.572	9.8	0.0352
5.9	1.05	7.9	0.501	9.9	0.0352
6.0	1.14	8.0	0.449		

Reaction 11					
Energy [eV]	$\sigma \times 10^{-22}$ [m^{-3}]	Energy [eV]	$\sigma \times 10^{-22}$ [m^{-3}]	Energy [eV]	$\sigma \times 10^{-22}$ [m^{-3}]
15.0	0.0000	25.6	0.4056	40.0	0.5044
15.9	0.0000	26.8	0.4160	41.7	0.4940
16.8	0.0000	28.0	0.4472	43.9	0.4836
17.9	0.0156	28.9	0.4628	45.6	0.4784
18.9	0.0364	30.0	0.4888	47.9	0.4680
20.0	0.0676	30.8	0.5096	50.0	0.4628
21.8	0.1976	32.1	0.5200	52.0	0.4602
22.9	0.2600	33.7	0.5304	54.2	0.4576
23.9	0.3380	36.2	0.5200		
24.7	0.3692	38.0	0.5096		

Reaction 12					
Energy [eV]	$\sigma \times 10^{-20}$ [m^{-3}]	Energy [eV]	$\sigma \times 10^{-20}$ [m^{-3}]	Energy [eV]	$\sigma \times 10^{-20}$ [m^{-3}]
0.0000	0.0000	0.5900	0.0000	1.2300	0.0000
0.0067	0.0000	0.6800	0.0000	1.2300	0.0600
0.0700	0.0000	0.6900	0.0804	1.2600	0.0000
0.0800	0.0054	0.7100	0.0000	1.3400	0.0000
0.1000	0.0000	0.7900	0.0000	1.3500	0.0360
0.2000	0.0000	0.8000	0.0936	1.3700	0.0000
0.2100	0.0216	0.8100	0.0000	1.4400	0.0000
0.2200	0.0000	0.9000	0.0000	1.4500	0.0240
0.3200	0.0000	0.9100	0.0840	1.4700	0.0000
0.3300	0.0384	0.9300	0.0000	1.5400	0.0000
0.3500	0.0000	1.0200	0.0000	1.5500	0.0120
0.4400	0.0000	1.0300	0.0720	1.5700	0.0000
0.4500	0.0540	1.0500	0.0000	1.6400	0.0000
0.4700	0.0000	1.1300	0.0000	1.6500	0.0048
0.5600	0.0000	1.1400	0.0468	1.6700	0.0000
0.5700	0.0672	1.1600	0.0000	10000	0.0000

Reaction 13					
Energy [eV]	$\sigma \times 10^{-20}$ [m^{-3}]	Energy [eV]	$\sigma \times 10^{-20}$ [m^{-3}]	Energy [eV]	$\sigma \times 10^{-20}$ [m^{-3}]
0.0000	0.0000	0.7100	0.0000	1.3400	0.0000
0.1900	0.0000	0.7900	0.0000	1.3500	0.0165
0.2000	0.0010	0.8000	1.0000	1.3700	0.0000
0.2100	0.0010	0.8200	0.0000	1.4400	0.0000
0.2300	0.0000	0.9000	0.0000	1.4500	0.0055
0.3200	0.0000	0.9100	0.6000	1.4700	0.0000
0.3300	0.4150	0.9300	0.0000	1.5400	0.0000
0.3500	0.0000	1.0200	0.0000	1.5500	0.0019
0.4400	0.0000	1.0300	0.2850	1.5700	0.0000
0.4500	1.3500	1.0500	0.0000	1.6300	0.0000
0.4700	0.0000	1.1300	0.0000	1.6500	0.0006
0.5600	0.0000	1.1400	0.1125	1.6700	0.0000
0.5700	1.8500	1.1600	0.0000	3.5000	0.0000
0.5900	0.0000	1.2300	0.0000	4.0000	0.0000
0.6800	0.0000	1.2400	0.0475	5.0000	0.0000
0.6900	1.6500	1.2600	0.0000	10000	0.0000

Reaction 14					
Energy [eV]	$\sigma \times 10^{-20}$ [m^{-3}]	Energy [eV]	$\sigma \times 10^{-20}$ [m^{-3}]	Energy [eV]	$\sigma \times 10^{-20}$ [m^{-3}]
0.0000	0.0000	0.9000	0.0000	1.3700	0.0000
0.3800	0.0000	0.9100	0.4650	1.4400	0.0000
0.4400	0.0000	0.9300	0.0000	1.4500	0.0185
0.4500	0.0000	1.0200	0.0000	1.4700	0.0000
0.4700	0.0000	1.0300	0.3150	1.5400	0.0000
0.5600	0.0000	1.0500	0.0000	1.5500	0.0085
0.5700	0.1400	1.1300	0.0000	1.5700	0.0000
0.5900	0.0000	1.1400	0.2000	1.6300	0.0000
0.6800	0.0000	1.1600	0.0000	1.6500	0.0034
0.6900	0.4150	1.2300	0.0000	1.6700	0.0000
0.7100	0.0000	1.2400	0.0950	3.5000	0.0000
0.7900	0.0000	1.2600	0.0000	4.0000	0.0000
0.8000	0.5350	1.3400	0.0000	5.0000	0.0000
0.8200	0.0000	1.3500	0.0400	10000	0.0000

Reaction 15					
Energy [eV]	$\sigma \times 10^{-20}$ [m^{-3}]	Energy [eV]	$\sigma \times 10^{-20}$ [m^{-3}]	Energy [eV]	$\sigma \times 10^{-20}$ [m^{-3}]
0.0000	0.0000	1.1600	0.0000	3.5000	0.0000
0.5700	0.0000	1.2300	0.0000	4.0000	0.0000
0.6800	0.0000	1.2400	0.0950	5.0000	0.0000
0.6900	0.0037	1.2600	0.0000	6.0000	0.0125
0.7100	0.0000	1.3400	0.0000	7.0000	0.0363
0.7900	0.0000	1.3500	0.0550	8.0000	0.0588
0.8000	0.0215	1.3700	0.0000	9.0000	0.0750
0.8200	0.0000	1.4400	0.0000	10.000	0.0675
0.9000	0.0000	1.4500	0.0300	11.000	0.0563
0.9100	0.0900	1.4700	0.0000	12.000	0.0475
0.9300	0.0000	1.5400	0.0000	13.000	0.0300
1.0200	0.0000	1.5500	0.0165	14.000	0.0175
1.0300	0.1200	1.5700	0.0000	15.000	0.0088
1.0500	0.0000	1.6300	0.0000	20.000	0.0000
1.1300	0.0000	1.6500	0.0080	45.000	0.0000
1.1400	0.1150	1.6700	0.0000	10000	0.0000

Reaction 16					
Energy [eV]	$\sigma \times 10^{-20}$ [m^{-3}]	Energy [eV]	$\sigma \times 10^{-20}$ [m^{-3}]	Energy [eV]	$\sigma \times 10^{-20}$ [m^{-3}]
0.0000	0.0000	1.2300	0.0000	1.6700	0.0000
0.7500	0.0000	1.2400	0.0315	6.0000	0.0000
0.7900	0.0000	1.2600	0.0000	7.0000	0.0275
0.8000	0.0015	1.3400	0.0000	8.0000	0.0350
0.8200	0.0000	1.3500	0.0335	9.0000	0.0413
0.9000	0.0000	1.3700	0.0000	10.000	0.0462
0.9100	0.0055	1.4400	0.0000	11.000	0.0313
0.9300	0.0000	1.4500	0.0285	12.000	0.0250
1.0200	0.0000	1.4700	0.0000	13.000	0.0175
1.0300	0.0003	1.5400	0.0000	14.000	0.0088
1.0500	0.0000	1.5500	0.0215	15.000	0.0000
1.1300	0.0000	1.5700	0.0000	10000	0.0000
1.1400	0.0165	1.6300	0.0000		
1.1600	0.0000	1.6500	0.0165		

Reaction 17		**Reaction 18**		**Reaction 19**	
Energy [eV]	$\sigma \times 10^{-20}$ [m^{-3}]	Energy [eV]	$\sigma \times 10^{-20}$ [m^{-3}]	Energy [eV]	$\sigma \times 10^{-20}$ [m^{-3}]
0.000	0.0000	0.000	0.0000	10	0.1305
0.977	0.0000	1.627	0.0000	15	0.075
1.500	0.0058	2.000	0.0026	20	0.039
2.000	0.0153	3.000	0.0097	30	0.013
3.000	0.0380	3.500	0.0133		
3.500	0.0490	4.000	0.0149		
4.000	0.0570	5.000	0.0182		
5.000	0.0740	5.690	0.0194		
5.620	0.0825	6.540	0.0194		
5.910	0.0862	7.340	0.0191		
6.190	0.0888	8.410	0.0183		
6.530	0.0908	9.260	0.0174		
6.990	0.0914	10.00	0.0160		
7.610	0.0891	13.00	0.0130		
7.890	0.0863	14.90	0.0130		
8.960	0.0768	17.00	0.0130		
10.04	0.0679	19.40	0.0125		
13.00	0.0527	20.70	0.0125		
15.10	0.0455	22.50	0.0110		
17.50	0.0387	24.00	0.0100		
20.50	0.0324	28.00	0.0080		
24.90	0.0256	35.10	0.0063		
30.90	0.0196	41.90	0.0018		
41.00	0.0137	45.10	0.0005		
45.00	0.0120	1000	0.0000		
10000	0.0000	10000	0.0000		

Reaction 20		**Reaction 21**		**Reaction 22**	
Energy [eV]	$\sigma \times 10^{-20}$ [m^{-3}]	Energy [eV]	$\sigma \times 10^{-20}$ [m^{-3}]	Energy [eV]	$\sigma \times 10^{-20}$ [m^{-3}]
0.0000	0.0000	0.0000	0.0000	0.0000	0.0000
8.4000	0.0000	10.000	0.0000	14.700	0.0000
9.4000	1.0000	20.000	0.0130	20.000	0.0085
30.000	0.9000	30.000	0.0260	25.000	0.0160
50.000	0.7000	40.000	0.0400	30.000	0.0225
100.00	0.5400	50.000	0.0500	40.000	0.0280
150.00	0.3200	60.000	0.0600	60.000	0.0370
200.00	0.2700	70.000	0.0650	70.000	0.0380
300.00	0.1700	80.000	0.0700	80.000	0.0390
500.00	0.1090	100.00	0.0700	100.00	0.0380
700.00	0.0800	120.00	0.0500	500.00	0.0000
1000.0	0.0580	150.00	0.0400	10000	0.0000
1500.0	0.0420	170.00	0.0350		
2000.0	0.0330	200.00	0.0300		
3000.0	0.0240	300.00	0.0200		
5000.0	0.0160	500.00	0.0120		
7000.0	0.0120	700.00	0.0080		
10000	0.0090	1000.0	0.0050		
		1500.0	0.0000		
		2000.0	0.0000		
		3000.0	0.0000		
		5000.0	0.0000		
		7000.0	0.0000		
		10000	0.0000		

Reaction 27					
Energy [eV]	$\sigma \times 10^{-22}$ [m^{-3}]	Energy [eV]	$\sigma \times 10^{-22}$ [m^{-3}]	Energy [eV]	$\sigma \times 10^{-22}$ [m^{-3}]
2.930	0.0185	5.110	5.7460	7.332	1.6102
3.073	0.0388	5.295	6.1940	7.517	1.2028
3.258	0.2328	5.480	5.9400	7.702	1.0088
3.443	0.4268	5.665	5.6490	7.815	0.8342
3.628	0.6208	5.850	5.1640	8.166	0.6402
3.813	1.0088	6.037	4.7760	8.351	0.4462
4.000	1.5908	6.222	4.1940	8.536	0.2910
4.185	2.3880	6.407	3.7848	8.721	0.2134
4.370	2.9700	6.592	3.2804	8.906	0.1940
4.555	4.0000	6.777	2.7760	9.091	0.0776
4.740	4.7760	6.925	2.3880	9.276	0.0582
4.925	5.5520	7.110	1.8042	9.461	0.0582

Reaction 28					
Energy [eV]	$\sigma \times 10^{-22}$ [m^{-3}]	Energy [eV]	$\sigma \times 10^{-22}$ [m^{-3}]	Energy [eV]	$\sigma \times 10^{-22}$ [m^{-3}]
5.01	0.0194	6.98	1.0476	8.70	0.2716
5.29	0.0149	7.16	1.2416	8.89	0.1552
5.57	0.0194	7.35	1.3774	9.07	0.1164
5.85	0.0582	7.53	1.3774	9.26	0.0970
6.05	0.0679	7.72	1.2416	9.50	0.0776
6.24	0.2134	7.90	1.2028	10.04	0.0776
6.42	0.2910	8.14	1.0476	10.22	0.0776
6.61	0.4656	8.33	0.8342	10.41	0.0776
6.79	0.7566	8.52	0.5626		

Reaction 39					
Energy [eV]	$\sigma \times 10^{-21}$ [m^{-3}]	Energy [eV]	$\sigma \times 10^{-21}$ [m^{-3}]	Energy [eV]	$\sigma \times 10^{-21}$ [m^{-3}]
0.1	10.0000	3.5	0.1300	6.8	0.0350
0.2	6.5000	3.6	0.1500	6.9	0.0300
0.3	5.0000	3.7	0.1300	7.0	0.0290
0.4	3.2000	3.8	0.1200	7.1	0.0280
0.5	2.0000	3.9	0.1000	7.2	0.0290
0.6	1.6000	4.0	0.1200	7.3	0.0280
0.7	1.0000	4.1	0.1100	7.4	0.0280
0.8	0.8000	4.2	0.1000	7.5	0.0250
0.9	0.6500	4.3	0.1100	7.6	0.0230
1.0	0.5500	4.4	0.0900	7.7	0.0220

Reaction 39 (*continued*)					
Energy [eV]	$\sigma \times 10^{-21}$ [m^{-3}]	Energy [eV]	$\sigma \times 10^{-21}$ [m^{-3}]	Energy [eV]	$\sigma \times 10^{-21}$ [m^{-3}]
1.1	0.4800	4.5	0.0900	7.8	0.0210
1.2	0.3500	4.6	0.0800	7.9	0.0200
1.3	0.3200	4.7	0.0900	8.0	0.0200
1.4	0.2900	4.8	0.0900	8.1	0.0190
1.5	0.2700	4.9	0.0750	8.2	0.0180
1.6	0.2500	5.0	0.0700	8.3	0.0170
1.7	0.2400	5.1	0.0650	8.4	0.0170
1.8	0.2200	5.2	0.0700	8.5	0.0170
1.9	0.2100	5.3	0.0650	8.6	0.0150
2.0	0.1900	5.4	0.0600	8.7	0.0130
2.1	0.2000	5.5	0.0600	8.8	0.0130
2.2	0.1900	5.6	0.0650	8.9	0.0120
2.3	0.1800	5.7	0.0550	9.0	0.0120
2.4	0.1900	5.8	0.0500	9.1	0.0110
2.5	0.1700	5.9	0.0500	9.2	0.0110
2.6	0.1600	6.0	0.0450	9.3	0.0100
2.7	0.1700	6.1	0.0500	9.4	0.0090
2.8	0.1600	6.2	0.0450	9.5	0.0090
2.9	0.1600	6.3	0.0450	9.6	0.0085
3.0	0.1700	6.4	0.0400	9.7	0.0085
3.1	0.1600	6.5	0.0350	9.8	0.0085
3.2	0.1400	6.6	0.0400	9.9	0.0080
3.3	0.1600	6.7	0.0350	10.0	0.0080
3.4	0.1400				

Reaction 42		**Reaction 43**		**Reaction 44**	
Energy [eV]	$\sigma \times 10^{-21}$ [m^{-3}]	Energy [eV]	$\sigma \times 10^{-21}$ [m^{-3}]	Energy [eV]	$\sigma \times 10^{-21}$ [m^{-3}]
4.5	3.74	22.5	0.01	0.000336	33460
5.5	4.62	24.5	0.04	0.000745	14484
6.5	3.31	28.5	0.16	0.00164	5185
7.5	2.07	33.5	0.37	0.00391	1988
8.5	3.55	38.5	0.51	0.00517	1554
10.5	5.70	43.5	0.87	0.00714	1170
12.5	8.14	48.5	1.35	0.0113	731.6
14.5	11.07	58.5	2.27	0.0136	602.4
16.5	12.11	68.5	2.98	0.0164	476.6
18.5	13.44	78.5	3.68	0.0225	315.2
22.5	15.15	88.5	4.49	0.0294	194.0
24.5	15.91	98.5	4.98	0.0373	145.52
28.5	17.67	118.5	5.30	0.0461	113.39
33.5	18.85	148.5	5.25	0.0663	83.64
38.5	20.54	198.5	4.82	0.103	77.01
43.5	20.98	248.5	4.33	0.147	23.52
48.5	21.11	298.5	3.95	0.199	20.79
58.5	21.42	348.5	3.36	0.218	18.76
68.5	21.80	498.5	3.03	0.231	13.79
78.5	21.95	598.5	2.54	0.258	17.08
88.5	22.00	798.5	2.11	0.279	11.97
98.5	21.90	998.5	1.79	0.301	20.88
118.5	21.43	1498.5	1.19	0.503	11.34
148.5	20.32	1998.5	1.00	0.818	4.032
198.5	18.21	2498.5	0.87	1	2.232
248.5	16.54			1.2	3.096
298.5	15.17			1.41	3.024
398.5	13.13			1.5	3.006
498.5	11.70			1.59	1.044
598.5	10.60			1.68	1.2546
798.5	8.98			1.78	1.4004
998.5	7.84			1.87	2.124
1498.5	5.87			1.97	1.4058
1998.5	4.60			2.18	1.629
2498.5	3.73			2.5	1.4274

Reaction 45		**Reaction 46**		**Reaction 47**	
Energy [eV]	$\sigma \times 10^{-20}$ [m^{-3}]	Energy [eV]	$\sigma \times 10^{-20}$ [m^{-3}]	Energy [eV]	$\sigma \times 10^{-20}$ [m^{-3}]
0.000336	7216	1.00	4.45	14	0.00383
0.000745	3124	1.17	4.90	16	0.0247
0.00164	1341	1.37	5.56	18	0.0651
0.00391	681.6	1.61	5.74	20	0.133
0.00517	532.8	1.89	6.51	25	0.334
0.00714	452.62	2.00	6.62	30	0.509
0.0113	283.02	3.00	6.95	35	0.649
0.0136	207.57	4.00	7.64	40	0.767
0.0164	164.22	5.00	7.76	45	0.868
0.0225	92.59	6.00	7.76	50	0.951
0.0294	63.07	7.00	7.64	60	1.071
0.0373	50.504	8.00	7.52	70	1.149
0.0461	39.353	9.00	7.52	80	1.198
0.0663	29.028	10.00	7.29	90	1.227
0.103	26.727	20.00	6.52	100	1.243
0.147	20.496	30.00	5.39	120	1.247
0.199	18.117	40.00	4.52	150	1.220
0.218	16.348	50.00	4.11	180	1.175
0.231	12.017	60.00	3.62	200	1.142
0.258	14.884	70.00	3.29	250	1.058
0.279	10.431	80.00	3.04	300	0.981
0.301	4.524	90.00	2.99	350	0.912
0.503	0.2457	100.00	2.64	400	0.852
0.818	0.8736	200.00	1.61	450	0.799
1	0.4836	300.00	1.25	500	0.752
1.2	0.6708	400.00	1.00	600	0.673
1.41	0.6552	500.00	0.90	700	0.610
1.5	0.6513	600.00	0.73	800	0.558
1.59	0.2262	700.00	0.67	900	0.514
1.68	0.27183	800.00	0.57	1000	0.478
1.78	0.30342	900.00	0.54	2000	0.284
1.87	0.4602	1000.00	0.49	3000	0.205
1.97	0.30459	2000.00	0.30	4000	0.162
2.18	0.35295	3000.00	0.22	5000	0.135
2.5	0.30927	4000.00	0.16		
		5000.00	0.12		
		6000.00	0.11		

Reaction 48		**Reaction 49**		**Reaction 50**	
Energy [eV]	$\sigma \times 10^{-22}$ [m^{-3}]	Energy [eV]	$\sigma \times 10^{-22}$ [m^{-3}]	Energy [eV]	$\sigma \times 10^{-22}$ [m^{-3}]
2.1	0.82	4.4	0.54	16.0	0.17
2.4	5.41	4.8	1.30	18.0	1.27
2.7	10.7	5.0	1.60	20.0	2.09
3	15.4	6.0	2.57	25.0	4.11
4	24.9	7.0	3.02	30.0	6.82
4.4	26.7	8.0	3.22	40.0	12.7
4.8	27.7	9.0	3.28	45.0	13.6
5	28.0	10.0	3.27	50.0	14.1
6	28.3	12.0	3.15	55.0	13.7
7	27.4	14.0	2.97	70.0	11.5
8	26.0	16.0	2.79	100.0	7.45
9	24.4	18.0	2.61	150.0	4.49
10	22.8	20.0	2.44	200.0	3.14
12	19.8	25.0	2.09		
14	17.1	30.0	1.80		
16	14.8	40.0	1.37		
18	12.9	45.0	1.21		
20	11.2	50.0	1.07		
25	8.07	55.0	0.95		
30	5.9	70.0	0.69		
40	3.34	100.0	0.38		
45	2.58	150.0	0.16		
50	2.02	200.0	0.08		
55	1.61				
70	0.87				
100	0.33				
150	0.11				
200	0.05				

Reaction 51		**Reaction 52**		**Reaction 53**	
Energy [eV]	$\sigma \times 10^{-22}$ [m^{-3}]	Energy [eV]	$\sigma \times 10^{-22}$ [m^{-3}]	Energy [eV]	$\sigma \times 10^{-22}$ [m^{-3}]
9.9	0.350	9.9	3.42	12	3.96
10.1	0.540	10.1	4.41	14	17.03
10.5	1.060	10.5	5.48	16	25.99
11.0	1.370	11.0	6.28	18	30.83
12.0	1.780	12.0	7.71	20	34.29
14.0	2.330	14.0	9.87	25	33.94
16.0	2.850	16.0	10.50	30	33.28
18.0	3.190	18.0	11.00	40	35.28
20.0	3.080	20.0	11.10	50	36.19
22.0	2.780	22.0	10.80	60	56.0
25.0	2.290	25.0	10.40	70	28.87
28.0	1.770	28.0	9.30	100	21
30.0	1.510	30.0	8.69	150	18.859
35.0	0.910	35.0	8.37	200	13.555
40.0	0.610	40.0	8.10	300	10.215
45.0	0.430	45.0	7.95	400	8.254
50.0	0.310	50.0	7.81	500	7.051
55.0	0.230	55.0	7.62	600	6.156
60.0	0.180	60.0	7.45	700	5.442
70.0	0.110	70.0	7.16	800	4.946
100.0	0.040	100.0	6.30	900	4.493
150.0	0.011	150.0	5.27	1000	4.099
200.0	0.005	200.0	4.37		

Reaction 54					
Energy [eV]	$\sigma \times 10^{-20}$ [m^{-3}]	Energy [eV]	$\sigma \times 10^{-20}$ [m^{-3}]	Energy [eV]	$\sigma \times 10^{-20}$ [m^{-3}]
1.491	0.000075892	11.5	4.7768	21.5	5.2774
2.0	0.41484	12.0	4.8669	22.0	5.2687
2.5	0.80103	12.5	4.9469	22.5	5.2608
3.0	1.1667	13.0	5.0173	23.0	5.2542
3.5	1.5125	13.5	5.0787	23.5	5.2495
4.0	1.8388	14.0	5.1316	24.0	5.2473
4.5	2.1463	14.5	5.1765	24.5	5.2480
5.0	2.4355	15.0	5.2141	25.0	5.2522
5.5	2.7069	15.5	5.2448	25.5	5.2604
6.0	2.9611	16.0	5.2692	26.0	5.2733
6.5	3.1986	16.5	5.2878	26.5	5.2914
7.0	3.4200	17.0	5.3013	27.0	5.3151
7.5	3.6258	17.5	5.3100	27.5	5.3451
8.0	3.8166	18.0	5.3146	28.0	5.3819
8.5	3.9929	18.5	5.3157	28.5	5.4260
9.0	4.1552	19.0	5.3137	29.0	5.4780
9.5	4.3042	19.5	5.3092	29.5	5.5384
10.0	4.4402	20.0	5.3028	30.0	5.6078
10.5	4.5640	20.5	5.2950		
11.0	4.6760	21.0	5.2864		

FOLHA DE REGISTRO DO DOCUMENTO

1. CLASSIFICAÇÃO/TIPO	2. DATA	3. DOCUMENTO Nº	4. Nº DE PÁGINAS
TD	13 de dezembro de 2016	DCTA/ITA/TD-040/2016	93

5. TÍTULO E SUBTÍTULO:
A volume averaged global model study of oxygen discharges – formation and annihilation of the singlet molecular metastables and effects of the electron energy distribution function

6. AUTOR(ES):
David Arruda Toneli

7. INSTITUIÇÃO(ÕES)/ÓRGÃO(S) INTERNO(S)/DIVISÃO(ÕES):
Instituto Tecnológico de Aeronáutica – ITA

8. PALAVRAS-CHAVE SUGERIDAS PELO AUTOR:
Física; plasma; oxigênio; metaestáveis; modelagem.

9. PALAVRAS-CHAVE RESULTANTES DE INDEXAÇÃO:
Plasma de oxigênio; Descargas elétricas; Reatores; Energia de elétrons; Densidade; Física de plasmas; Física.

10. APRESENTAÇÃO: (**X**) **Nacional** ( ) **Internacional**
ITA, São José dos Campos. Curso de Doutorado. Programa de Pós-Graduação em Física. Área de Física de Plasmas. Orientador(es): Profª. Drª. Marisa Roberto; co-orientador(es): Prof. Dr. Rodrigo Sávio Pessoa. Defesa em 02/12/2016. Publicada em 2016.

11. RESUMO:
This work describes a computational model called volume averaged global model for an oxygen plasma produced in an inductive reactor coupled to an AC power source which operates at a frequency of 13.56 MHz. This model considers an extensive reaction set that includes the species: $O_2(X^3\Sigma_g^-)$, $O_2(a^1\Delta_g)$, $O_2(b^1\Sigma_g^+)$, $O_2(A^3\Sigma_u^+$, $A'^3\Delta_u$, $c^1\Sigma_u^-)$, O_2^+, O_2^-, $O(^3P)$, $O(^1D)$, O^+, O^-, O_3, O_3^+, O_3^-, and electrons. Rate coefficients for some reactions are evaluated and new values are proposed. It was calculated the densities of various species as a function of discharge pressure in the pressure range 1 – 100 mTorr. In this work, the influence of the electron energy distribution function (EEDF) and the wall material were also evaluated. Differences in the results for Maxwellian and non-Maxwellian distributions show the importance of using a proper EEDF in discharge modelling. It was also explored the differences due to different reactor wall materials comparing the results for an anodized aluminium reactor with a stainless steel reactor. Due to the low recombination coefficient for oxygen atoms on the anodized aluminium walls, the yield of atomic oxygen in anodized aluminium reactors increases significantly as compared to stainless steel reactors. However, the difference of the yield of atomic oxygen in these reactors decreases as pressure increases. Thus, anodized aluminium reactors can be desired for applications where a high concentration of atomic oxygen is required. Formation and annihilation of the singlet molecular metastables were evaluated. It was found that the $O_2(a^1\Delta_g)$ density can be lower than the $O_2(b^1\Sigma_g^+)$ density contradicting previous results. The relative reaction rates for formation and annihilation of $O_2(a^1\Delta_g)$ and $O_2(b^1\Sigma_g^+)$ are evaluated and the most important reactions are indicated. Recently, experimental results have shown that the velocity of each ion at the sheath edge can approximate to a common value. One of these values would be the solution of the generalized Bohm criterion assuming that all ions reach the sheath edge at the same velocity. Thus, in this work, it was also studied this common velocity of the ions through an expression obtained from the dispersion relation for a plasma with many species of positive and negative ions. As the electronegativity at the sheath increases, the common velocity of the ions decreases as the Bohm velocity.

12. GRAU DE SIGILO:
(**X**) **OSTENSIVO** ( ) **RESERVADO** ( ) **SECRETO**